Inorganic and Organic Photovoltaic Materials for Powering Electrochromic Systems

by

Ebraheem Ali Azhar

A Dissertation Presented in Partial Fulfillment
of the Requirements for the Degree
Doctor of Philosophy

Approved April 2018 by the
Graduate Supervisory Committee:

Hongbin Yu, Co-Chair
Sandwip Dey, Co-Chair
Michael Goryll
Terry Alford

ARIZONA STATE UNIVERSITY

May 2018

ABSTRACT

Autonomous smart windows may be integrated with a stack of active components, such as electrochromic devices, to modulate the opacity/transparency by an applied voltage. Here, we describe the processing and performance of two classes of visibly-transparent photovoltaic materials, namely inorganic (ZnO thin film) and fully organic (PCDTBT:$PC_{70}BM$), for integration with electrochromic stacks.

Sputtered ZnO (2% Mn) films on ITO, with transparency in the visible range, were used to fabricate metal-semiconductor (MS), metal-insulator-semiconductor (MIS), and p-i-n heterojunction devices, and their photovoltaic conversion under ultraviolet (UV) illumination was evaluated with and without oxygen plasma-treated surface electrodes (Au, Ag, Al, and Ti/Ag). The MS Schottky parameters were fitted against the generalized Bardeen model to obtain the density of interface states ($D_{it} \approx 8.0\times10^{11}$ $eV^{-1}cm^{-2}$) and neutral level ($E_o \approx$ -5.2 eV). These devices exhibited photoconductive behavior at $\lambda = 365$ nm, and low-noise Ag-ZnO detectors exhibited responsivity (R) and photoconductive gain (G) of 1.93×10^{-4} A/W and 6.57×10^{-4}, respectively. Confirmed via matched-pair analysis, post-metallization, oxygen plasma treatment of Ag and Ti/Ag electrodes resulted in increased Schottky barrier heights, which maximized with a 2 nm SiO_2 electron blocking layer (EBL), coupled with the suppression of recombination at the metal/semiconductor interface and blocking of majority carriers. For interdigitated devices under monochromatic UV-C illumination, the open-circuit voltage (V_{oc}) was 1.2 V and short circuit current density (J_{sc}), due to minority carrier tunneling, was 0.68 mA/cm^2.

A fully organic bulk heterojunction photovoltaic device, composed of poly[N-9'-heptadecanyl-2,7-carbazole-alt-5,5-(4',7'-di-2-thienyli2',1',3'-benzothiadiazole)]:phenyl-C71-butyric-acidmethyl (PCDTBT:$PC_{70}BM$), with corresponding electron and hole transport layers, i.e., LiF with Al contact and conducting/non-conducting (nc) PE-

DOT:PSS (with ITO/PET or Ag nanowire/PDMS contacts; the illuminating side), respectively, was developed. The PCDTBT/$PC_{70}BM$/PEDOT:$PSS_{(nc)}$/ITO/PET stack exhibited the highest performance: power conversion efficiency (PCE) $\approx 3\%, V_{oc}$ = 0.9V, and $J_{sc} \approx$ 10-15 mA/cm^2. These stacks exhibited high visible range transparency, and provided the requisite power for a switchable electrochromic stack having an inkjet-printed, optically-active layer of tungsten trioxide (WO_3), peroxo-tungstic acid dihydrate, and titania (TiO_2) nano-particle-based blend. The electrochromic stacks (i.e., PET/ITO/$LiClO_4$/WO_3 on ITO/PET and Ag nanowire/PDMS substrates) exhibited optical switching under external bias from the PV stack (or an electrical outlet), with 7 s coloration time, 8 s bleaching time, and 0.36-0.75 optical modulation at λ=525 nm. The devices were paired using an Internet of Things controller that enabled wireless switching.

DEDICATION

This work is dedicated to my mother, Chia-Lan, who's love and support have made me capable of becoming a better person through pursuing education.

ACKNOWLEDGMENTS

First and foremost, I would like to express my sincere gratitude to my research co-advisers Dr. Hongbin Yu and Dr. Sandwip Dey. Their patience, yet willingness to challenge me to think about my work at a deeper level have been of great inspiration. Opening up the smart-window project and allowing me creative license to pursue its completion has been instrumental in allowing me to develop an investigative research philosophy, and a personal workflow/library for designing/running experiments, analyzing data, and reporting scientific results. Their input on all aspects of my work (particularly their expertise in device physics and characterization), has helped me better understand, model, and describe the most salient aspects of this dissertation. I cannot thank these two professors enough for supporting me throughout my graduate career. I would also like to thank Professor Michael Goryll, who has been a great mentor to me. Our late-evening/weekend discussions on everything from infrared spectroscopy, microscopy, electrochemistry, all the way down the rabbit hole to state minimization using implicant tables, various legacy hardware hacks, and German cars (you know, typical nerd stuff), have always been enriching and illuminating for me. Between all of his academic commitments (teaching, committees, senior design, research), I have no idea how he still made time to help me with my own research, and for that, I'm eternally thankful. I am also extremely grateful to Professor Terry Alford for enabling my study of organic solar cells, and all of his invaluable feedback on my research. His support has allowed me to better understand photovoltaic characterization.

My thanks to CSSER staff, especially Jon Martin, Todd Eller, Carrie Sinclair, Timothy Eschrich, Wayne Paulson, Arthur Handuagan, and Stefan Myhajlenko for all their time and effort in equipment training. They have always been readily available upon needing assistance with any processing or characterization issues. Thanks to

the LeRoy Eyring Center for Solid State Science (CSSS) staff, of whom, I would like to thank David Wright and Timothy Karcher for help with all experiments both inside and outside the facilities. To David, thank you for guiding me for nearly a decade on the single zone growth and anneal tube furnaces, and most recently thanks to you and Dr. Emmanuel Soignard for helping me interpret high resolution X-ray diffractograms.

I would also like to acknowledge a few senior colleagues from my research group who have since graduated and carry incredible lives: Dr. Tawab Dastigir, for kicking off my practical interests in nano-materials and devices, Dr. Wei Xu, for our stimulating discussions and thorough assistance in executing experiments, Tej Belagodu, for helping me start on, guiding me throughout the entire nanowire device fabrication process, Dr. Xiaodi Sun, for our work together on the smart window project, among others. I would like thank my peers Dr. Hanshuang Liang, Dr. Hao Wu, Seungho Ahn, Dr. Mahmoud Khdour, and Dr. Jhih-Hong Peng for their support and creating an environment conducive to quality research, and for constantly showing interest in my projects. To the junior members I have had a chance to learn from: Jignesh Vanjaria, thanks for being my personal punching bag these last three years, but more importantly, critically collaborating on ZnMgO nanowires, and to Todd Houghton, thank you for doing most of the heavy lifting in figuring out the MicroFab printer during a period I was too busy, and for being someone I can consult on nanoparticles. I consider the both of you colleagues for life. To the undergraduate researchers (many of whom have gone to pursue doctorates themselves) who have facilitated my work and helped me gather data for my work: William Scheidler (NNIN REU), David Bull (FURI), Gregory Spell (FURI), Lucas Thompson (FURI), Micah Tuttle, and Thomas Fou (FURI)—thank you so much for your time take out of your busy semesters and invaluable summers.

I would like to especially recognize the few colleagues who contributed directly to this project: George Chen for electrical characterization and data visualization, Weidong Ye for electrical characterization and manuscript revising, Chelsey McAlpin for electrochromic stack fabrication and manuscript revising, Benjamin Helfrecht (REU, NNIN) for device design, fabrication and characterization trials, and model visualization, and Wai Mun (Sally) Cheung for ZnO and Ag nanowire synthesis, electrical characterization, data visualization, data analysis, and manuscript revising. I would also like to extend my gratitude to Dr. Zhao Zhao for guiding me through the organic solar cell fabrication and characterization process, as well as providing insights on device failure.

I also take this opportunity to thank all my other research colleagues for providing useful and innovative research methods, materials, and for helping me out in general. They include Dr. Swee Hoe Lim, Dr. Cunjiang Yu, Dr. Teng Ma, Dr. Raghuraj Hathwar, Dr. Punarvasu Joshi, Dr. Bill Lepkowski, Dr. Reza Ghajar, Maryam Shakib, Dr. Pradymna Muralidharen, Hank Detlaff, Iniyan Elongo, Sai Baluguri, Sridutt Tummalapalli, Dr. Ganesh Subramanian, Dr. Nishant Chandra, Steve Mussi, Dr. Michael DiNezza, Dr. Derek Caselli, Dr. Shirong Zhou, Dr. Preston Webster, Dr. Maitreya Dutta, Dr. Owen Hildreth, Avinash Mamidanna, Chris Lefky, Dr. Rui Tang, Dr. Salman Manzoor, Dr. Xiaofeng Wang, Dr. Xu Wang, Dr. Shankar Ramakrishnan, Dr. Samet Arda, Arvind Shalindar, and many others not mentioned for helping me out at various times during the course of this work.

Several sources of funding have made this work possible, and I am grateful for their support. These include the Medtronic Employee Scholarship, IEEE Phoenix Chapter Fellowship, and Center for Nanotechnology in Society Fellowship, which in total supported me for three years. My work also received financial support by the National Science Foundation (Grant Number: 1143570) as well as NASA (Grant Number:

NNX-15CG10C) through a subcontract from Structured Materials Industries, Inc., Piscataway, New Jersey.

I would also like to thank some of the important people in my life who so patiently endured the insanity throughout my tenure in the program (in no particular order): Chelsea Wegner, for being incredible through the worst of it; James Maurice Cloud, for being available since the beginning; Dion Jerel Pouncil, for including me in all your creative enterprises; Stephanie Zankman, for showing me what madness lies before a med student; Michael Hamouda, for helping me gain perspective while simultaneously fighting your own legal battles; Patrick Krecker, for annually giving me a glimpse into the real world; Kevin King, for helping me understand academics, pop culture, politics, and everything in between; Kelsey Marks, for our shared love of delightfully silly, cringe-inducing memes (Turquoise Jeep), and of course your unwavering support as I unraveled; Devin Clark, for always bringing a sensible perspective to my professional endeavours; Jeffery Walloch, mutually obsessing about GM since the 90s; and Stacy Caligiuri, for your optimism and support during a major inflection point in my graduate career. Despite graduate school compromising my ability to connect with everyone, please know I wish you the absolute best in your personal and professional lives ahead.

To members of my family, who have had an even harder time seeing me: Uncle Chung-Sheng, thank you for inspiring me to pursue a doctoral program, developing a taste for American cars, supporting my interests in photography, and for turning me into a bit of an audiophile; to my father, Mahmood, and siblings Pakeeza, Rabih, and Aleeza, whom I am hoping to see more regularly. To my grandmother Kuei-Yueh Li, who I am looking forward to spending more time with.

Above all, this work would not have been possible without the support of my amazing mother Chia-Lan. It is impossible to completely express the gratitude I owe

her. I thank her for having faith in me and encouraging me to stick it out every time I felt like giving up. She has unconditionally supported, and dealt with the fallout of all my choices, and I could not have possibly asked for a kinder, gentler, more understanding mother. Mom, thank you for everything.

TABLE OF CONTENTS

CHAPTER Page

CHAPTER Page

LIST OF TABLES

Table Page

LIST OF FIGURES

Figure Page

Figure Page

Figure Page

Figure Page

Figure Page

Chapter 1

INTRODUCTION

1.1 Motivation

1.1.1 Energy Challenges

The United States Department of Energy (DOE) has served as the guide and motivator for standardizing public knowledge of both energy conservation and surveying new sources for energy. In fact, the DOE maintains a national residential efficiency measures database that accumulates portions of the households that most prone to radiant and insulating heat. As recently as 2018, the Energy Information Administration (EIA), a subset of the DOE, estimated that heating and cooling categories represented a majority of the non-pooled studied energy consumption (listed as 'other'). It is estimated that 20-50% of heat absorption occurs from sunlight radiation through windows (US Department of Energy, 2018), however, more specifically, it is projected that removing cooling loads from windows totals about 5 quadrillion BTUs and 3 quadrillion BTUs for residential and commercial (EIA, 2017), respectively, and this accounted for over 15% of total energy consumption in the U.S (EIA, 2017; Wong and Chan, 2013; DeForest *et al.*, 2015; Piccolo and Simone, 2015). Additionally, energy consumption normalized to building sizes indicated that cooling accounted for the highest majority at 25,000 BTUs per square foot (EIA, 2017). In 2001, it was estimated that 1.5 quadrillion BTUs per year amounted to costs of almost $15 billion (Deb *et al.*, 2001). A staggering 2 billion square meters of flat glass is produced worldwide each year (Deb *et al.*, 2001) for the purposes of both residential and commercial windows, and while a small fraction of these windows encompass energy-saving de-

sign features (such as low-emissivity coating, argon filling, and vacuum insulation), these solutions still ultimately render the window passive. Such large areas have massive potential for power generation and integration of self-powered electronics, sensors, and displays while retaining nearly identical optical properties. Considering the following: a 1 kW PV device can remove heat at approximately 3 kW from a building envelope during cooling, whereas the same device can be used to drive smart windows, averting an estimated electrical consumption rate of 110 kW; resulting in enormous energy savings (US Department of Energy, 2018; Deb *et al.*, 2001). With these metrics in mind, smart windows have sensibly received much attention over the years for their potential to be a completely transformative force in reducing energy consumption.

Electrochromism is a technique that has been been explored by many commercial interests and academic reports. Transparent surfaces like windows are able to transition between opaque and translucent states through an external potential. By blocking radiant heat from sunlight, households or other buildings can be insulated properly to reduce cooling loads, with a mechanism that fundamentally uses less power. Smart windows based on electrochromic mechanisms allow for the variation of transmittance through electrical current, and while the energy required to power and maintain a smart window is only 1/15 the power consumed of a standard nightlight (Bailey-Salzman *et al.*, 2006; Baxter and Aydil, 2005), smart windows account for an even smaller fraction of total windows manufactured worldwide. Part of the small demand is attributed to the fact that the product still represents an extremely niche interest.

The use of an external power source to operate each window ultimately reduces the freedom of architectural designers, having to accommodate for this requirement. However, a solution to this problem arrives from the attachment of a solar cell to the

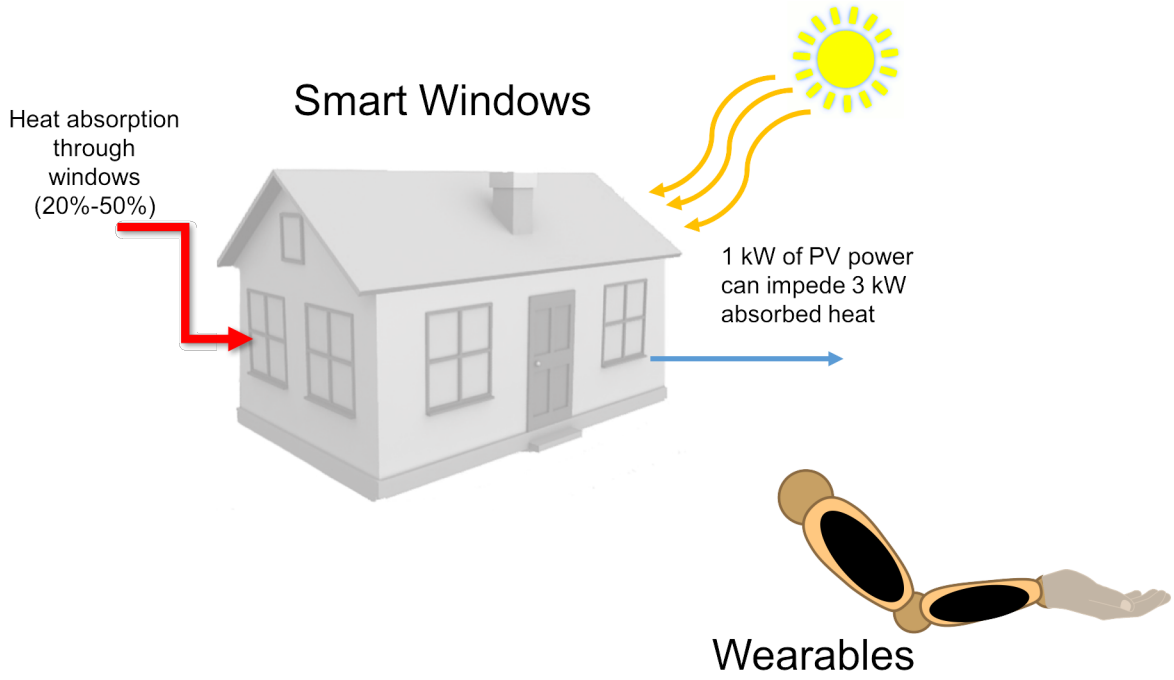

Figure 1.1: Visualization of household heat reflection and wearable applications of this work

smart glass, truly allowing for "off-the-grid" use. While the cell may not ultimately power a smart window, the amount of solar energy that drives it may be used to power a variety of other devices. At AM 1.5G, a power density (P_d) of 100 W/cm^2 will be available. As a conservative estimate, for energy conversion efficiency (η) of only 1%, a 1 meter by 1 meter window will potentially generate the following power density:

$$P_{d(1meter \times 1meter)} = P_d \times \eta \tag{1.1}$$

$$100\frac{W}{cm^2} \times 1\% = 1\frac{W}{cm^2} = 10,000\frac{W}{m^2} \tag{1.2}$$

i.e., a 1 m^2 window (which is still a relatively small area) can generate 10,000 W/m^2. As previously mentioned, since billions of square meters of glass for windows are manufactured worldwide, the potential payoffs for the incorporation of this smart technology are significant. Conventional (monocrystalline Si-based) solar cells on windows suffer mainly from aesthetic drawbacks—their cold, bulky feel may be one

issue, but the fact that they ultimately undermine the very purpose of a window (to see what is outside) is a more pressing issue. Thus, regardless of whether the solar cell is used to power a smart window or simply harvest energy, the cell must be relatively transparent, so as to retain the optical properties of a lucid window. Reports of optically transparent or semi-transparent Si-based photovoltaics have run into a problem of overall size reduction to less than 100 nm and 60 nm (Bailey-Salzman *et al.*, 2006; Baxter and Aydil, 2005); both indicate that this reduced thickness contributes to electrical shorts from the top contact with the PV, making the fabrication of large area devices extremely difficult.

The U.S. government has already invested considerable resources on "smart" windows, i.e., windows in which light transmission properties can be controlled by an external stimulus. Previous works have comprised a wide range of technologies to meet these needs, including electrochromic systems (Qi and Peterson, 2001) and even phase change glass materials that respond to heat pulses (Lee, 2006). However, these techniques require power to generate the desired effect; thus the need for a completely self-powered smart-window system becomes more evident, appealing, and urgent. A US company in 2006, NTERA Inc., created electrochromic dislayes based on TiO_2 nanoparticles coated with bis(2-phosphonoethyl)-4,4'-bipyridinium dichloride (Moller *et al.*, 2010). The company was able to achieve a high contrast ratio and fast switching time through the integration of white pigments from ZnO nanoparticles and optically active organic violgen. (Corr *et al.*, 2003). In 2007, Swedish company ACREO ITC fabricated flexible electrochromic displays using printed PEDOT:PSS and reported extremely fast switching times (Andersson *et al.*, 2007; Mannerbro *et al.*, 2008; Said *et al.*, 2009; Kawahara *et al.*, 2013). Another US company, Aveso Inc. (later acquired in 2011 by French Company Gemalto), produced embedded electrochromics for their "smart card" technology, that would randomly generate passkeys on a seven segment

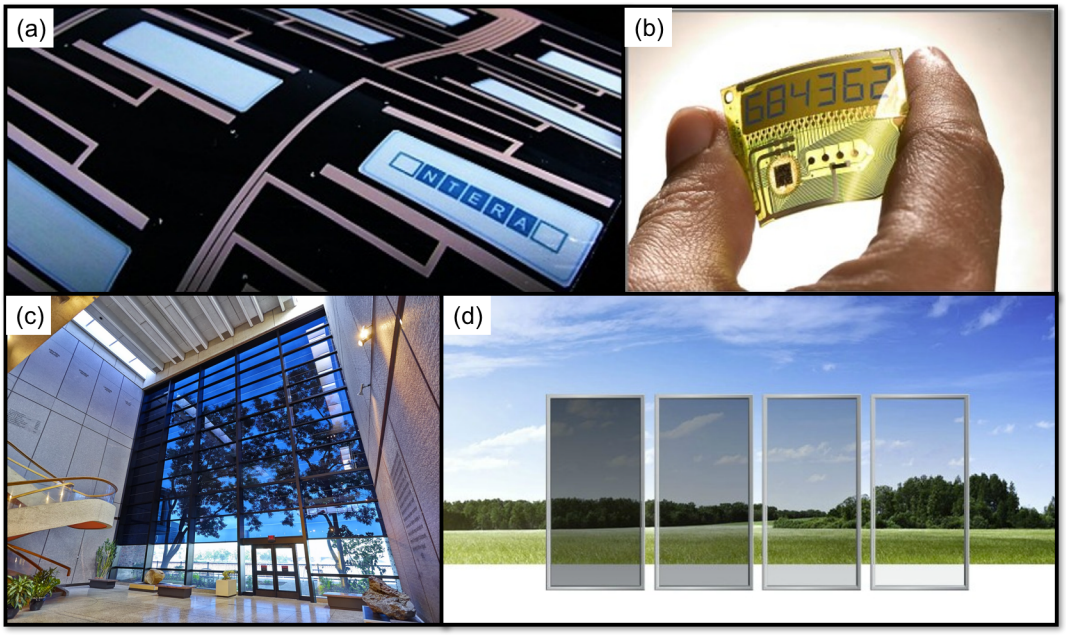

Figure 1.2: Electrochromic and smart windows products from (a) NTERA Inc. (Ganapati, 2010), (b) Aveso Inc. (IDTechEx, 2005), (c) Sage Windows (Spivak, 2016), and (d) View Inc. (Koerner, 2014)

display which they donned the One Time Password (OTP) technology. Based on organic pH indicators such as bromoscrescol purple, the technology created withstood operating times of up to 5 years (Babinec *et al.*, 2004). In terms of active building integrated electrochromics for glass, a US companies, Sage Windows and View Inc. released an electrochromic window panel which claims moderately fast switching time but at the expense of large power usage. Most recently, both of their flagship products have included Internet of Things (IoT) remote controlling to adjust daytime opacity.

1.1.2 Flexible Electronics

A field of major interest in recent years has been the fabrication of integrated circuits, not onto conventional substrates such as silicon (Si), but rather onto flexible, transparent, and even stretchable substrates. Indeed, tremendous progress has been made in flexible and transparent electronics in the last few years, as demonstrated

by the emergence of exciting flexible displays, e-papers, radio frequency identification card (RFID) etc. This has been feasible due to light weight, compact form factor, conformable, low cost, shock-resistance and potential versatility of multifunctionality. Beyond just information display, integrated multifunctionality on flexible substrates will certainly drive this field much further. UV resistant films and polymers used to block harmful radiation from entering buildings have been heavily commercialized. By itself, the material is simply a passive element, but possesses the capability of integrating many more features including complex transparent circuitry and photovoltaics. The flexible nature of the device also allows it to be attached to a variety of complex surfaces for smart window applications and energy harvesting. Conventional approaches for energy harvesting window production concentrate fabrication on rigid Si substrates, a material that is already so brittle that with additional thickness mildly adverse weather conditions may erode these devices if no external encampsulation is in use. Thus, the need for a flexible, mechanically resilient solar cell becomes more imperative. Flexible PVs with the required material characteristics certainly further the freedom of architectural designers. The inclusion of a self-powered stand-alone smart window or solar cell becomes a post-design thought of retrofitting, rather than a burden at the outset. Additionally, the mechanically flexible nature of the device substrate allows for contouring to complex surfaces such as curved windows or even soft fabrics such as a camping tent. Finally, the growth and popularity of Internet of things (IoT) enabled devices has unified the ability to remotely control the switching characteristics of devices (Xia *et al.*, 2012). IoT controllers will be integrated allowing for more robust control use-cases and greater consumer-level interest in such an integrated design. Realizing its importance in the consumer marketplace, the aforementioned Sage Inc. and View Inc. offer IoT functionality directly onto their electrochromic windows. The economic viability of flexible electronics is enhanced

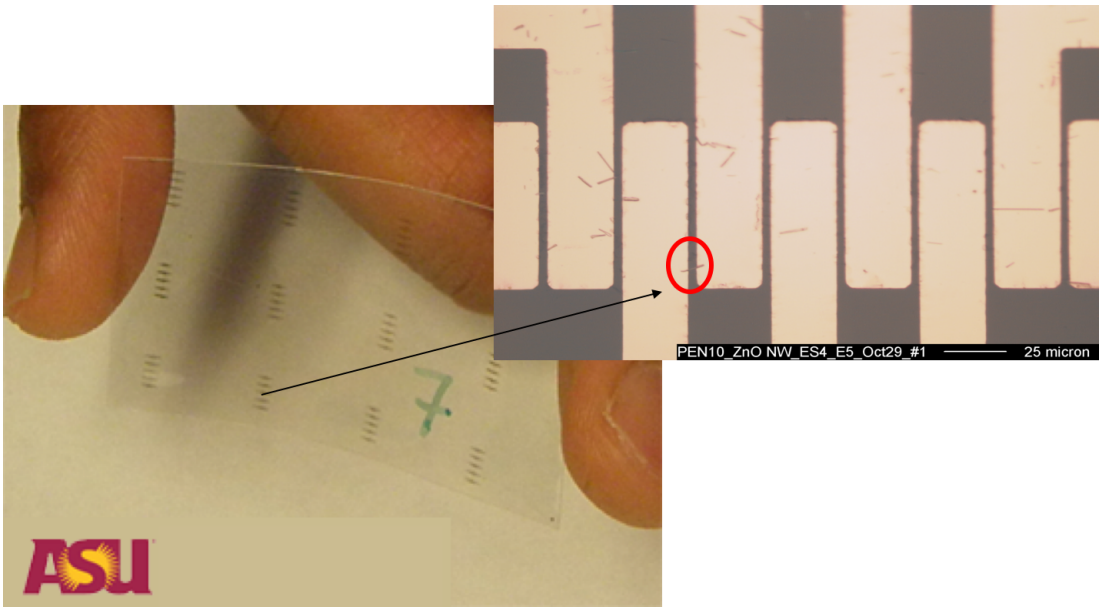

Figure 1.3: Flexible ZnO single-nanowire photodetectors

by the advent of fabrication techniques such as printing (Fan *et al.*, 2009). Various techniques such as contact printing or direct printing have allowed for large-scale integration of single-crystal inorganic NWs to be directly placed in specific locations. These methodologies of collecting such NWs into aggregates of well-ordered arrays have enabled the ability to mass-produce cohesive NW devices in a roll-to-roll fashion; a fabrication process that has the promise of being one of the most cost-effective ways to create a large volume of NW devices on a sheet of flexible substrate. Thus, the challenge to achieving self-powered flexible smart windows lie in fabrication of the reliable and reproducible photovoltaic devices for harvesting solar energy and electrochromic devices for shading sunlight. These devices must also demonstrate robustness (especially when subject to mechanical strain from bending), as well as large-scale, cost effective integration for potential commercialization.

1.2 Fundamentals

1.2.1 Metal-Semiconductor-Based Thin Film (Second Generation) Photovoltaics

Since A.E. Becquerel's discovery of electrical current generation from incident sunlight, Bell Labs' production of the first commercial solar cell in the 50s, and the energy crisis of the 70s, interest in photovoltaic technology had been sparse, and had largely been dominated by monocrystalline Si. Emerging thin film solar cells from the 90s and early 2000s sought to address the problems with crystalline Si, including high materials costs, as well as processing energy and costs. Materials for thin film-based cells have included amorphous silicon, CdTe, CIGS, of which introduced much lower processing temperatures and cost. Within this category, Schottky barrier (or surface barrier) solar cells have too been measured with cell performances comparable to homojunction or heterojunction cells. Within the enormously prolific field of silicon photovoltaics, even as early as the 70s, silicon based Schottky solar cells were reported to operate just as well as PN junction counterparts in terms of typical performance characteristics (J_{sc}, V_{oc}, and power conversion efficiencies) in both simulation and experimental studies (Fonash, 2010). Surface barrier photovoltaics can have promised even less processing steps and therefore less cost. Additionally, for materials in which dissimilar doping is exceptionally difficult (for example, ZnO), it is advantageous to implement Schottky-based solar cells.

Under equilibrium Schottky barrier-based solar cells can be characterized as as the diffusion of photogenerated minority carriers to a narrow surface or Schottky barrier. The difference between energy levels from differences in density of states create an electrostatic field and break symetry along the semiconductor surface inducing band bending, as shown in Figure 1.4(a). An insulator layer is introduced between the metal and absorber in order to serve as an electron blocking layer for self-recombination near

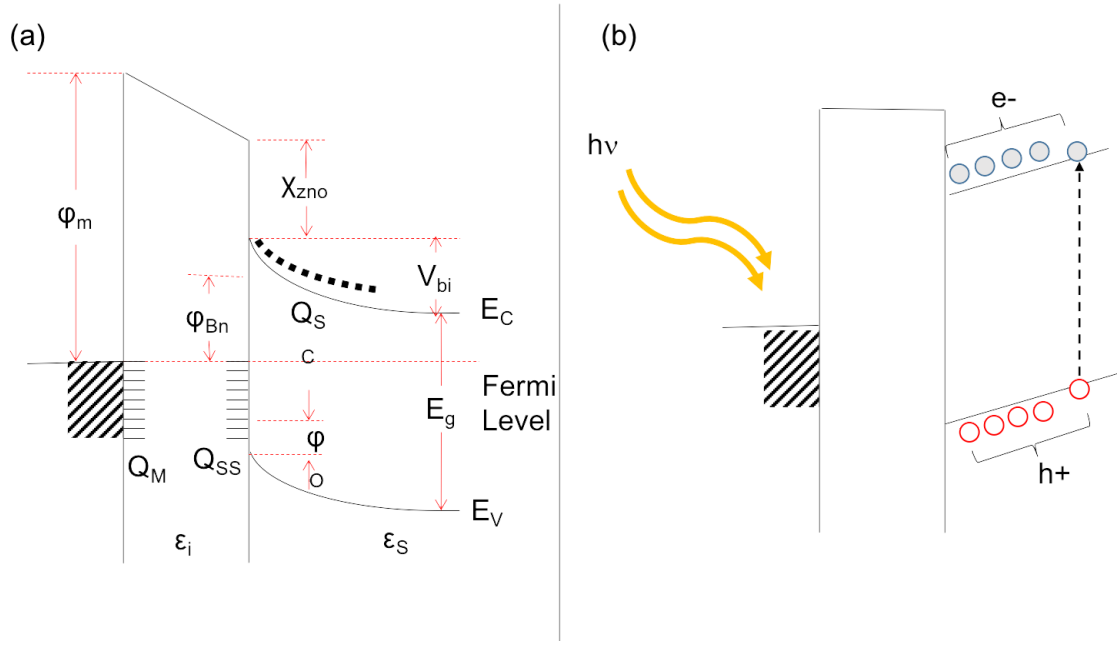

Figure 1.4: Band diagram of MIS Schottky Photovoltaic Diode in (a) equilibrium and (b) under illumination

the semiconductor surface. Under illumination, electrons are injected by thermionic emission into the metal layer, as illustrated in Figure 1.4(b).

1.2.2 Organic (Third Generation) Photovoltaics

Despite its promises for better or equal performance at low cost, interest in thin-film cells has been short-lived due to extremely slow development-leaving another category of solar cells to emerge, organics. In addition to the low cost of thin films, organic materials brought about even lower costs, thinner films, and even lower temperatures. Organic based solar cells have also exploded to an infinite variations of materials, material compositions, layer stacking, architecture, and even substrate independence, despite its poor stability. However, the combination of performance and production costs of previous generation solar cells are not scalable to the gigawatt or even terawatt scale, which has led many researchers to explore organic cells with great depth.

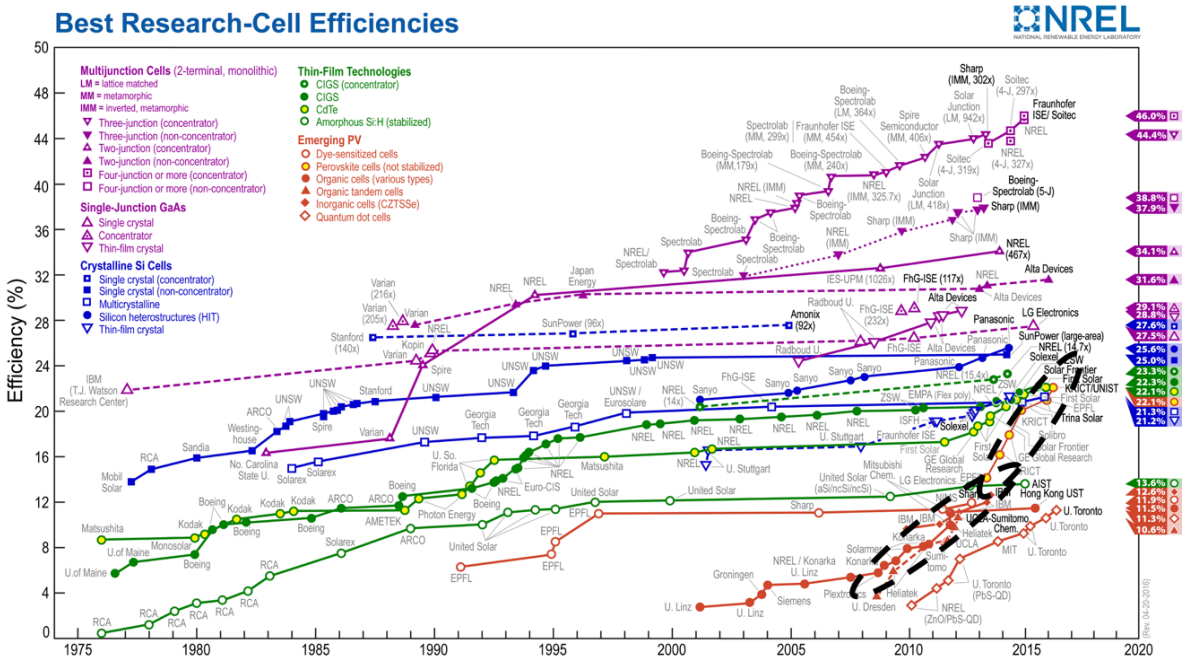

Figure 1.5: Comparison of power conversion efficient of dominant photovoltaic technology with organic solutions circled (NREL, 2018)

Organic based photovoltaic technologies have shown great promise and an even steeper learning curve over the last few years (Dong *et al.*, 2012; Khalil *et al.*, 2016) with power conversion efficiencies of 13.2% and lifetimes of over 5000 hours unencapsulated. Figure 1.5 presents a timeline of power conversion efficiencies for dominant photovoltaic technologies (Note: organic and perovskite typologies, indicating fastest rate or improvement, are circled). Organic polymers such as P3HT and PCDTBT mixed with fullerenes such as $PC_{60}BM$ for power harvesting have met incredible advances that allow for stand-alone atmospheric processing capabilities on tabletop inkjet printers, ultrasonic spray stations, sheet-to-sheet slot-die coater, roll-to-roll deposition with microgravure printing and slot-die coating, and laser scribing to enable monolithic interconnection and edge delete (Das *et al.*, 2014; Das and Alford, 2015; Das *et al.*, 2015; Steirer *et al.*, 2011; Ratcliff *et al.*, 2013, 2012). NREL has recently sponsored the SolarWindow CRADA whose aim is to "transparent electricity-

generating OPV film for glass and flexible plastics...low-capex, high-throughput manufacturing; and they generate electricity in sunlight and artificial, diffused, reflected, shaded, and low-light condition" (NREL, 2016).

The active absorbers in organic-based solar cells are shown in Figure 1.6 and can be characterized as a mixture of donor materials, conjugated thiophene monomers (represented with an S) with side chain esthers or alkyles (represented with an R), which produce π-electrons that can diffuse accross the entire polymer. Acceptor materials are composed of fullerenes that begin as C_{60} and undergo a series of reflux distillations with multiadducts to transform into $PC_{60}BM$, that allows solubility in typical solvents like o-dicholorobenzene or o-xylene. The acceptor and donor are allowed to dissolve within one another and form a bulk heterojunction. The typical device structure involves this bulk heterojunction sandwiched by a hole transport layer (such as PEDOT:PSS, or MoOx) and an electron transport layer (LiF or ZnO) which facilitates the extraction of exitonic charges, that have been generated and allowed to seperate under illumination. Top electrodes that contact the electron transport layer tend to be annodic (such as Al) and bottom electrode that addresses the hole transport layer tend to be cathodic (such as ITO). The bulk heterojunction is composed of microdomains of acceptors and donors, and the regularity of these domains is small enough to allow the hopping and transport of charges from generated excitons across the domains and to the contact so that they can be collected and converted to usable work (Krebs, 2008). This hopping process is highlighted in the band diagram of Figure 1.7(b).

1.2.3 Electrochromism

Electrochromism is a phenomenon in which ions insert or extract from a material, driven by an external potential, and results in a change in color or transparency.

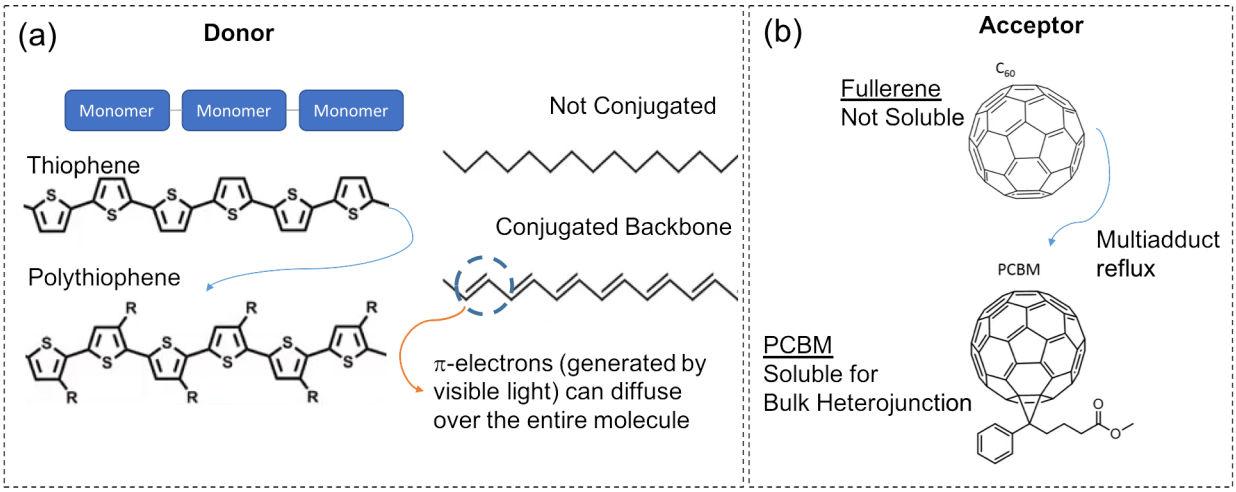

Figure 1.6: Chemical structures of (a) donor and (b) acceptor materials for organic photovoltaics

WO_3 has been among the most explored materials in this category because of its extremely stable switching and coloration mechanics with alkali ions such as Li^+. The device works on the same principle as an electrochemical cell, in which two electrodes are submerged in an electrolyte containing cations, shown below in Figure 1.8. As an external potential is produced between the annode and cathode, a reduction-oxidation reaction takes place leading to the movement and insertion/extraction of Li^+ ions, thereby causing coloration/bleaching (Figure 1.8 left/right). The underlying mechanism describing both coloration and bleaching can be expressed as:

$$WO_x + y(Li^+ + e^+) \rightarrow Li_yWO_x \tag{1.3}$$

$$Li_yWO_x - y(Li^+ + e^+) \rightarrow WO_x \tag{1.4}$$

The above reactions indicate a reversible switching of states through an external potential forming tungsten bronze, where y refers to the number of insertion sites. Electrochromic films are typically deposited on a conductive transparent substrate such as glass or a polyester like polyethylene terephthalate (PET) coated with ITO. The film is then cast with an electrolyte which serves to contain Li^+ ions and acts as

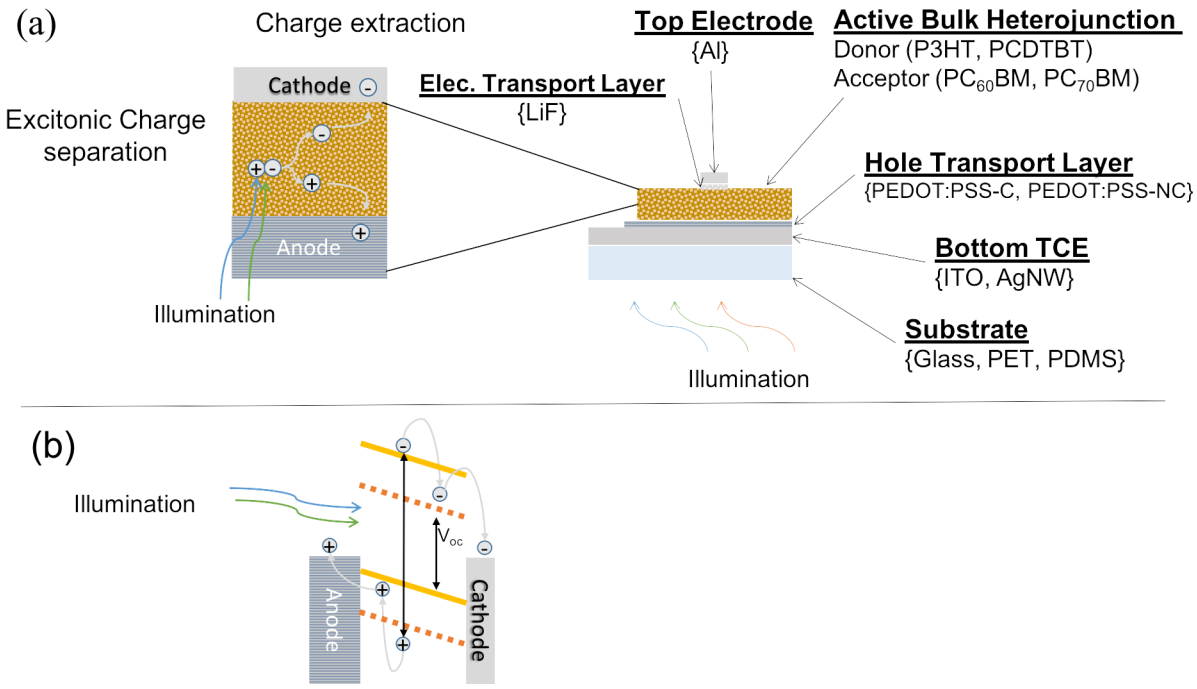

Figure 1.7: (a) Device structure and visualization of excitonic generation in bulk heterojunction. (b) Band diagram of bulk heterojunction solar cell.

an electronic insulator. Electrolytes can either be liquid or solid-state based on the molecular weight of the constituents. This device is then sandwiched atop another transparent electrode. The performance of electrochromic action depends on the electronic and ionic dynamics of the system. A combination of a highly electronically conductive materials with several active insertion sites, as well as a highly ionically conductive electrolyte ensures both fast switching times and high dynamic contrast between colored and bleach states.

1.3 Literature Review

1.3.1 Inkjet Printed Electrochromics

Inkjet printing is a technique that expels picoliter droplets of low-viscocity inks from the nozzle of the print head onto a two-dimensional plane. Inkjet printing is a

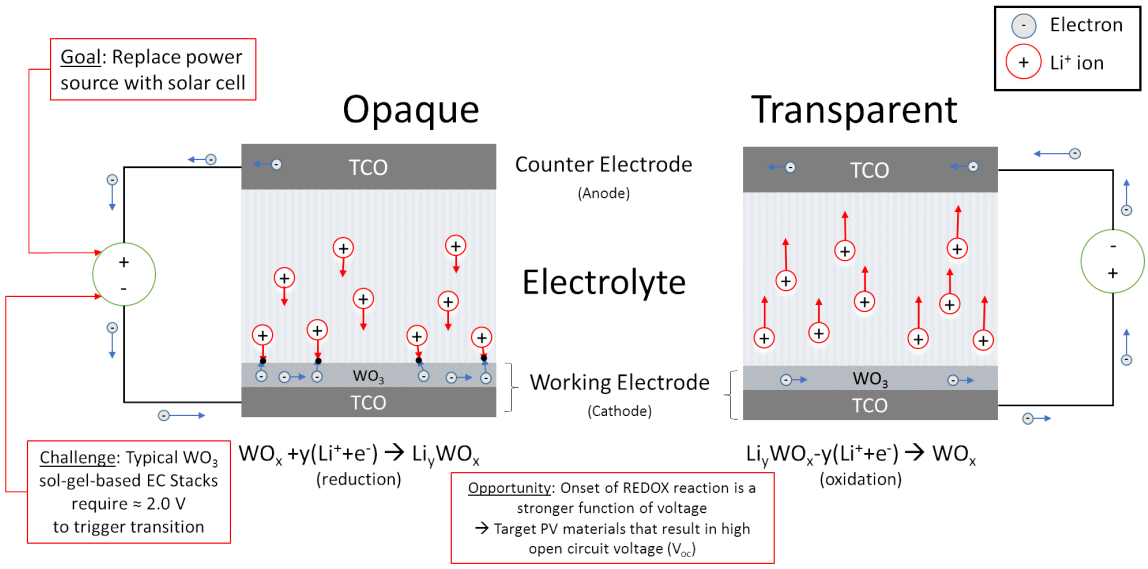

Figure 1.8: Electrochemical reaction of WO_x based electrochromic devices for reduction (left) and oxidation (right) reactions

attractive fabrication technique that encompasses additive patterned deposition processes. Inkjet printing allows for the deposition and patterning on a robust array of substrates, which can further be integrated with roll-to-roll industrial scale manufacturing (Angmo *et al.*, 2013; Yu *et al.*, 2012b). It allows for the rapid prototyping of devices and and products while allowing researchers to focus on the chemistry that constitutes them. Ink formulation is often a complicated process of optimizing viscosity, particle size, and surface tension such that the printed pattern does not exhibit deformation, cracks, problems with adhesion, or problems with expelling droplets. The choice of solvent is extremely critical for mixtures of printable particles because it keeps them in a bound liquid form before meeting the substrate as a droplet and becomes allowed to dry. Solvent selection must be considered in terms of its room temperature vapor pressure, such that premature evaporation on print heads is avoided, and so that post-deposition, the solvent can be burned off or decomposed completely. For this reason, volatile alcohols or short chain esters are preferred.

Inkjet printing has sparsely been applied to electrochromics. In 2009, NREL

began work on formulating printing techniques for windows using inorganic materials (Verrengia, 2010). They created a window with Li infused NiO as a counter electrode, and WO_3 as a working electrode and had moderate switching time with a 300 °C processing temperature. In 2012, Costa et al. printed Vanadium Oxide gels (Costa *et al.*, 2012a) and hydrated WO_3 nanoparticles (Costa *et al.*, 2012b) on PET, in which they found a "dual spectroscopic response depending on the applied voltage" which was attributed to the two crystalline states formed after hydration. A dual-phase α-$WO_3/TiO_2/WO_x$ was explored in a combination of amorphous and monoclinic WO_3 allowed for higher optical contrast due to more insertion sites, but also faster switching kinetics due to the crystalline phase. This effect was punctuated with TiO_2 (a cathodic material) NP loading reduced the transition potential needed to induce coloration (Wojcik *et al.*, 2012, 2014). In 2015, they tailored a variety of WO_3 nanostructures including hydrated orthohombic nanorods and nanowires, as well as monoclinic nanosheets, and correlated their structure and morphology to conductivity, fluid control, processing temperature and overall electrochromic performance (Wojcik *et al.*, 2015; Santos *et al.*, 2015). Reports of printed WO_3 sols on sintered Ag nanoparticles demonstrated a highly transparent substrate-independent realization (Layani *et al.*, 2014). In 2015, this work was continued with printing NiO and WO_3-based complementary electrodes and correlated performance with the number of printed layers (Cai *et al.*, 2015). Additionally, reports of an ink formulation that involved printing metallo-supramolecular polymers based on Fe and Ru was developed and demonstrated a vast array of color-changing electrochromics (Chen *et al.*, 2015). In 2016, reports of successfully printed WO_3-PEDOT:PSS based hybrid films in which high electrical conductivity was found to lead to faster response times, along with lowered redox potentials through the inclusion of PEDOT:PSS (Nguyen *et al.*, 2016).

1.3.2 Stretchable Electrochromics

Most recently, attention has been placed on stretchable devices for textiles and other wearables. Stretchability for electrochromics has been described as more challenging than achieving flexibility because the demand of a more mechanically robust device structure that considers elasticity as well as flexure. A stretchable device is expected to conform to non-planar surfaces without incurring performance degredation, along with being bent, twisted, and folded. This introduces further challenges for ITO as an electrode, which is quite brittle, and provides a common ground to the entire electrochromic film. Very few researchers have perused this idea, but the few reported implementations have been enabled by percolating AgNW networks embedded on stretchable substrates. In 2014, electrodeposited WO_3 layers on AgNW/PDMS substates, as well as embedding these substrates on textiles, and EC devices were shown to still function post-mechanical deformation (Yan *et al.*, 2014). In 2015, AgNWs were embedded on nano-cellulose paper and WO_3 was electrodeposited with an H_2SO_4 electrolyte, and was optimized against resistivity and transparency (Kang *et al.*, 2015).

1.3.3 Solar-Powered Electrochromics

Self-powered EC devices represent an interesting design goal toward the development of multifunctional and efficient smart windows. Self-powered electrochromic devices fit within a subset of research interests that work toward pairing energy harvesting devices with electrochemical storage devices (Zhong *et al.*, 2017). A smart window adds additional design constraints such as high visible-range transparency with a priority on optical modulation, transition time, and low power consumption. As previously mentioned, a report by NREL estimated that 1 kW of PV power can

remove approximately 3 kW of heat from a building envelope (Deb *et al.*, 2001).

In the late 90s, electrochromic devices were too expensive to scale up (Bechinger and Gregg, 1998), and similarly sized photovoltaic devices were not powerful enough. As a result, the scientific literature was dominated with device design proposals than actual realizations (Benson and Branz, 1995). Self-powered electrochromics have come in design flavors of vertical integration in which the electrochromic device is integrated directly on the device stack with the photovoltaic (largely dominated by photoelectrochromic cells with dye-sensitized solar cells), and laterally configured devices, in which the photovoltaic and electrochromic devices are seperate modules. The aforementioned issues with development of smart windows is to retain visibility functionality, which is why vertical integration has the problem of low optical modulation (Huang *et al.*, 2012a,b), in addition to low bleached state transparency. The integration of both systems in a lateral manner presents the most efficient generation of potential, and the most effective way of creating the most dynamic optical modulation range. In 2013, Xie implemented such a design and it was the first to integrate a double-pole double throw switch the reverse the external reaction potential (Xie *et al.*, 2013). In 2014, Dyer et al. created a vertically integrated tandem organic cells sandwiching an electrochromic device device, which was addressed with internal PEDOT:PSS electrodes (Dyer *et al.*, 2014). In 2016, another integration of photo-electrochromic device was released, transitioning glass from green to blue, with low optical modulation (Huang *et al.*, 2016). Table 1.1 summarizes some experimental processing conditions and materials for integrated self-powered electrochromic devices.

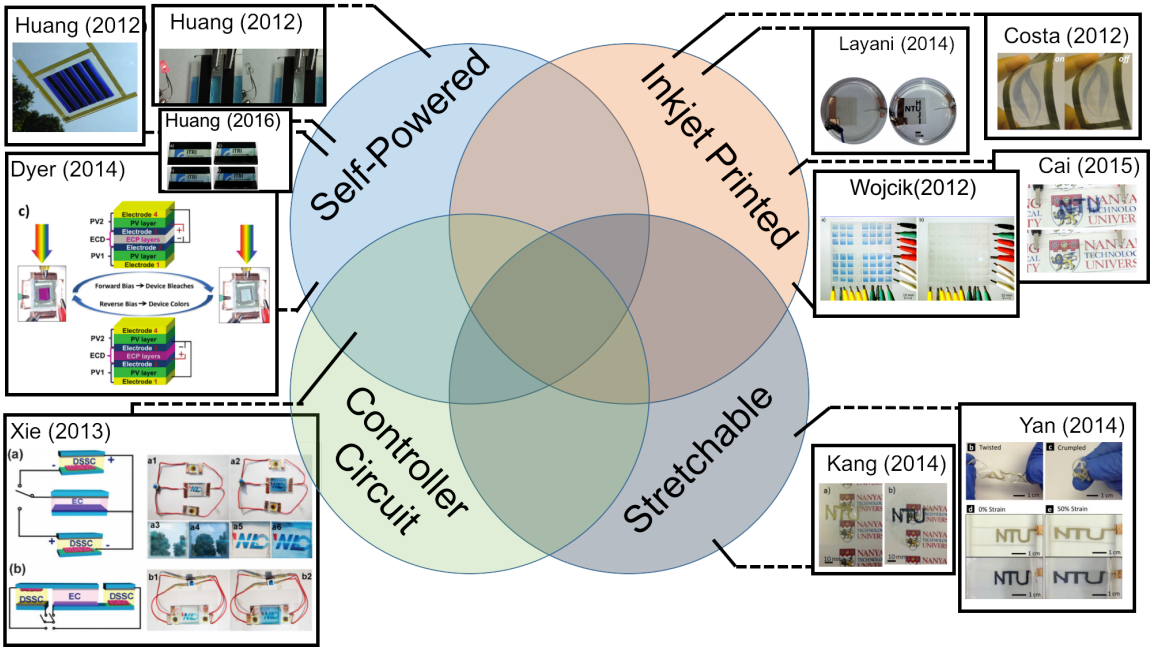

Figure 1.9: Categories and images of electrochromic devices reported in scientific literature

1.4 Research Goals

1.4.1 Smart windows, smart textiles, and the future

Previous studies on smart windows have focused on the fabrication using rigid substrate materials, use of flexible substrates opens new opportunities. Here we propose novel strategies to face the aforementioned challenges. A monolithic integration of organic-based photovoltaic cells and nanomaterials for electrocrhromic layers will be demonstrated using a flexible polymer as the substrate, to achieve self-powered smart windows and wearable electrochromics. The characteristics of the hybrid cells, such as transparency and switching time will also be determined. The final device structure is illustrated in Figure 1.10.

Device Orientation	EC Deposition	EC Material	PV Deposition	PV Material	Controller Circuit	Ref.
Vertical	Drop-cast	TMPD/ TBAB4	Sputter Coat	α-Si	None	Huang (2012)
Vertical	Electro-deposition	Prussian Blue	Sputter Coat	Si-TFSC	None	Huang (2012)
Lateral	Dip Coated	WO_3-$2{\cdot}H_2O$ films	Screen Printed	Si (DSSC)	DPDT	Xie (2013)
Vertical	Spray Cast	ECP-Magenta/ MCCP	Spin-Coat	PDPP3T: PCBM60	None	Dyer (2014)
Lateral	Sputtering	NiO/WO_3	MOCVD	InGaN/ GaN MQW	None	Kwon (2015)
Vertical	Spin Coat	Polyaniline: PSS	Sputter	Si-TFSC	None	Huang (2016)

Table 1.1: Comparison of implemented solar-powered electrochromic devices in scientific literature

1.4.2 Objectives

Despite maintaining a sufficiently high visible range transparency for window integration, a highly transparent solar cell results in lower utilization of the solar spectrum. Additionally, the power delivered by the photovoltaic device must be sufficient in order to instigate the reduction-oxidation reaction that initiates the electrochromic optical transition. Thus, such an electrochromic device should maintain a sufficiently

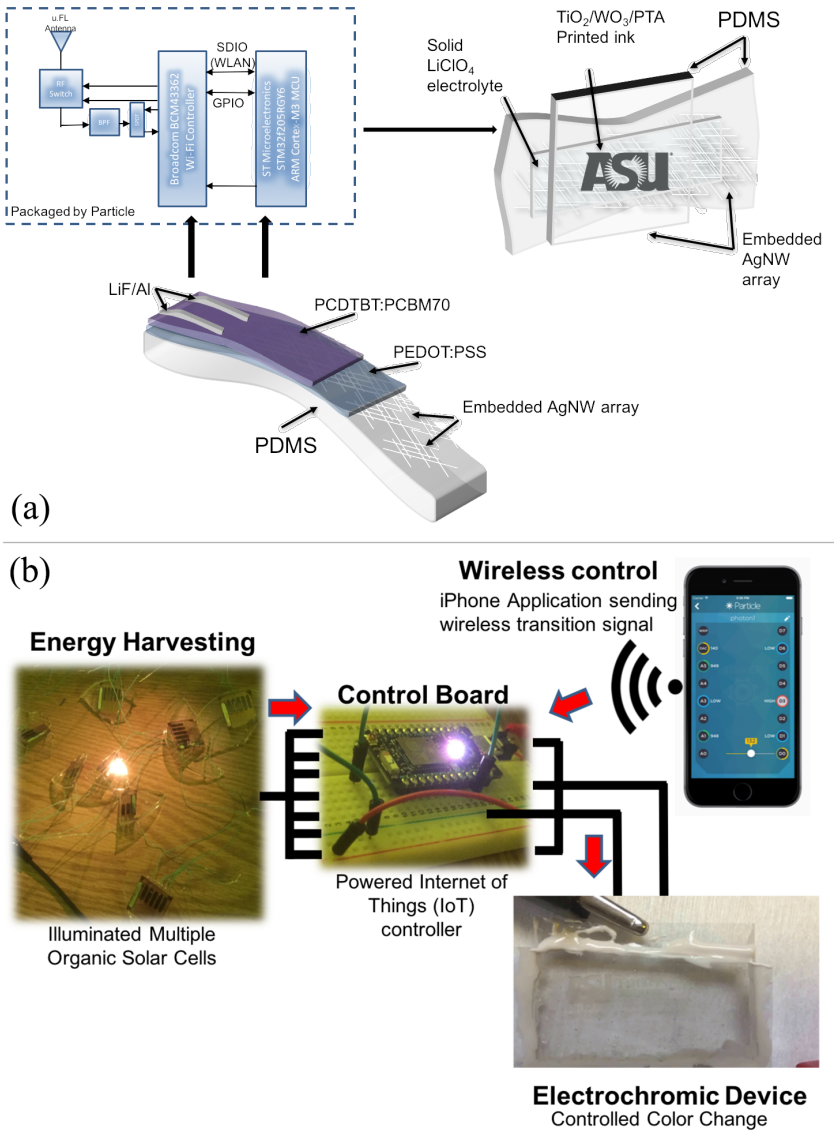

Figure 1.10: Final device structure (a) as a block system and (b) fully realized, encompassing electrochromic and photovoltaic components demonstrating material and system view of Self-powered IoT-enabled Electrochromic Device

low threshold voltage, while not sacrificing coloration and bleaching kinetics (transition time), as well as maintaining a sufficiently high optical density. When considered as a complete system, the photovoltaic device should consume an area much smaller than that of the electrochromic device.

With these design constraints in mind, integrating electrochromic devices with

photovoltaic devices requires an interdisciplinary approach toward tackling such a design objective (powering an electrochromic device with sunlight), while considering other design tradeoffs (switching time, optical modulation, power conversion efficiency). The purpose of this work is to extend the body of knowledge as related to stretchable, inkjet printed, self-powered, electrochromic devices, of which only few implementations have been reported. This work shall provide new solutions, expertise, and insights into the design considerations and restrictions that come about when integrating both technologies. It is the aim for this research to create simple, cost-effective, printable-based mixtures at lab-scale that would be compatible with large-scale R2R processes.

This study aims to focus on:

- Low temperature processing techniques
- Uniform printed films
- Material performance stability
- Mechanical integrity under physical stress
- High optical contrast
- High power conversion efficiency
- High visible spectrum transparency
- Low-cost materials and inexpensive synthesis

1.4.3 Research Approach

The topic of applied nanosciences, especially when applied to functional flexible devices requires an extraordinarily interdisciplinary approach. The methods described

in this work require the application of more than classical chemistry lab practicals and techniques, but also requires parsing and developing a deeper understanding of the results through informatics, data analytics, and other tools of specialized engineering backgrounds as well as academic bodies of knowledge. Figure 1.11 attempts to visualize the core aspects of the experimental research workflow, while expounding on the tools and techniques used in this work. The result of printed devices based on nanomaterials comes about from motivations from environmental sciences as applied to the built environment, materials science for understanding the properties of constituent materials needed to realize the devices, as well as device physics needed to model and predict their electrical behavior. This research, in addition to traditional engineering and chemistry knowledge, required the skills of CAD design to simulate circuit elements and to perform the necessary layout tasks required to realize them with the selected materials. The post-characterization understanding of results has come about from a quantitative approach, that is, translating and organizing observations to sets numerical values, such that statistical techniques and analysis can be applied to the data. This allowed statistical inferential techniques and modeling techniques to be applied in order to develop digestible understanding and insights of the research explored in this work. A subset of hypotheses are presented below, which illustrates the major scientific questions answered by this body of work.

- Chapter 2
  - Hypothesis: The thickness of insulator layers for MIS Schottky devices produces linearly increasing Schottky barrier height for ZnO between Schottky contacts.
    - *Observation 1*: Local maxima of Schottky Barrier height found across all tested metal contacts, with the exception of Aluminum
      - *Experimental Design*: I-V measurements with extracted Schottky barrier height (numerical response) as a function of oxide layer thickness (numerical), and contact metal (categorical).
      - *Fundamental Physical Interactions Uncovered*: Local maxima of Schottky barrier created by increased oxide barrier height. When

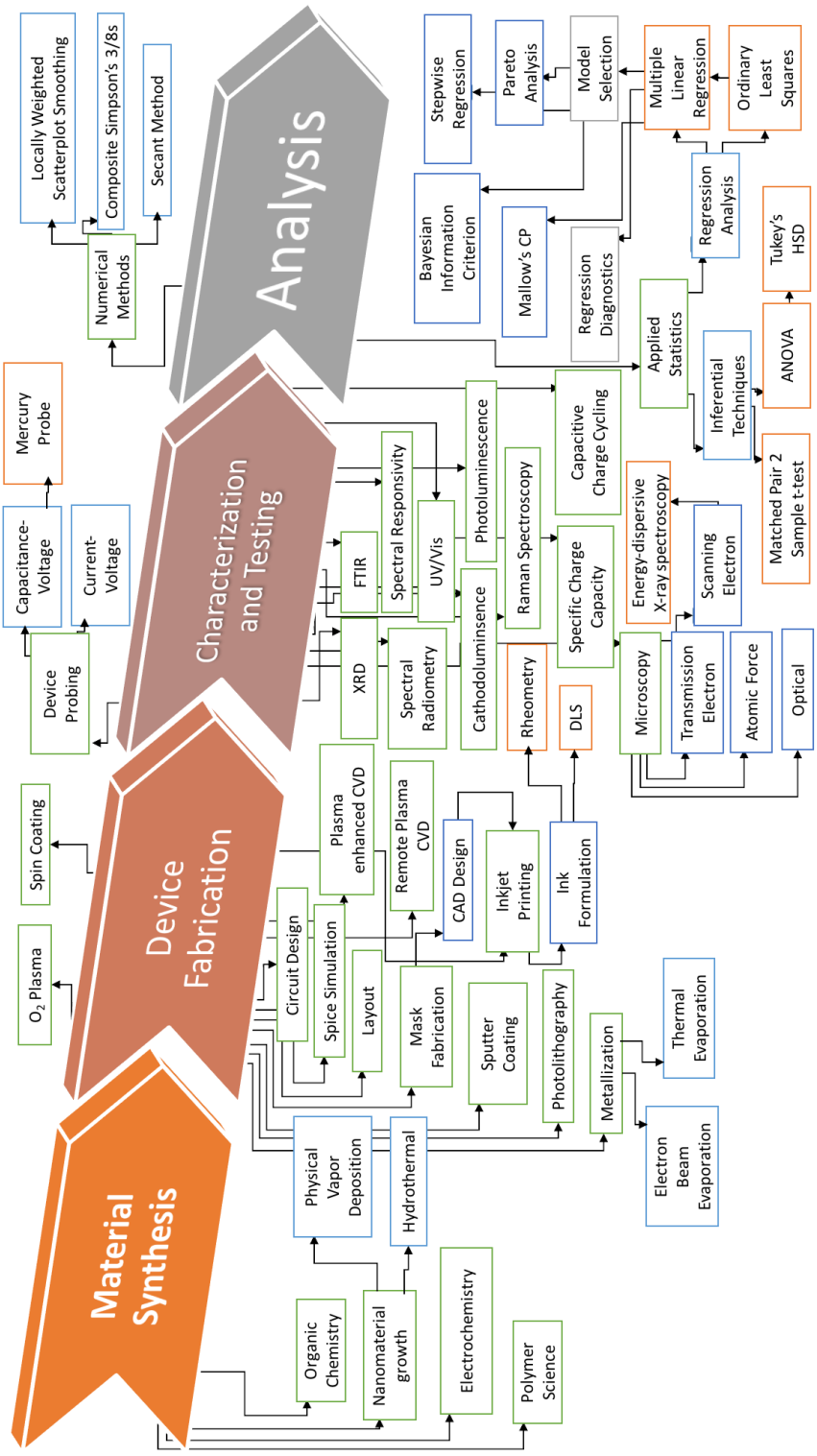

Figure 1.11: Visualization of device fabrication workflow and research techniques used in this dissertation

oxide thickness increases further, increased barrier width suppresses conduction. In the case of aluminum, at lower thicknesses, Al penetrates the oxide layer, bridging a conduction path to ZnO, which forms an ohmic contact. Increased barrier width suppresses conduction.

* *Observation 2*: Schottky Barrier height found to increase due to oxygen plasma treatment
  - *Experimental Design*: Schottky Barrier Height (numerical response) before and after oxygen plasma (categorical, 2-sample matched pair t-test), across two metal contacts (categorical), and two plasma powers powers (categorical).
  - *Fundamental Physical Interactions Uncovered*: Formation of Ag_2O and TiO_2 which have larger Schottky Barrier Height than unoxidized Ag and Ti. Passivation of ZnO and SiO_2 surfaces reducing tunneling.
* *Observation 3*: Photovoltaic action correlated with large Schottky barrier heights on ZnO thin films with low wavelength (UV) illumination for Ti/Ag and Ag oxygenated contacts
  - *Experimental Design*: IV measurements, PV performance parameters extracted (numerical response), as a function of contact geometry (categorical variable).
  - *Fundamental Physical Interactions Uncovered*: Explanation: Subband-edge illumination and large Schottky Barrier height through Ag and Ti/Ag oxidation favor spontaneous band splitting necessary for illuminated current.

- Appendix A
  - Hypothesis: Using PEDOT:PSS as a Schottky contact, or applying a Schottky contact to PEDOT:PSS will result in necessary solar power conversion to operate electrochromic devices.
  - Hypothesis: Current-Voltage Hysteresis behavior and transformations (Voc+/-, Isc+/-, intersection, loop areas) for organic semiconductors are a function of testing parameters (maximum voltage, illumination, voltage scan rate) and processing parameters (device size, choice of PEDOT:PSS conductivity grade, substrate).
    * *Observation 1*: Intercepts (current or voltage axis crossings) found to be a strong function of device size and illumination. Open circuit voltage found to shift for Al, and expand for Au.
      - *Experimental Design*: All processing and characterization conditions tabulated, extracted intercept points with secant method. Empirical model describing evolution of intercepts developed using Multiple Linear Regression (MLR).
      - *Fundamental Physical Interactions Uncovered*: Further explored the interaction between the Al/PEDOT:PSS interface and

Au/PEDOT:PSS interface and traced respective movement of intercept points. For short circuit current, an absolute increase of current is found to correspond to increased device areas, which was tied to the increase of absorbed light flux through each progressively larger device. In the case of V_{oc}, the logrithmic ratio of illuminated to saturated current determined the direction of V_{oc} shift, and because Au is less anodic than Al, open circuit voltage was found to decrease.

* *Observation 2*: Intersections between forward and reverse traces were found to have a non-origin shift as a function of device size, for non-conductive PEDOT:PSS on ITO substrates.
  - *Experimental Design*: All processing and characterization conditions tabulated, extracted intercept points with secant method. Empirical model describing evolution of intersections developed using Multiple Linear Regression (MLR).
  - *Fundamental Physical Interactions Uncovered*: First quadrant intersections which indicate further that a memcapacitance effect via slow states in PEDOT:PSS.
* *Observation 3*: Loop area increased as a function of device size and in most cases increased device sizes.
  - *Experimental Design*: All processing and characterization conditions tabulated, extracted hysteresis loop areas with composite Simpson's 3/8th method. Empirical model describing evolution of intersections developed using Multiple Linear Regression (MLR).
  - *Fundamental Physical Interactions Uncovered*: Larger device sizes and greater illumination increased the density of trapped carriers. With Au/Si on conductive PEDOT:PSS, this case was an exception because a cathodic material of heavily doped Si increased the conduction path through PEDOT:PSS, which increased the rate at which the electrons can detrap, thereby suppressing the formation of a hysteresis loop.

- Chapter 3
  - Hypothesis: Low reaction potential electrochromics can be achieved with TiO_2 NP loading.
    * *Experimental Design*: Mixture design of varying two types of WO_3 nanoparticles and TiO_2 nanoparticles were tested, switching characteristics and optical modulation recorded and tabulated.
      - *Observation 1*: Coloration density and contrast trade off with switching time and reaction potential, without the inclusion of TiO2.
      - *Observation 2*: W-TiO_2 led to greater optical modulation without significant compromise in switching time and reaction potential
      - *Fundamental Physical Interactions Uncovered*: W doped TiO_2 introduce more insertion and extraction sites for Li+ ions but due to

the higher coordination numbers and high electronegativity, bonding to O_2 radicals. The 6 courdination in WO_3 and 4 courdination of TiO_2 impedes electronic charge transfer, but will increase the number of insertion sites.

- Hypothesis: PCDTBT thin films can be applied to stretchable surfaces and can power electrochromic devices.
  - *Experimental Design*: Devices were fabricated composed of conductive and non-conductive PEDOT:PSS HTL and ITO/PET and AgNW/PDMS substrates. Solar cell performance parameters extracted from IV measurements and tabulated.
    - *Observation 1*: PCDTBT films exhibit larger power conversion efficiency with NC PEDOT:PSS.
    - *Fundamental Physical Interactions Uncovered*: The higher solid content and acidity of non-codncutive PEDOT:PSS allow the device to supress losses from laterial conduction between contacts.
    - *Observation 2*: PCDTBT films on AgNW/PDMS exhibit smaller power conversion efficiencies
    - *Fundamental Physical Interactions Uncovered*: Nonuniform distribution of AgNWs leads to larger series resistance from non-optimized conduction paths of percolation networks.

1.4.4 Merit

It is the intent of this work to describe the results of this Ph.D. research in a form that is standard and easily understood from professionals in the wide society of engineers. Systematic literature reviews and the parsing of experimental information have been entered in databases, and have been used to translate a set of facts into novel, actionable, and testable research work. This work uses the research and information of authors who came before it, which have included journal periodicals, conferences, and periodic reviews. The authors have made attempts to ensure that all work is repeatable by future researchers. A set of underlying hypotheses, discoveries, and scientific explanation is highlighted in each chapter, which further explains how the research work conducted expands each field respectively. The intellectual merit of this work lies in the interdisciplinary research approach, that has allowed for the exploration of a singular design problem in the context of multiple material systems,

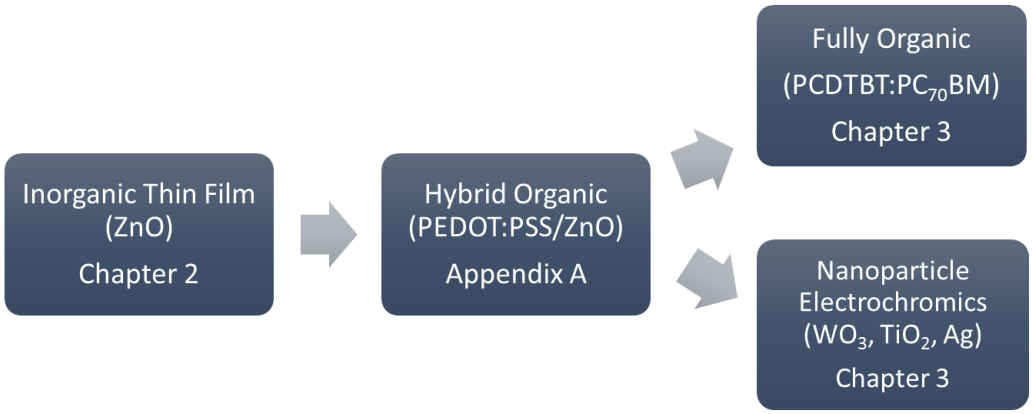

Figure 1.12: Organization of photovoltaic material systems and nanomaterials explored in this work.

multiple goals, and multiple trade-offs that must be reconciled with one another. Each study marks a series of intellectually rigorous stages including planning, executing, and analyzing. Each process requires a certain dedication toward learning, due diligence, discovery and confirming abstract expectations with evidence in the physical world. Once again, the tools and techniques acquired acquired to contextualize the torrent of information are detailed in 1.11.

The broader impact of this work is, in addition to the realization of smart windows that are self-powered, the advances will open up numerous opportunities using self-powered (solar) electrochromic devices. Furthermore, novel integration strategies will bring innovation from concept-to-commercialization at an accelerated pace in this rapidly growing field of organic and nanomaterial-based applications.

1.5 Organization of the dissertation

The organization of this thesis falls under the order in which the work was executed and completed. Chapters 2 and Appendix A discuss the work of power generation on ZnO thin films. Chapter 2 discusses ZnO based schottky devices and the processing conditions that lead to larger schottky barrier height and power conversion

efficiency. Appendix A characterizes, models, and discusses the hysteresis behavior exhibited with the inclusion of an organic conductive polymer, PEDOT:PSS. Chapter 3 discusses the organic and inorganic synthesis and fabrication of a self-powered electrochromic device on stretchable substrates. The organization of this thesis is combined upon the single learning tracks presented in Figure 1.12, which included nanomaterial integration on flexible and stretchable substrates and transparent, high open-circuit solar cell devices, which shows a culmination on both to the final implementation of a solar-powered smart window in Chapter 3.

Chapter 2

ZNO-BASED SCHOTTKY AND OXIDE MULTILAYERS FOR VISIBLE-TRANSPARENT PHOTOVOLTAIC DEVICES

2.1 Abstract

Zinc oxide (ZnO) films are suitable for low-power applications including smart-window harvesters and electrochromic devices. Initially, the scanning electron microscopy (SEM) microstructure of sputtered ZnO (2% Mn) semiconductor thin films and their spectral response of high transparency in the visible range were determined. Next, metal-semiconductor (MS), metal-insulator-semiconductor (MIS), and p-i-n heterojunction devices were fabricated, and their photovoltaic conversion under ultraviolet (UV) illumination was evaluated with and without oxygen plasma-treated surface electrodes. To achieve MS Schottky devices, noble and/or transition contact metals (Au, Ag, and Ti/Ag) were deposited, with Al as a control (ohmic) case. The Schottky parameters were fitted against the generalized Bardeen model, and density of interface states ($D_{it} \approx 8.0\times10^{11}$ $eV^{-1}cm^{-2}$) and the neutral level ($E_o \approx$ -5.2 eV) were estimated. These devices exhibited photoconductive behavior under UV illumination (λ=365 nm); note, low-noise, Ag-ZnO detectors exhibited the highest performance, with responsivity (R) and photoconductive gain (G) of 1.93×10^{-4} A/W and 6.57×10^{-4}, respectively. Confirmed via matched-pair analysis, post-metallization, oxygen plasma treatment of Ag and Ti/Ag electrodes resulted in an increase of the Schottky barrier height, which maximized with a 2 nm SiO_2 electron blocking layer (EBL), coupled with the suppression of recombination at the metal/semiconductor interface. Also, the blocking of majority carriers, and the unaffected short circuit cur-

rent due to tunneling of minority carriers, resulted in an open-circuit voltage (V_{oc}) of 1.2 V and short circuit current density (J_{sc}) of 0.68 mA/cm^2 for interdigitated devices under high energy, monochromatic UV-C illumination.

2.2 Introduction

Building-integrated photovoltaics (BIPV) have garnered immense attention for research and commercialization since building facets, such as windows and skylights, represent underutilized spaces for the incorporation of solar cells (Petter Jelle *et al.*, 2012). Due to its long development history following the microelectronics industry, silicon technology has largely dominated this BIPV platform (Swanson, 2006). Since the development of the earliest Si p-n junction solar cells, comparably performing metal-semiconductor (MS) Schottky (Charlson *et al.*, 1972) and metal-insulator-semiconductor (MIS) photovoltaic devices (Card, 1977; Thomas *et al.*, 1980) have also come under extensive scrutiny; for the former, open circuit voltage (V_{oc}) and power conversion efficiency are highly correlated with Schottky barrier height (Zhu *et al.*, 2012). Moreover, since Si and other narrow gap, inorganic semiconductors are opaque in the visible range, varieties of functional challenges present themselves for replacing passive transparent surfaces with "smart," energy harvesting windows (Mercaldo *et al.*, 2009).

Wide-gap materials, such as zinc oxide (ZnO), have gained traction toward meeting the aforementioned needs due to their visible-range transparency (Ozgur *et al.*, 2005). Additionally, analytical transport models have suggested that with large absorber bandgap energy, high open-circuit voltage (V_{oc}) can be achieved (Bowden and Honsberg, 2014). Certain models (after disregarding thermal, resistive, and optical losses) have determined a theoretical limit of single-junction visibly transparent solar cells composed of wide-gap materials (coupled with absorption in the near infra-red

spectrum); predicted power conversion efficiencies (PCE) are as high as 21% (Lunt, 2012). Metal-semiconductors (MS) and metal-insulator-semiconductor (MIS) barriers on ZnO have been a topic of vast exploration (Brillson and Lu, 2011), and furthermore, ZnO is an excellent absorber of ultraviolet (UV) radiation, as noted by the realization of UV photodetectors (Soci *et al.*, 2007; Yu *et al.*, 2012a; Azhar *et al.*, 2018) and UV photocatalysts (Ullah and Dutta, 2008; Mahmood *et al.*, 2011).

While photovoltage has been shown to vary with metal work function for bulk ZnO (Li *et al.*, 2009), achieving transparent photovoltaics has led to enormous efforts in other oxide-based semiconductor absorbers (Rühle *et al.*, 2012). In the context of conventional solar cells, ZnO has typically been integrated as a thin-film "window" material; and nanostructured ZnO have been utilized for their light trapping and light scattering properties (Hagiwara *et al.*, 2001; Son *et al.*, 2012). Weak photovoltaic conversion utilizing ZnO absorbers under ultraviolet illumination has also been discussed in some reports (Nakano *et al.*, 2008; Amiruddin and Kumar, 2016). Most recently, interest in scavenging energy from UV radiation has become of great interest for structural and vehicular window integration, and have largely focused on absorber-tuned polymer-based solar cells composed of ZnO-C_{60} core-shell quantum dots (Son *et al.*, 2011), fluorophore-doped dye-sensitized solar cells (Lin *et al.*, 2015), and PTB7:PCBM (Liu *et al.*, 2013; Lim Dong Chan *et al.*, 2017). While purely inorganic material-based devices are considerably less reported, interests have arisen from p-GaN/MgO/n-ZnO layers exhibiting 0.46% PCE (Yang *et al.*, 2016b) to ZnO/NiO/Ag layers demonstrating PCE as high as 6% (Patel *et al.*, 2017), under ultraviolet illumination. Although the terrestrial energy content of UV radiation is fundamentally small, power conversion through limited absorption may supply enough energy for applications that require a relatively low operating point, such as electrochromic windows (Davy *et al.*, 2017).

In this study, the microstructral, optical, and electronic properties of sputtered ZnO thin films in varying device configurations (MS, MIS, and p-i-n heterojunction) were analyzed. The electrical response as a function of Schottky barrier height, varied by metal-semiconductor work function differences, was used to estimate the density of interface states (D_{it}) and the surface neutral level (E_o). To address this, the effect of SiO_2 electron blocking layer (EBL) thickness toward suppressing metal/semiconductor interface recombination was examined. In addition, post-metallization oxygen plasma treatment was carried out to maximize the effective barrier potential experienced by carriers. Finally, the photovoltaic and photodetection performance for assorted electrode patterning of Ag_2O and Ti_x/Ag_2O electrodes, differentiated by illumination energy, are reported. A brief discussion of the limitations in forming a robust model in completely describing transport phenomena in the specified oxide multilayers is also presented.

2.3 Experimental Details

Glass microslides coated with indium tin oxide (ITO, Delta Technologies, CG-61IN) were submerged in Piranha (70% sulfuric acid, 30% hydrogen peroxide) for 10 minutes to remove organic contaminants. Varying thicknesses of ZnO (2% Mn) were deposited via RF magnetron sputtering (Lesker PVD 250) at 400 W in 1×10^{-6} Torr O_2 ambient. Surface microstructure of ZnO films was characterized with Field Emission Scannning Electron Microscopy (FESEM, Hitachi S4700-II), operating at 15 kV excitation. Visible light transmittance was measured with a halogen broad band white light source (Princeton Instruments TS-425) and concave grating spectrometer (StellarNet BLACK-Comet). Fourier transform infrared spectroscopy (FTIR, Nicolet 800) system was used to characterize transmittance in the wavenumber range from 400 to 4000 cm^{-1} using a potassium bromide (KBr) beam splitter. In order to

passivate the ZnO surface, all samples subsequently received oxygen plasma (Tegal PlasmaLine Asher) treatment of 250 W for 15 minutes. A Plasma Enhanced Chemical Vapor Depositor (PECVD, Oxford 100) was used to coat the ZnO surface with thin (2 nm and 5 nm) SiO_2 electron blocking layers (EBL). Surface electrodes including Al, Au, Ag and Ti/Ag (250 nm each, 5 nm/245 nm Ti/Ag) were deposited atop the coated and uncoated ZnO films via electron beam evaporation (CHA SE-600). Device structures analyzed included adjacent circular patterns of varying diameters (300-700 μm diameter) in order to control for device area in barrier height determination with current-voltage (I-V) measurements (Keithly 4200). After metallization and initially-illuminated electrical characterization, a second oxygen plasma treatment was undertaken on four blocks of Ag and Ti/Ag device test groups (without EBL) at 50 W for 5 minutes and at 250 W for 5 min; the contacts visibly darkened from reflective to completely opaque, indicating the formation of Ag_2O (Bock *et al.*, 2004). These devices were subsequently re-measured, and the increased Schottky barrier heights were inferentially evaluated as matched pairs. Additionally, an interdigitated grid (0.5 cm $\times$ 1 cm, 1 μm pitch) shown in Fig. 2.1(b), was photolithographically patterned on ZnO thin film devices for photovoltaic measurement under monochromatic UV-A (365 nm) and UV-C (254 nm) illumination (UVP EL Series). A final schematic of the device fabrication workflow is illustrated in Fig. 2.1(a), highlighting the primary experimental design parameters. Post-processing of data, which included data transformation, parameter extraction, analysis, and visualization were performed in R language with the ggplot2 library.

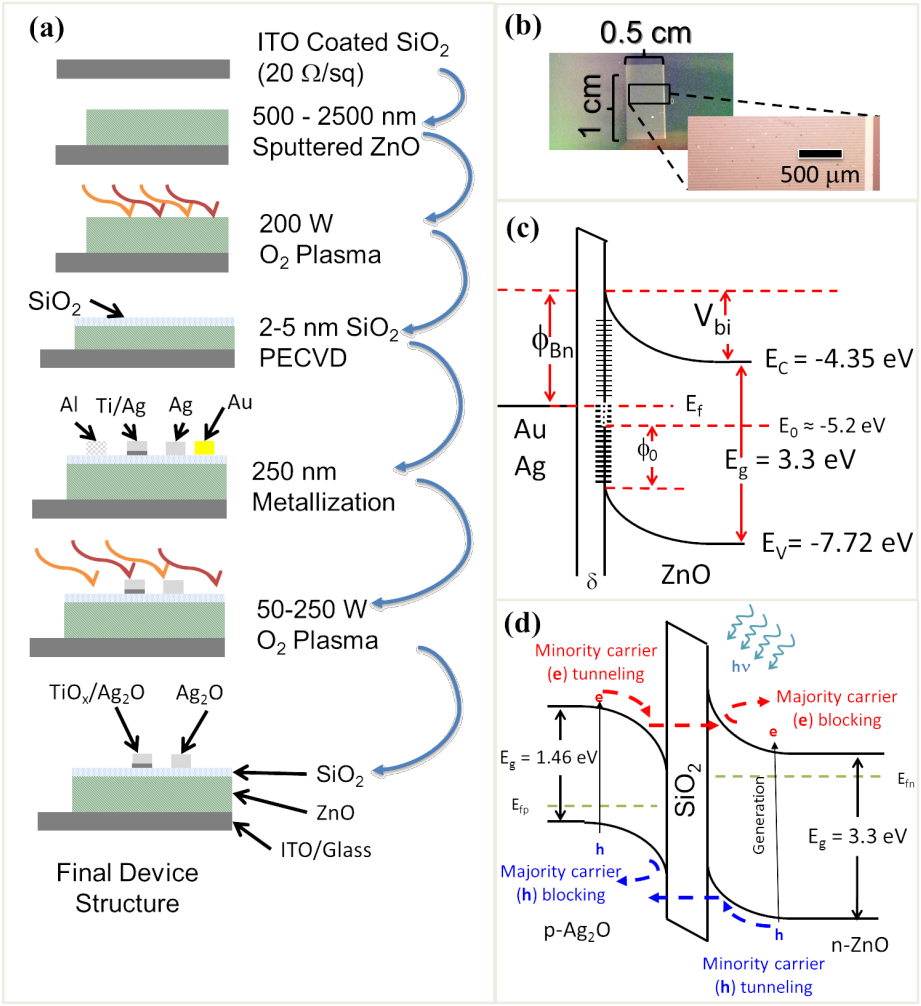

Figure 2.1: (a) Schematic of device fabrication procedure. (b) Image of final device structure with grid pattern (inset: optical microscope image of device). (c) Equilibrium energy band diagram of high interface state density Schottky-Bardeen device configuration with estimated surface neutral level. (d) Energy band diagram of final p-i-n heterojunction device with Ag_2O contacts illustrating majority carrier blocking, minority carrier tunneling transport mechanism under forward bias and UV illumination (Note: energy levels and band offsets not to scale).

2.4 Results and Discussion

2.4.1 Optical and Microstructural Properties

The visible-range spectral transmittance of ZnO films are illustrated in Fig. 2.2(a). As previously reported for ZnO and other wide-gap semiconductors, the transmittance

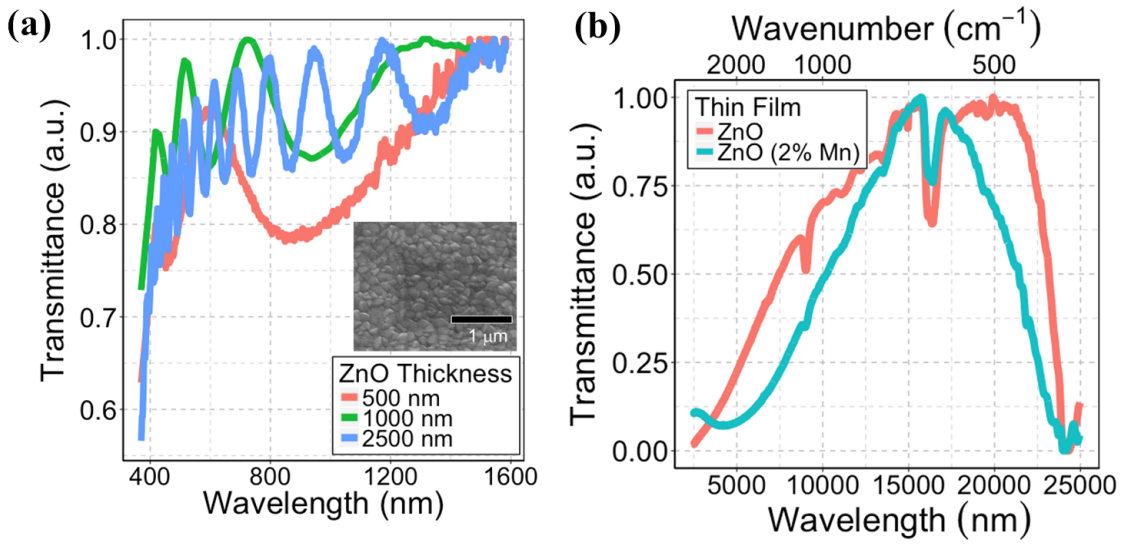

Figure 2.2: (a) Visible range transmission spectra of ZnO thin films. Increased film thickness results larger frequency periodic signature with local minima and maxima corresponding to constructive and destructive integer-factor wavelengths (inset: Scanning electron micrograph of sputtered ZnO) (b) FTIR (mid-IR) spectra of ZnO and ZnO (2% Mn) films (red and teal trace respectively).

in the visible spectrum is found to be high, with a slight attenuation for increased film thickness due to larger penetration depth (Song *et al.*, 2002). While a small component of the signal is lost due to reflectance, the transmission profile at and above 370 nm indicate excellent absorption in the UV range, the onset of which begins at the band edge of ZnO. Increased film thickness also results in a pronounced higher frequency periodic interference signature stemming from path differences of integer-factor wavelengths, with local minima and maxima corresponding to destructive and constructive interference, respectively. An empirical dispersion relationship for ZnO (Bond, 1965) is expressed in (C.1), and the thickness is extrapolated from interference fringes (Tuzemen *et al.*, 2009) from (C.2). The thicknesses are confirmed as 504 ± 15.6 nm, 1039 ± 28.5 nm, and 2503.1 ± 37.8 nm, respectively.

$$n^2 = 2.81418 + \frac{0.87968\lambda^2}{\lambda^2 - 0.3042^2} 0.00711\lambda^2 \tag{2.1}$$

$$t = \frac{\lambda_1 \lambda_2}{2[n(\lambda_1) \times \lambda_2 - n(\lambda_2) \times \lambda_1]} \tag{2.2}$$

The surface microstructure of the ZnO films is shown in the scanning electron micrograph inset of Fig. 2.2(a) and the presence of grains typical of sputtered ZnO thin films are observed. These columnar, grains on the film surface have been attributed to the high power of Zn^{2+} and O^{2-} ions, from the sputtering process, irregularly adjusting their bond length and settling in various bond directions, promoting periodic segregated nucleation, and forming as distinct grains (Yu *et al.*, 2005).

The vibrational bands in the IR range for pristine ZnO films and Mn (2%)-doped ZnO films are shown in Fig. 2.2(b). The peak at 545 cm^{-1} in both spectra has been attributed to the stretching mode of ZnO, but the shift of the secondary peak at approximately 538 cm^{-1} in Mn-doped ZnO indicates a perturbation in the Zn-O-Zn network from the incorporation of Mn (Hao *et al.*, 2012). Previous studies for photocatalytic applications have linked the increased visible range absorption to the relative concentration of Mn^{2+} as a substitutional dopant for Zn^{2+}. This has been attributed to the electron transitions from the sp-d exchange interactions between the Mn^{2+} ions and photogenerated carriers in ZnO (Lu *et al.*, 2012).

2.4.2 Electrical and Optoelectronic Properties

The current-voltage characteristics of two-terminal, metal-semiconductor (MS) Schottky devices are shown in Fig. 2.3. The choice of contact metal determines conductivity, as well as rectifying or ohmic behavior. As illustrated in Fig. 2.3(b), ohmic conductivity is exhibited for Al, whereas Ag, Au, and Ti/Ag exhibit asymmetry across the origin. Applying the thermionic emission model, expressed in (C.4), with the ZnO Richardson constant A^* taken as 32 $\frac{A}{cm^2 K^2}$), to measured current-voltage responses without illumination, a series of Schottky Barrier heights and ideality factors (2.4)

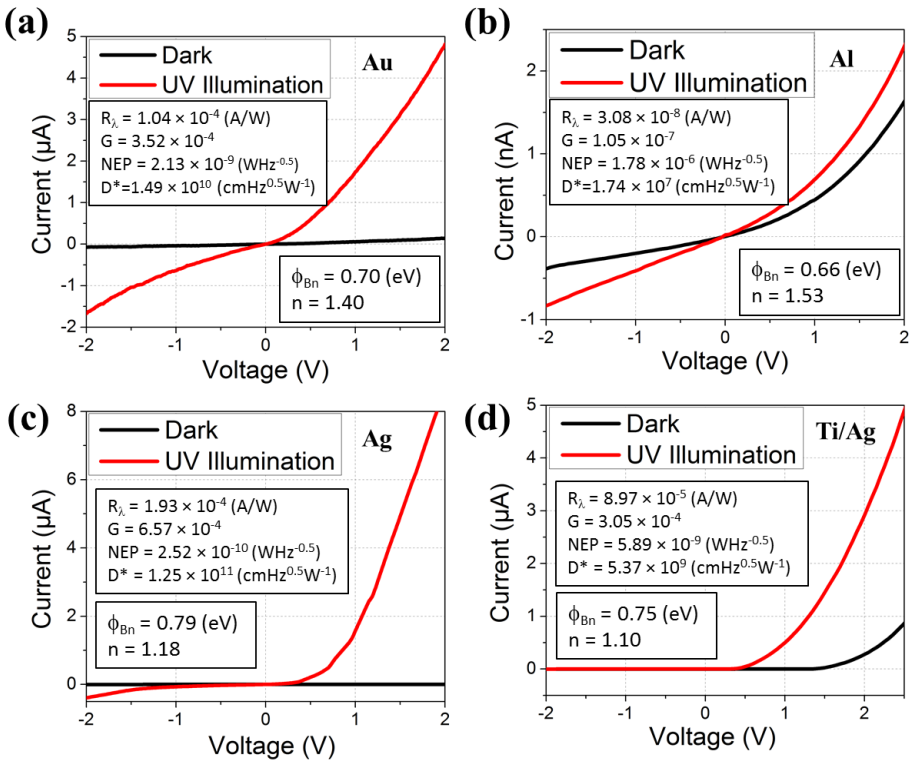

Figure 2.3: Current Voltage response of ZnO films in dark (black) and under UV illumination (red) with (a) Au, (b) Al (nA response), (c) Ag, and (d) Ti/Ag Shottky contacts. Insets for each electrode: (1) median extracted Schottky barrier height along with median ideality factor and (2) photodetection performance and noise parameters.

were extracted for each test electrode, and are appended to each plot in Fig. 2.3.

$$\phi_B = \frac{kT}{q} ln(\frac{A^* T^2}{J_o}) \tag{2.3}$$

$$n = \frac{q}{kT} \frac{dV}{d(ln(J))} \tag{2.4}$$

The results of pre-plasma treated barrier height extractions are consistent with previous studies on treated and untreated Zn or O polar faces, which have indicated Schottky barrier heights in the range of 0.6 eV - 0.8 eV (Ozgur *et al.*, 2005) despite measureable metal-semiconductor workfunction differences. This behavior has been attributed to the dominance of Fermi level pinning by a high density of interface

Material Structure (Synthesis/Deposition Technique)	D_{it} ($eV^{-1}cm^{-2}$)
ZnO:Al Thin Film (sputtered) (Oh *et al.*, 2006)	1.66×10^{10} - 4.46×10^{11}
SiO_2/ZnO Thin Film (sputtered) (Nandi *et al.*, 2003)	6.84×10^{11} - 8.52×10^{11}
ZnO Thin Film (hydrothermal/sol-gel) (Yakuphanoglu, 2011)	1.38×10^{8}
Au/ZnO Nanorod (hydrothermal) (Hussain *et al.*, 2012)	1.9×10^{8}
ZnO Thin Film (electrodeposition) (Aydogan *et al.*, 2009)	17.3×10^{13}
ZnO Nanorod (hydrothermal) (Faraz *et al.*, 2012)	7.98×10^{10} - 3.74×10^{11}
ZnO:Mn Thin Film (sputtered, this work)	8.0×10^{11}

Table 2.1: Comparison of interface state densities as reported for ZnO material systems

states (D_{it}) due to point defects over metal induced gap states (Allen and Durbin, 2008). To describe the interface transport behavior of measured ZnO thin film devices, a modified set of linear systems based on Cowley and Sze's generalized case of the Bardeen model (Cowley and Sze, 1965), expressed in (2.5), was evaluated with extrapolated parameters and known quantities (note: this model is only applied to analysis of metal-semiconductor devices, i.e. without EBL). Modeled in Fig. 2.1(c), the neutral level (E_o) is estimated to be approximately -5.2 eV, and the interface state density (D_{it}) is approximately 8.0×10^{11} $ev^{-1}cm^{-2}$, which is in agreement with reports of interface state determinations for ZnO with deep-level transient spectroscopy (DLTS), summarized in Table 2.1.

$$\begin{bmatrix} \phi_{Bn(Ag)} \\ \phi_{Bn(Au)} \end{bmatrix} = \frac{1}{1+\frac{qD_{it}\{\delta\}}{\epsilon_r\epsilon_o}}\left(\begin{bmatrix} \phi_{m(Ag)} \\ \phi_{m(Au)} \end{bmatrix} - \chi\right) + \left(1 - \frac{1}{1+\frac{qD_{it}\{\delta\}}{\epsilon_r\epsilon_o}}\right)(E_g - (E_o - E_v)) \quad (2.5)$$

Previous reports investigating Ti/Au, Ti/Al, and Ti/Pt with alloying post-anneal (Brillson and Lu, 2011) have demonstrated ohmic behavior. Brillson had noted that

Ti and Al react strongly with chalcogenides, forming alloyed n-type barriers with generally ohmic behavior exhibited, and that analysis was later extended to oxide-based systems (Brillson, 1982; Brillson and Lu, 2011). However, in this work, Ti/Ag exhibits rectification, which suggests that thermionic emission dominates. Considering the 5 nm thickness of Ti (as compared to that of the 1 μm ZnO thin film), Ti spontaneously forms into a kinetically-limited semiconducting TiO_x layer, due to its high negative formation energy, by scavenging oxygen from ZnO (Dey *et al.*, 1995). The net effect is a metal-semiconductor interface between Ag and TiO_x, thereby increasing the measured barrier potential, especially evident in post-metallization oxygen plasma treated layers.

Devices in the metal-semiconductor configuration did not exhibit photovoltaic behavior under UV-A (λ=365 nm) illumination, however, a photoconductive effect was observed. The spectral responsivity (R_λ) and photoconductive gain (G), key metrics distinguishing photodetector systems, are defined according to relationships expressed in previous reports (Yu *et al.*, 2012a; Azhar *et al.*, 2018). Studies of ZnO-based UV detectors have attributed its photoconductive behavior to the desorption and absorption of O_2 on the surface of ZnO, creating surface band bending with reduced depletion width, which allows photogenerated carriers to be separated by an electric field (Liang *et al.*, 2001). Detector noise characteristics, including noise-equivalent power (NEP) and detectivity (D^*) (Sze and Ng, 2006; Yu *et al.*, 2012a; Azhar *et al.*, 2018), were also evaluated in order to distinguish the sensitivity of ZnO thin-film devices before any post-metallization plasma treatment or pre-metallization EBL deposition. Along with detector performance metrics, detector noise characteristics, differentiated by surface electrode, are appended with each plot in Fig. 2.3.

$$R_\lambda = \frac{\Delta I}{PA} \tag{2.6}$$

$$G = \left(\frac{\Delta I}{e}\right) / \left(\frac{P}{h\nu}\right) \tag{2.7}$$

Noteworthy deviations in performance and noise metrics were exhibited with Al electrodes, in which three orders of magnitude reduction in G (1.05×10^{-7}) is found as compared to that of Au (3.52×10^{-4}), Ag (6.57×10^{-4}), and Ti/Ag (3.05×10^{-4}). The same general trend is exhibited with noise parameters, indicating decreased spectral sensitivity in the case of Al. Reports on ohmic behavior for non-alloyed Al have been discussed by Kim et al., namely the formation of an interfacial Al_2O_3 that creates an accumulation of oxygen vacancies behaving as donors, thereby leading to field emission transport (Han-Ki Kim *et al.*, 2003). The heavily doped region, formed by Al penetrating ZnO, diminishes the effect of surface band-bending from oxygen desporption (Feng, 2012), reducing the observed R_λ and G. With high electron concentration in the heavily doped region, along with trap levels present as intrinsic defects in ZnO, a reduction of recombination rate and increased electron accumulation has been described among reports of time-resolved photoresponse measurements of Al:ZnO photodiodes (Amiruddin and Kumar, 2016). This reduction in photoconductivity is accompanied by thermal agitation of charge carriers (Hsu *et al.*, 2004), which is linked to thermal noise, and may explain the significant increase in NEP for Al contacts.

$$NEP = (1/R_\lambda)(2qI_d + 4kT/R_v)^{1/2} \tag{2.8}$$

$$D^* = (Af)^{1/2}/NEP \tag{2.9}$$

The results of the matched pair analysis of Ag and Ti/Ag electrodes is presented in Table 2.2, which tabulates electrode type, oxygen plasma power, number of samples,

95% confidence interval of the barrier height difference (Note: intervals that do not overlap 0 indicates rejection of the null hypothesis), t-statistic and associated p-value.

Electrode	Plasma Power (W)	df	Confidence Interval (eV)	t	p-value
Ag	50	11	[0.037, 0.111]	4.41	1.052×10^{-3}
Ag	250	8	[0.189, 0.214]	37.06	3.083×10^{-10}
Ti/Ag	50	9	[0.093, 0.152]	9.51	5.409×10^{-6}
Ti/Ag	250	11	[0.084, 0.151]	7.69	9.521×10^{-6}

Table 2.2: Matched Pair two-sample t-test analysis of difference in extracted Schottky Barrier Height before and after oxygen plasma treatment

The effect of oxygen plasma post-metallization was explored in the case of Ag and Ti/Ag electrodes, and the treatment quite clearly leads to the formation of Ag_2O and TiO_x/Ag_2O. The barrier heights were extracted before and after treatment and were analyzed as two-sample matched pairs. The null and alternative hypothesis, along with associated probability of a type-I error (p-value) are presented in Fig. 2.4(b) for each combination of Ag and Ti/Ag electrodes, along with plasma treatment power. The results confirm that the barrier energy, in all cases, exhibited a statistically significant increase as a direct result of oxygen plasma treatment. Other studies of Ag_2O contacts on ZnO have also found a significant improvement on barrier heights as a direct result of silver oxidation (Allen *et al.*, 2006), and have attributed this effect to the predicted high work function of the thin O-terminated Ag_2O (001) and (111) surfaces (Gajdoš *et al.*, 2003), while others have modeled Ag_2O as a p-type semiconductor (Li *et al.*, 2003). Since the Ag_2O is already in an oxidized state, it does not introduce additional oxygen vacancies to the ZnO surface. The effect of induced oxidation leading to increased Schottky barrier height has been observed with other noble metals on ZnO (Allen *et al.*, 2009). Along with its high formation energy, with higher plasma power, the formation of TiO_x from Ti is amplified, once again mitigat-

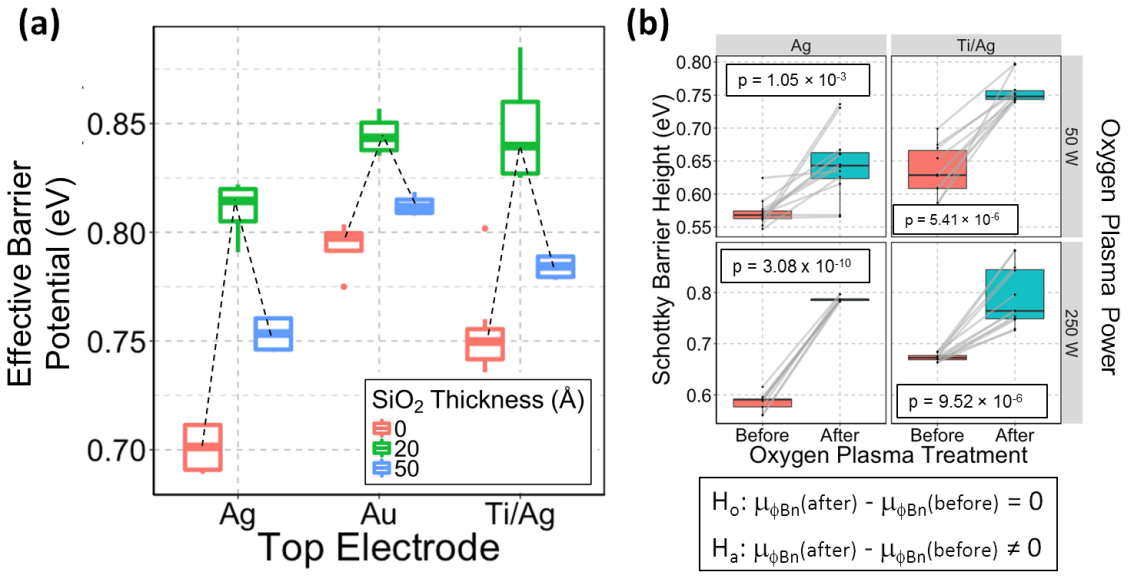

Figure 2.4: (a) Effective Barrier potential variation as a function of EBL thickness and electrode metal. (b) Schottky Barrier height variation due to O_2 plasma treatment with connecting line matching individual devices before and after treatment (Bottom: null and alternative hypothesis of matched pair two sample t-test; associated p-values within inset of each experimental group).

ing the electronic transport modification of a separate (e.g.,TiO_x/Ag_2O) interface and dissimilar barrier with ZnO. This effect explains the larger barrier heights extracted for all Ti/Ag (TiO_x/Ag_2O) cases, as compared to the Ag (Ag_2O) case alone.

Electrical characterization of devices at varying levels of SiO_2 thickness (0 Å, 20 Å, and 50 Å) for each metal electrode was conducted, and the extracted barrier heights are summarized in Fig. 2.4(a). (Note: Transport modeled for thermionic emission in MIS devices entails a current density (J) dependence on $\exp(V^{1/2})$, rather than $\exp(V)$ (Sze and Ng, 2006), and was accounted for accordingly in barrier potential extraction). The effective barrier potential was found to vary in correspondence to the thickness of the EBL, and was maximized for a thickness of 20 Å. The SiO_2/ZnO interface has been investigated by Mohammadnejad et al. who have proposed that thermal electron emission is suppressed with the inclusion of the insulator layer, and that Fowler-Nordheim tunneling dominates with thermionic field emission occurring

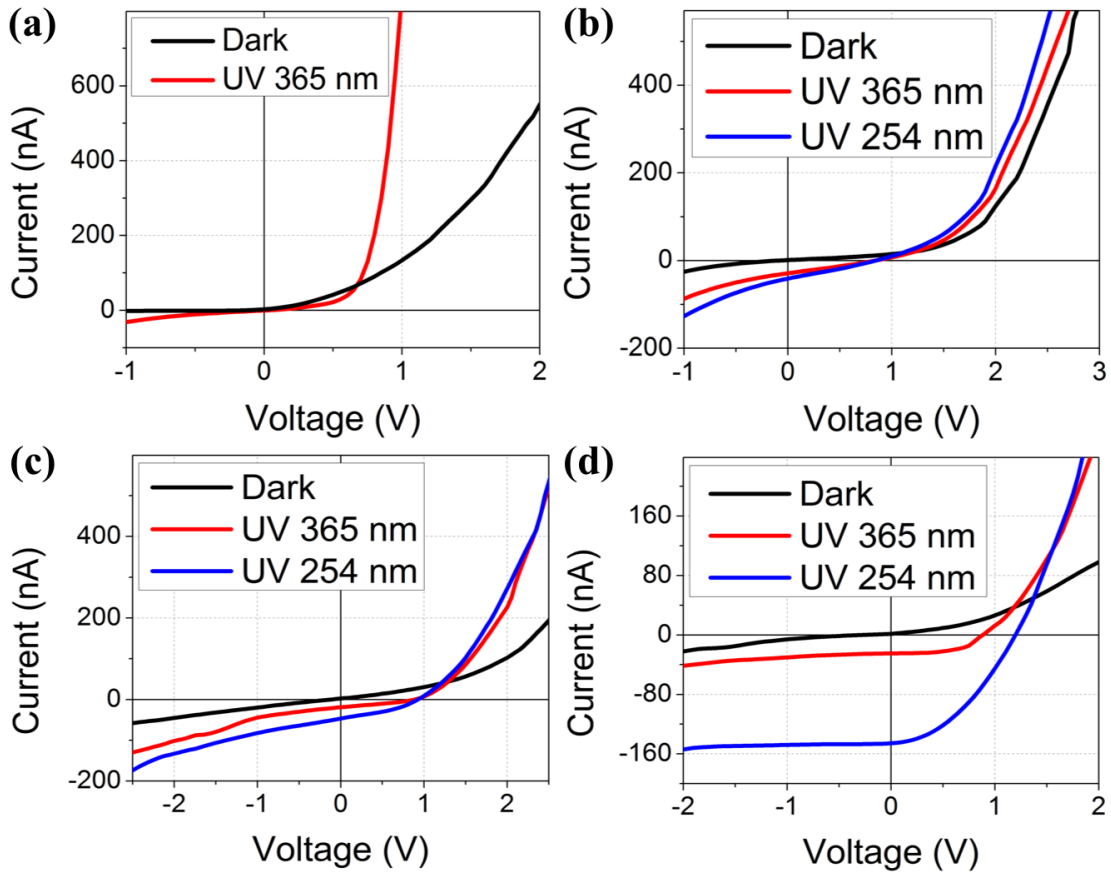

Figure 2.5: Current Voltage response in dark, UV (365 nm) and UV (254 nm) illumination (black, red, and blue traces, respectively) for (a) Au, (b) Ag_2O, (c) TiO_x/Ag_2O, and (d) TiO_x/Ag_2O electrodes patterned as interdigitated grids.

for a greater barrier height than the MS case (Mohammadnejad *et al.*, 2008). In conjunction with oxygen plasma used to induce silver oxidation, this treatment may further passivate ZnO and SiO_2 surfaces (Allen and Durbin, 2008), and reduce incidences of electron hopping and recombination through trap states within the SiO_2/ZnO interface (Allen *et al.*, 2007). For insulator thicknesses greater than 20 Å, the barrier width increases leading to heavily suppressed (leakage) current and reduced barrier potentials (Brillson and Lu, 2011; Yang *et al.*, 2016a).

The I-V responses of devices, incorporating a 20 Å SiO_2 EBL and post-metallization oxygen plasma treatment, under UV illumination are shown in Fig. 2.5. Although

Contact Metal	Contact Geometry	Illumination Wavelength (nm)	Voc (V)	Jsc (mA/cm^2)	Fill Factor	Power Conversion Efficiency
Ag_2O	circle	365	0.85	9.49×10^{-4}	0.2705	2.55×10^{-3}
Ag_2O	circle	254	0.9	2.33×10^{-3}	0.2709	7.72×10^{-3}
TiO_2/Ag_2O	circle	365	0.85	0.144285	0.2983	0.332
TiO_2/Ag_2O	circle	254	0.95	0.205098	0.3486	0.472
TiO_2/Ag_2O	grid	365	0.9	0.124067	0.3901	0.602
TiO_2/Ag_2O	grid	254	1.2	0.729128	0.5394	0.341

Table 2.3: Comparison of solar cell performance for Schottky contact metal, device configuration, and illumination conditions.

characteristic photovoltaic response curves are observed for devices with TiO_x/Ag_2O contacts, devices with Al (not shown) and Au do not exhibit such behavior. The power conversion efficiencies were extracted using (2.7), where P_{light} is the power of the illumination source and FF is the fill factor (defined as a ratio of the maximum power point to the product of short circuit current, I_{sc}, and open circuit voltage, V_{oc}). The use of a large area interdigitated grid design that minimizes shading while maintaining conduction was also explored in this work and resulted in greater power conversion efficiency, as shown in Fig. 2.5(d). These results, arranged by device contact geometry and illumination configurations, are summarized in Table 2.3. Power losses from the illuminated electrode are proportional to the cube of line spacing, however, narrower line widths with thicker metal can reduce resistive losses, while allowing for shorter spacing (Serreze, 1978). These design rules were considered in formulating a suitable electrode pattern for optimizing photovoltaic performance and further explain why grid patterns resulted in greater power conversion than a com-

pletely opaque electrode pattern.

In general, weak photovoltaic conversion utilizing ZnO absorbers under ultraviolet illumination has been reported previously (Nakano *et al.*, 2008; Amiruddin and Kumar, 2016). Additionally, studies on (a) photovoltage on ZnO surface using time-resolved Kelvin probes (Li *et al.*, 2009) and (b) majority carrier-based, Schottky solar cells with high E_g absorber (Yang *et al.*, 2016a) have alluded to the inherent relationship of work function to typical photovoltaic conversion mechanisms (Kasap, 2017). However, as observed throughout Fig. 2.3, the lack of photovoltaic conversion for MS diodes suggest the presence of recombination centers at the metal-semiconductor interface. Moreover, in contrast to a pn diode that is a minority carrier controlled device, the saturation current (I_0) in an MS diode, a majority carrier device, becomes a major limitation for the improvement of solar cell performance. Therefore, the integration of a sufficiently thin insulating layer on ZnO effectively passivates the interface (Fonash, 2010) and reduces (I_0), while allowing minority carriers to tunnel through the insulator. In forward bias, the field drives minority carriers toward the interfacial barrier prior to tunneling, while majority carriers are driven away from the interface. When considering the post-metallization oxidation of $Ag/SiO_2/ZnO$ (MIS) devices, the formation of p-Ag_2O surface electrodes transforms device configurations into p-i-n heterojunctions, which more precisely models measured I-V photoresponse. The transport mechanism for such heterojunction devices is illustrated in Fig. 2.1(d) in the case of Ag_2O in contact with a thin EBL on ZnO. The sufficiently thin EBL results in increased effective barrier potential, as noted in Fig 2.4(a), and reinforces the relationship between the effective barrier potential and V_{oc}. The integration of an additional layer of TiO_x further reduces the recombination rates and improves the solar cell characteristics, as illustrated in Fig. 2.5(c,d). Indeed as previously reported for Si MIS-based cells, an interfacial layer up to approximately 20 Å in thickness re-

duces dark current (due to suppressed majority electrons) while minimally affecting the short circuit current (due to tunneled minority holes), and locally maximizing V_{oc} (Card, 1977). Considering the relatively large D_{it} estimated for ZnO thin film in this study (Table 2.1), as well as the small grain size observed in Fig. 2.2(a), the effectiveness of EBL in reducing the trap states is noteworthy. The thin-film integration of additional oxide layers and interfaces coupled with the EBL on ZnO introduces confounding complexities and difficulties in interpretations; for example, under dark and illuminated conditions, recombination (and generation rates under light) is field and spatially dependent, but unknown for these systems. All I-V photoresponse presented throughout Fig. 2.5 clearly indicate that photocurrent is voltage and oxide layer-dependent, and therefore, the principle of superposition is not applicable. Although this preliminary work qualitatively describes the experimental data, a more robust analysis (similar to that presented in (Card, 1977)) must be undertaken. Specifically, numerical and/or analytical models of the multi-layered oxides coupled with relevant parameters (e.g., energy levels of interface states and defects, spatially-dependent recombination and generation rates, oxide-dependent carrier lifetimes etc.) must be developed to compare against experimental and simulated UV photovoltaic current-voltage responses.

2.5 Conclusion

This preliminary study reports the photovoltaic response of sputtered ZnO (2% Mn) films integrated with metal or semiconductor contacts, and/or majority carrier blocking layers (i.e., in MS, MIS, and p-i-n heterojunction configurations) for visibly transparent, low-power applications such as window-integrated photovoltaics and electrochromic devices. For MS Schottky devices, a high interface state trap density ($D_{it} \approx 8.0\times10^{11}$ $eV^{-1}cm^{-2}$), estimated by fitting the dark current-voltage response

to the generalized Bardeen Model, warranted ZnO surface passivation. Nonetheless, the photodetection performance and noise response of MS devices were assessed with respect to the nature of contacts, i.e., Schottky (Au, Ag, and Ti/Ag) versus ohmic (Al). Under UV-A illumination, the Ag-ZnO detectors exhibited the highest performance, with responsivity (R) and photoconductive gain (G) of 1.93×10^{-4} A/W and 6.57×10^{-4}, respectively. Post-metallization oxygen plasma treatment of Ag or Ag/Ti electrodes, coupled with inferential matched pair analysis, indicated significant increases in effective Schottky barrier heights, as well as the formation of semiconducting Ag_2O and TiO_x/Ag_2O at the interfaces. For such devices with patterned interdigitated electrodes, the photovoltaic response of $Ag_2O/TiO_x/SiO_2/ZnO$ layers (modeled as a p-i-n heterojunction) under UV-C illumination indicated a short circuit current density (J_{sc}) and a relatively high open circuit voltage (V_{oc}) of 0.68 mA/cm^2 and 1.2 V, respectively. These results are attributed to the presence of additional quasi-neutral and space charge regions for optical generation of charge carriers, and the promotion of minority carrier tunneling and surface passivation by the optimally determined 2 nm SiO_2 blocking layer. Much work remains to quantitatively account for the (a) voltage-dependent and site-dependant recombination losses, (b) carrier recombination at contacts, (c) photocurrent sign change, and (d) spatial dependence of the generation and recombination across the multilayered structures in order to model the photovoltaic I-V response (with accurate transport parameters) under high-energy UV illumination. However, this initial study indicates the potential of all-inorganic, visibly transparent, current-matched and voltage-matched ZnO-based UV absorbers for low-power, smart window-integrated photovoltaic devices.

Chapter 3

SELF-POWERED, INKJET PRINTED ELECTROCHROMIC FILMS ON FLEXIBLE AND STRETCHABLE SUBSTRATES

3.1 Abstract

Electrochromic films have been used as a non-emissive material for display applications. Such materials have already been integrated in antiglare rearview mirrors for passenger vehicles as well as smart windows intended for energy savings for buildings. However, most electrochromic materials are deposited on rigid substrates, which prevent its use in flexible and stretchable electronic applications, where low temperature deposition techniques are desired. Additionally, electrochormics require an external power source to drive the underlying reduction/oxidation reaction. In this work, electrochromic materials inkjet-printed onto flexible and stretchable substrates have been explored. These devices are "self-powered" by organic solar cells also fabricated on flexible and stretchable substrate such as PDMS and PET. A set of inks based on a combination of synthesized and commercially obtained WO_3 nanoparticles, W-TiO_2 and TiO_2 nanoparticles were evaluated. The microstructure of the nanoparticles used in this study were examined under scanning electron microscopy for examining nanoparticle morphology, x-ray diffraction for chemical and structural characterization, and dynamic light scattering for particle size determination. Electrochromic layers were then ink-jet printed on flexible and stretchable PDMS substrates, using synthesized Ag nanowires as conductive, yet highly transparent electrodes. The stretchable printed electrochromic devices under various stress conditions and electrochromic performances were evaluated and demonstrated clear switching behavior under exter-

nal bias, with 7 second coloration time, 8 second bleaching time, and 0.36-0.75 optical modulation at λ=525 nm. Cyclic voltammetry and galvanostatic charge/discharge measurements demonstrated high areal capacitance, with limited stability upon cycled operation. The electrochromic devices were then integrated in an Internet of Things (IoT)-enabled switching configuration, self-powered by PCDTBT:$PC_{70}BM$ organic photovoltaics. The bulk heterojunction devices were evaluated with varying hole-transport layers and substrates, and exhibited the strongest performance of PCE$\approx$ 3%, V_{oc}=0.9V and J_{sc} $\approx$ 10-15 mA/cm^2. The described self-powered, IoT-enabled, ink-jet printed electrochromic devices, fabricated on flexible substrates, are demonstrative of potential applications for wearable electronics.

3.2 Introduction

In recent years smart window technologies have become among the most rapidly developing fields, both in commercial and in academic realms. In conjunction with attention devoted to harvesting energy through solar radiation, researchers have recognized that solar radiation also represents the cause of major energy consumption through cooling loads of residential and commercial buildings (US Department of Energy, 2018). Traditional electrochromic devices have become increasingly popular as a method to solving this problem, but suffer the limitation of requiring external power. Several researchers have integrated electrochromics with photovoltaics forming "self-powered," or photo-electrochromic devices. These realizations have varied from printed devices, to vertically integrated devices, and even devices that harness an internal redox potential (Cannavale *et al.*, 2016). However, these studies have focused their efforts on rigid or flexible substrates, but not necessarily stretchable substrates. This distinction is heavily important for wearable implementations of such technologies as they must contour to irregular nature of the human body, but

fundamentally represent many processing challenges.

Electrochromic devices have been realized with a variety of material systems including organic semiconducting polymers such as PEDOT:PSS and metal oxides, of which, WO_3 has dominated (Taylor *et al.*, 1996). Typical methods of deposition of WO_3 have included electrodeposition (Deepa *et al.*, 2004) and sol-gel techniques. Sol-gel techniques in particular require rather large and slowly ramped sintering temperatures to achieve crystalization of the WO_3 sols, and these processing temperatures are fundamentally incompatible with substrates that are otherwise sensitive to heat (Deepa *et al.*, 2006b), including PET and PDMS. Relatively few groups have explored inkjet printing electrochromicly active oxide-based nanoparticles (Costa *et al.*, 2012b; Layani *et al.*, 2014; Santos *et al.*, 2015). This is important for substrate-independent patterning of functional electrochromics, and can later be extended into roll-to-roll mass-manufacturing. Wojcik et al. systematically demonstrated the trade-offs between speed in electrochromic switching kinetics from the from the highly active crystal surfaces, and the intensity of optical modulation brought upon by the amorphous phase materials (Wojcik *et al.*, 2012). Deepa et al. have shown that this is due to the fact that highly ordered crystal phases become more dense, and therefore inhibit Li^+ ion intercolation into the WO_3 sites, thereby reducing colaration (Deepa *et al.*, 2006c). Wojcik was also able to demonstrate that the inclusion of TiO_2 nanoparticles, which are also electrochromic in nature, is a cathodic material, and were able to reduce the switching potential considerably. In a later analysis of their mixture experimental design, Wojcik et al. demonstrate that the inclusion of an amorphous matrix in tandem with the highly crystal nanoparticles can balance the tradeoffs of coloration and bleaching time, operating voltage, and optical density, such that an optimal ink can be achieved (Wojcik *et al.*, 2014).

In conjunction with low-temperature developments for processing oxide nanoparticle-

based functional devices, the progress of organic photovoltaics, (along with other organic-based electronic and optoelectronic devices) have steepened considerably. In particular, active layers composed of poly[N-9'-heptadecanyl-2,7-carbazole-alt-5,5-(4',7'-di-2-thienyl-2',1',3'-benzothiadiazole)]:phenyl-C71-butyric-acid-methyl (PCDTBT:$PC_{70}BM$) have quickly emerged as a high performance OPV devices as they have continually demonstrated high open circuit voltage and reported power conversion efficiencies of as high as 7.2% (Sun *et al.*, 2011), incorporating MoO_x as the hole injection material. Devices composed of this this bulk heterojunction have also been reported as particularly air-stable (Jung *et al.*, 2014; Zhang *et al.*, 2016) and have frequently been processed on flexible substrates using inkjet-printed techniques. One of the major differences that sets apart PCDTBT from regioregular bulk heterojunction polymers is the elimination of the post-deposition anneal, in which it has been shown by other researchers (Staniec *et al.*, 2011) to not affect optical properties such as extinction coefficient, and degrade device performance, due to the introduction of midgap monomolecular recombination centers (Constantinou *et al.*, 2015). The result is the retention of a highly amorphous and thus flexible properties, which has catalyzed its discussion in large scale plastic processing (Beaupré and Leclerc, 2013). The aforementioned studies have largely focused on incorporating PCDTBT:$PC_{70}BM$ onto PET, with ITO as the transparent conductor. However, ITO takes on a variety of disadvantages including the scarcity of indium, leading to higher demand. More importantly, ITO is highly brittle which limits its performance under strain. Thus many researchers have elected to explore AgNWs embedded in PDMS as a substrate for realizing stretchable electrochromics, due to percolating nanowire networks that have shown excellent resilience to strain (Yan *et al.*, 2014). Others have explored the use of embedded AgNW networks in PDMS as substrates for organic photovoltaic devices (Herrera Rocher, 2015) and some have even explored embedded

AgNPs in active layers with improved device performance (Wang *et al.*, 2015; Parlak *et al.*, 2013).

In this study the two technologies have been intersected to realize a fully functional solar-powered electrochromic device on a stretchable substrate, incorporating dual-phased WO_3 nanoparticles for the electrochromic device and powered by a PCDTBT:$PC_{70}BM$ organic solar cell. These devices are linked to an Internet of Things controller, allowing users to control electrochromic switching remotely. As shown in Figure 3.1(a), the organic photovoltaic device powers a modified Broadcom BCM43362 WiFi controller, driven by an ST Microelectronics STM32f205RGY6 ARM Cortex-M3 MCU (packaged by Particle Inc.). The internal microcontroler drives a pulse-width modulated output that allows tuning of output potential. When the user remotely varies intensity from a slider interface (provided as a mobile app by Particle) the load device, the stretchable electrochromic device is activated and transitions accordingly.

3.3 Experimental Details

3.3.1 AgNW Synthesis and PDMS Substrate Embedding

AgNWs grown by a solvothermal technique (Moreno *et al.*, 2012) in which 0.1 mM of NaCl and 0.15 M of polyvinylpyrrolidone (PVP) were dissolved in 10 mL of ethylene glycol. This salt solution was then placed in a buret and injected dropwise into a 0.1M solution of $AgNO_3$, also dissolved in 10 mL of ethylene glycol. The light-yellow solution was stirred vigorously and half of this mixture was transferred into a 25 mL teflon lined autoclave, and heated at 160 °C for 2.5 hours. The chamber was allowed to cool to room temperature and its contents were thoroughly washed by successive repetitions of dispersing in acetone and centrifugation to separate the solid

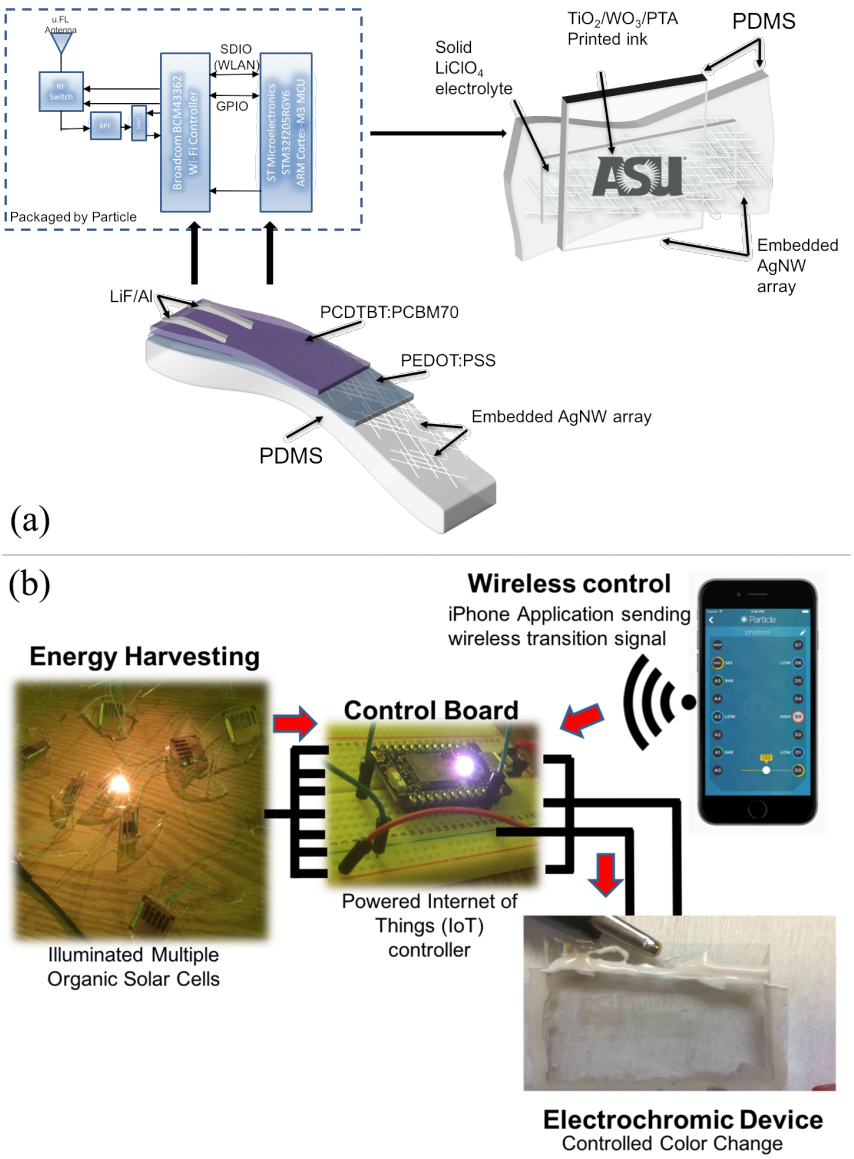

Figure 3.1: (a) Material and system view and (b) Device realization of Self-powered IoT-enabled Electrochromic Stack

content. The nanowires were dispersed on a Si substrate and characterized under field-emission scanning electron microscopy.

To embed the nanowires in PDMS, a PC filter paper was placed over a vacuum buchner filter, AgNWs in isopropanol dispersion were dispersed over the paper, and the isopropanol was allowed to evaporate naturally. The PDMS (Sylgard 184) was prepared by mixing a base and curer (weight ratio 10:1) over the filter paper in a

petri dish. After curing at 80 °C for 2 hours, the filter paper was removed and the AgNWs remained embedded in the PDMS matrix.

3.3.2 OPV Device Fabrication

Both ITO coated PET foils and AgNW/PDMS membrane were ozonated for 10 minutes. The samples were brought into an environmentally controlled glove box and PEDOT:PSS (non-conductive) was spun coated at 5000 RPM for 60 seconds. PCDTBT:$PC_{70}BM$ (1:4) was dissolved overnight at 80 °C spun coated at 700 RPM for 60 seconds. The samples were placed into an evaporator chamber and LiF (7 Å)/Al (70 nm) cathode patterns (1 cm × 1 cm) were evaporated through a shadow mask. The samples were then electrically characterized using a Kiethly electrometer under dark and AM 1.5G conditions.

3.3.3 PTA/WO_3 NP synthesis

Acetetylated Peroxotungstic Acid

Peroxotungstic Acid (PTA) was formed by dissolving 13 g of W powder with 80 mL H_2O_2 and 8 mL DI water in ice bath (due to the reactive exothermic reaction). The solid yellow material was filtered with a standard 0.2 μm filter paper and then dissolved in 80 mL acetic acid. This solution was then refluxed for 48 hours at 60 °C and was removed and vacuum dried. A solid, light-yellow flaky product, Acetetylated Peroxotungstic Acid was extracted.

WO_3 Nanoparticles

The PTA solid was dissolved in 0.3M HCl and placed in a hydrothermal autoclave for 2.5 hours. The chamber was allowed to cool to room temperature, its contents removed and washed in DI water, and separated using centrifugation.

Ink formation

A set of four inks based on the combination of synthesized WO_3 nanoparticles, commercial WO_3 nanoparticles, commercially obtained W-TiO_2 and TiO_2 nanoparticles, PTA, and oxylic acid dihydride (OAD) were mixed in isopropanol. The relative weights of each mixture were based on a previously reported D-optimal ink formulation. The ink was diluted 1/10 after initial mixture, and patterns were printed 33 times using a Microfab Jetlab II printer.

Electrochemical Characterization

An Autolab Potentiostat/Galvanostat was used to perform Cyclic voltammetry measurements at the specified voltages. A four-channel Arbin system was used to perform Galvanostatic charge–discharge measurements.

3.4 Results and Discussion

In Figure 3.2, the absorption spectra of PCDTBT and PCDTBT:$PC_{70}BM$ (1:4 weight ratio) are shown, overlayed with the terrestrial AM 1.5G solar spectrum. Upon complete dissolution of PCDTBT with $PC_{70}BM$, it is observed that the PCDTBT peak at 580 nm reduces, and the composite polymer forms a new peak at 480 nm, as well as exhibiting a broadened absorption spectra across visible range–also observed by others (Ochiai *et al.*, 2012; Zhao *et al.*, 2014). The attenuation of the natural PCDTBT absorption peak, and its change in pigment indicates a mixed bulk-heterojunction state of polymer and has been linked to the dimerization of $PC_{70}BM$ (Distler *et al.*, 2014).

Figure 3.3 shows the current-voltage (I-V) characteristics of the studied organic photovoltaic devices illuminated under AM 1.5G spectral irradiance with varying substrates, choice of hole transport layer, and a comparison to P3HT absorber (where

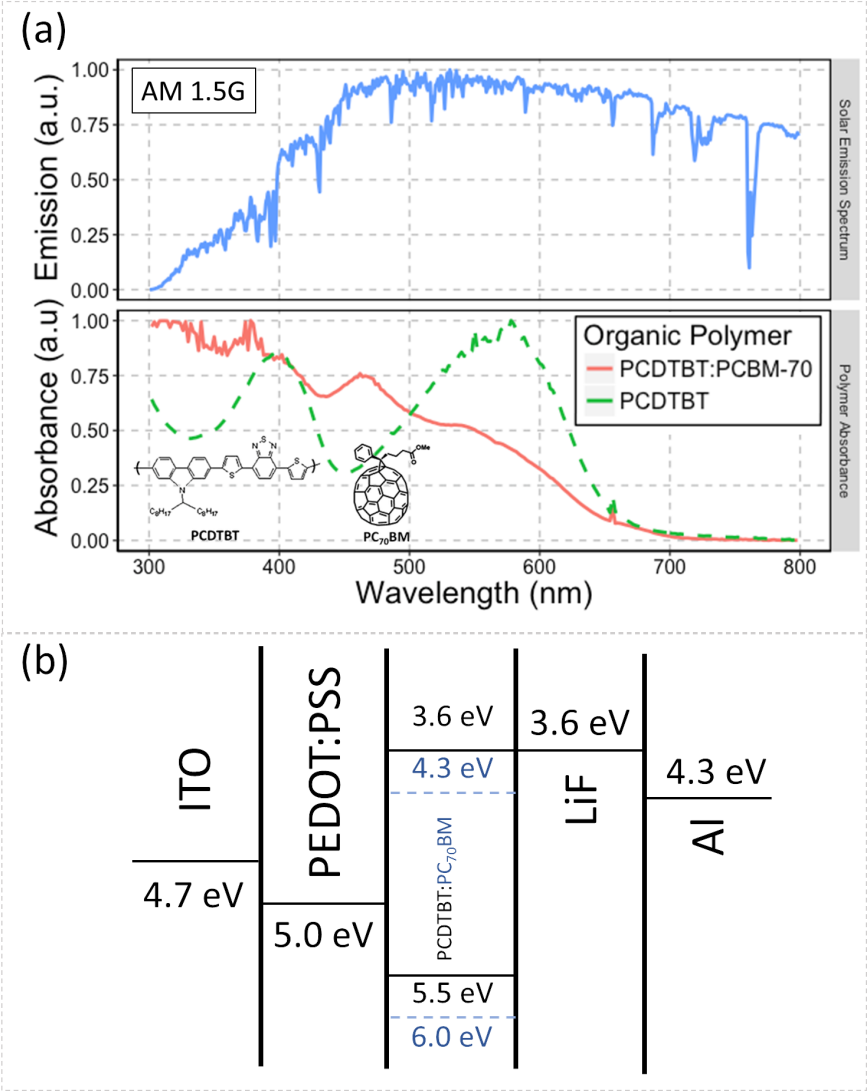

Figure 3.2: (a) UV/Vis Spectra of organic polymers (bottom) with overlayed AM 1.5G Solar Spectral irradiance (top). (b) Energy level diagram of studied bulk heterojunction device.

device 1 in this report refers to PCDTBT:PC_{70}BM with non-conductive PEDOT:PSS hole transport layer, device 2 refers to PCDTBT:PC_{70}BM with conductive PEDOT:PSS hole transport layer, device 3 refers to PCDTBT:PC_{70}BM with non-conductive PEDOT:PSS hole transport layer on silver nanowires, and device 4 refers to P3HT:PC_{60}BM with non-conductive PEDOT:PSS hole transport layer). Figure 3.3(a-c) features single representative devices composed of PCDTBT:PC_{70}BM, and it is found that the

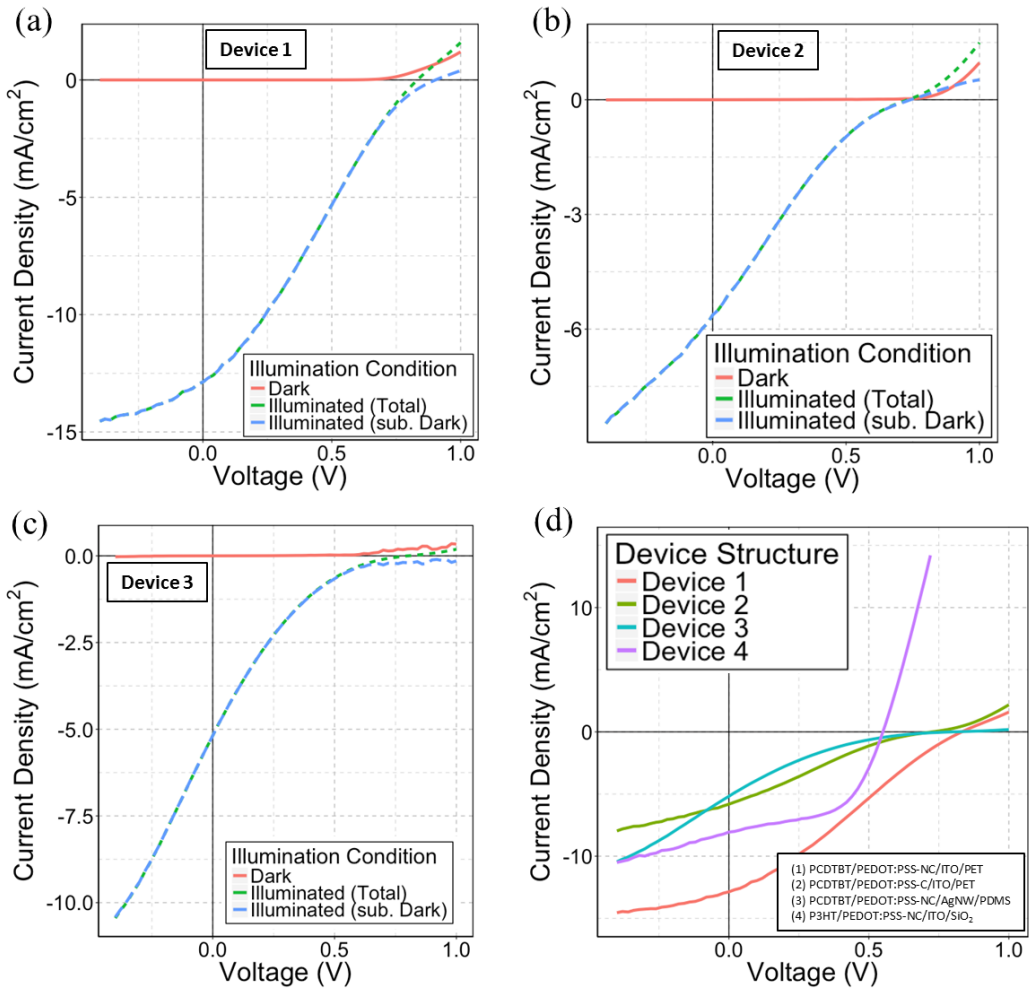

Figure 3.3: Dark (red trace) and total illuminated (dashed green trace) Current-Voltage characteristics, with their subtractive difference (dashed blue trace) segmented with the device structures (a) Device 1: PCDTBT: $PC_{70}BM$/PEDOT: PSS-NC/ITO/PET, (b) Device 2: PCDTBT: $PC_{70}BM$/ PEDOT: PSS-C/ITO/PET, (c) Device 3: PCDTBT: $PC_{70}BM$/PEDOT: PSS-NC/AgNW/PDMS. (d) Total illuminated current-voltage characteristics for all studied devices (inset: device structure numbering).

dark current exhibits typical rectifying behavior, while the illuminated current exhibits an S-shaped response (which will be discussed in the next paragraph). Initially it can be see that the subtracted illuminated current does not converge on a single value, suggesting superposition does not apply to this device structure. When comparing all illuminated current response, illustrated in Figure 3.3(d), the device

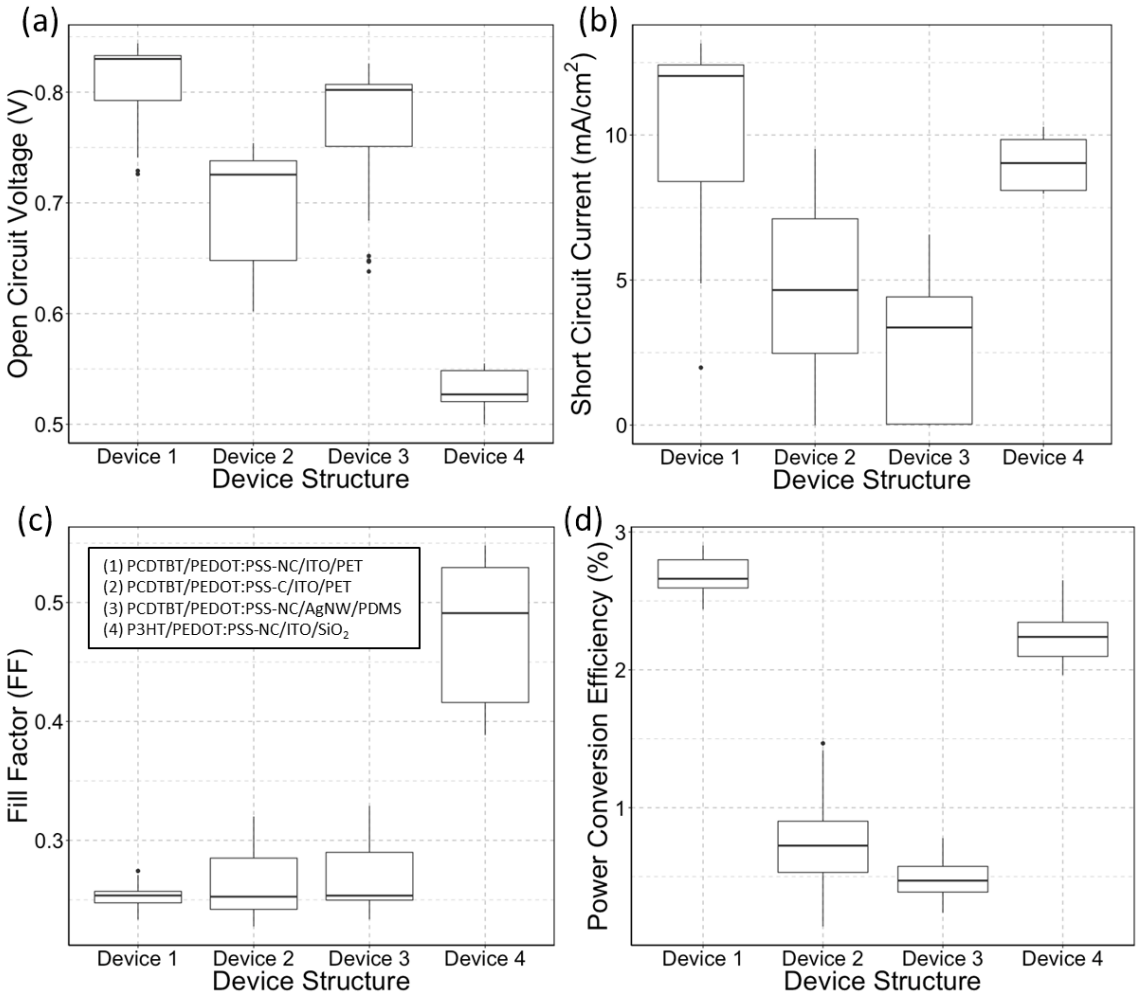

Figure 3.4: (a) Open-Circuit voltage, (b) Short-Circuit current, (c) Fill Factor, and (d) power conversion efficiency of all studied devices (inset: device structure numbering).

configuration that performs best incorporates non-conductive PEDOT:PSS as the hole transport layer (HTL) on ITO/PET (device 1). Device 1, as shown throughout Fig 3.4, outperformed all other device structures, and was therefore selected for self-powered window application.

Typically, non-conductive PEDOT:PSS is favored as to suppress lateral conduction of separated charges that never reach the cathode. In the case of ITO in device 2, the conduction is comparable to that of conductive PEDOT:PSS, and there-

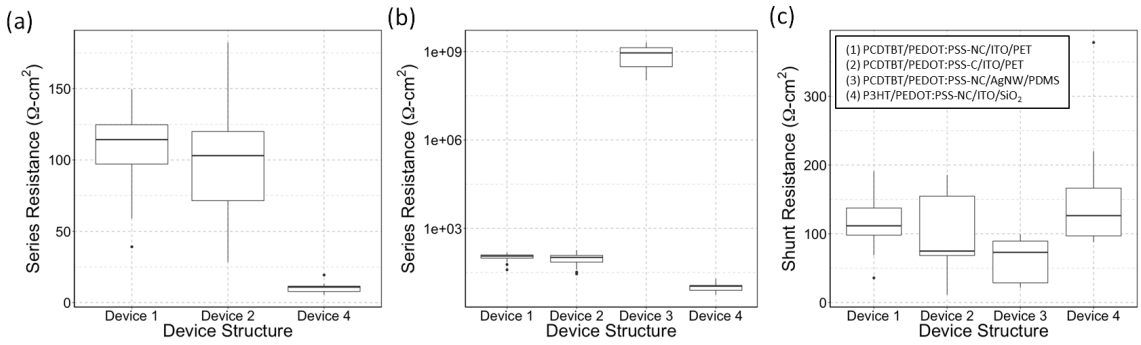

Figure 3.5: (a) Series Resistance (linear scale), (b) Series Resistance (log scale), and (c) Shunt Resistance (linear scale) of all studied devices (inset: device structure numbering).

fore, forms a current divider that reduces overall performance. Regardless of PEDOT:PSS conductivity the formation of S-shaped characteristics emerge in all cases of PCDTBT:$PC_{70}BM$ devices. This phenomenon has been linked to the formation of a hole injection (electron extraction) barrier from HTL (Cheng *et al.*, 2015), active layer degredation extended radially from the center of the device, indicating an imhomogeniety of device thicknesses due to the spin coating process and surface dipole formation from ambient conditions, Substrate conductivity, charge accumulation at the interfaces between the active layer and the electrodes (R. Mateker *et al.*, 2013), or oxidized species in a BHJ active layer acting as a carrier trapping site (Wang *et al.*, 2012), all of which have the ultimate effect of increasing series resistance (R_s). A summary of extracted series resistances, subdivided by device structure, is presented in the box plot in Fig. 3.5(a-b). As seen in Fig. 3.5(a), the series resistance of devices composed of PCDTBT:$PC_{70}BM$ on ITO(120 $\Omega/\square$)/PET is almost four times that of P3HT:$PC_{60}BM$ on ITO(40 $\Omega/\square$)/SiO_2. For AgNW devices (which will be discussed in the next paragraph), illustrated in the log plot in Fig. 3.5(b), the series resistance is almost 7 orders of magnitude larger than the next comparable device. Based on the available conductivity data of choice of ITO coated PET substrates, the high surface resistivity may contribute to the observed high-R_s S-shaped traced from illuminated

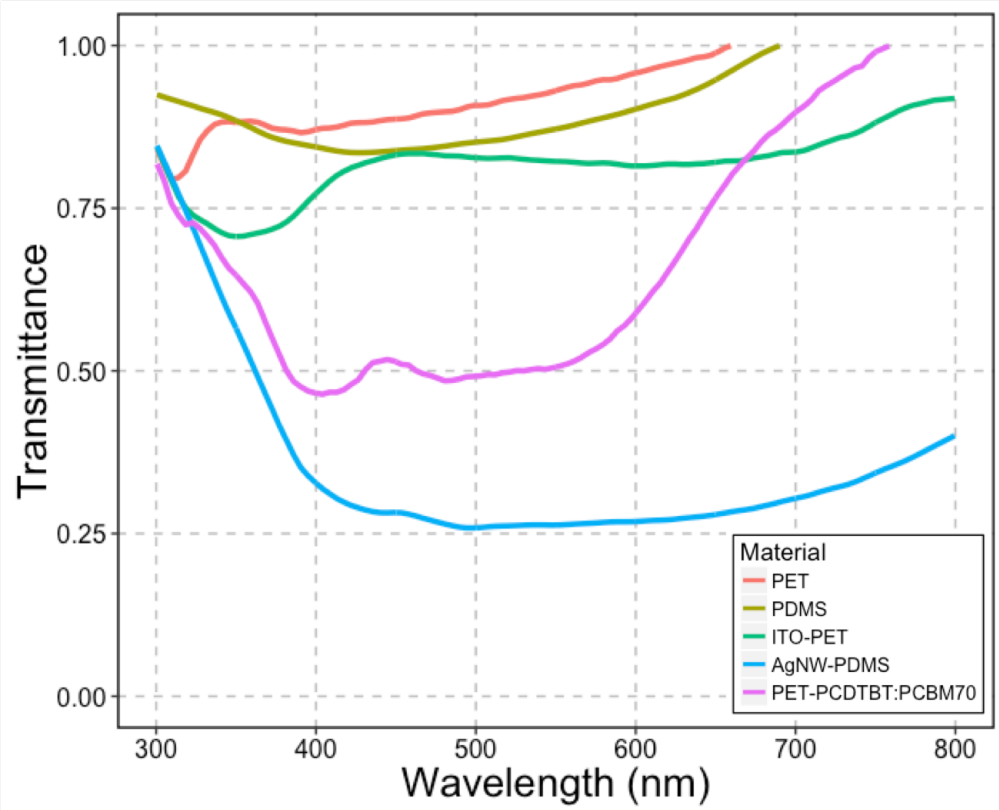

Figure 3.6: Transmittance of various polymer stacks

response. The shunt resistance among all devices, as illustrated in Fig. 3.5(c), is quite sufficiently, and comparably high.

From Fig. 3.4(a), both device 1 and device 3 use non-conductive PEDOT:PSS, and it is observed that their V_{oc} remain in the range of 0.7-0.9 V. However, despite performing the best, devices of device 1 configuration consistently demonstrate poor FF, shown in Fig. 3.4(c). From the above-discussed S-shaped response, a significant voltage dependence on photocurrent, either due to mechanisms of field dependent charge generation efficiency or collection efficiency (Etzold *et al.*, 2011) is uncovered. As can be seen, both device 1 and device 2 do not exhibit ideal diodic characteristics when illuminated, but do under dark conditions. Other reports have observed a drop in FF due to increased thicknesses of layer (Moon *et al.*, 2012), and relative weight ratio of PCDTBT to $PC_{70}BM$ (Ochiai *et al.*, 2012; Zhao *et al.*, 2014), however in those

cases, the rectification was retained. This could be due to the relative resistance of ITO on PET which contributes to these loss mechanisms. Device 3 formed of AgNWs networks on PDMS had the poorest performance, despite exhibiting a large V_{oc}. From the plot of transmittance in Figure 3.6, we observe that AgNW networks tend to absorb the most light in the visible spectrum, thereby shading the active layers that are deposited on the side opposite to illumination. Among the noted features of degraded device performance in this study was the series resistance of AgNW devices, which was was found to be 7 orders of magnitude larger than all other cases. This could be related to the presence of spatially inhomogenous electrically inactive areas that arise due to inconsistent dispersion of AgNWs.

Material	Mean Diameter (nm)	Standard Deviation (nm)
W-TiO_2	451	17.25
TiO_2	82.3	23.5
WO_3 (synthesized)	582.5	32.82
WO_3 (commercial)	325.8	2.98
PTA	464.9	49.7

Table 3.1: Comparison of constituent nanoparticle sizes in electrochromic inks

The micrstructure of the nanoparticles (shown in Figure 3.7(a)) used in this study were examined under scanning electron microscopy Figure 3.7(b), and their respective distribution of sizes using dynamic light scattering are summarized in Table 3.1. It can be seen that W-loaded TiO_2 nanoparticles are considerably larger than that of intrinsic TiO_2 (approximately 5.5× larger), and synthesized WO_3 nanoparticles were 1.8× larger than commercial ones. This could be related to the allowed growth time of synthesized nanoparticles. As a general rule of thumb the ratio nozzle size to particle size is approximately 9:1 in order to reduce the incidence of clogging and

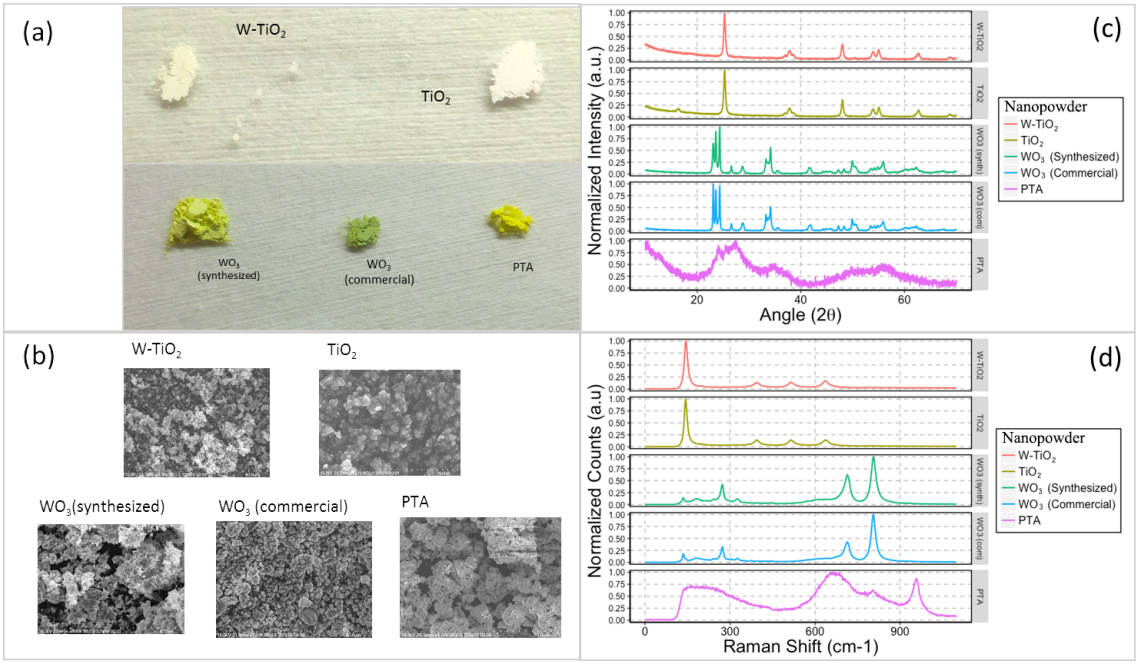

Figure 3.7: (a) Photograph (b) SEM Micrographs (c) XRD, and (d) Raman Spectrograph of nanopowders

agglomeration (Wojcik *et al.*, 2012). The nozzle used in this study was a MicroFab MJ-AT-01-50, low temperature printing device with an orifice diameter of 50 μm.

Figure 3.7(c) shows the XRD pattern of all constituent nanoparticles used in this study, including W-loaded TiO_2, undoped TiO_2, synthesized WO_3, commercial WO_3, and PTA. It is found that the relative difference between both cases of TiO_2 studied were relatively negligible, and closely correspond to the anatase phase of titanium oxide (JCPDS 21-1272). Additionally, the synthesized and commericial WO_3 nanoparticles closely correspond to the monoclinic phase (JCPDS 20-1324). The pure anatase nanoparticles exhibit a peak at 16.3 which does not match the JCPDS reference card. The presence of this peak may be due to 1) Lack of thermal treatment, 2) water or hydride bonds, or 3) size effects of TiO_2. However, in the W-loaded TiO_2 does not exhibit this peak, which may either be due to the size of the particle or the fact that W is suppressing its excitation. However, due to the fact

that no visible transference of WO_3 related peaks can be found in this diffractogram, it can be inferred that the concentration of W is relatively small and controlled, as compared to previous studies (Hong *et al.*, 2014; Mayoufi *et al.*, 2014). For WO_3, it is found that the intensity of (002) plane in the synthesized case is slightly more intense than commercial case. This could be an indication of tetragonal or orthohombic phase. The diffraction pattern related to PTA matches that of prior studies (Deepa *et al.*, 2006a).

In Figure 3.7(d), the molecular structures of the nanoparticles have been investigated with Raman spectroscopy, and were normalized to the largest peak (143.22 cm^{-1} for TiO_2 cases, 805 cm^{-1} for WO_3 cases, and 660 cm^{-1} for PTA). Once again TiO_2 cases do not show significant differences among one another in regards to peak positions. Peaks at 143.222 cm^{-1} and 637.486 cm^{-1} have been attributed to the 3Eg peak and peaks at 392.713 cm^{-1}, 515.291 cm^{-1} have been attributed to the 2B1g peak. The W-doped TiO_2 nanopowder does not show any evidence of weak peaks attriubted to WO_3 or any vibrational modes related to W-O-W peaks, as addressed by other reports. Synthesized nanopowders do not show evidence of hydrate phase and again correspond to the measured commercial case of monoclinic WO_3. The evolution of peaks from amorphous PTA is shown to transition into crystalline nanopowders. All peaks below 200 cm^{-1} are related to the lattice modes of WO_3. Peaks at 710 cm^{-1} are described as the "stretching-mode" which is shifted from 820 cm^{-1} in the amorphous phase PTA. Broad peak at 636 cm^{-1} for amorphous PTA related to O-W-O bending mode, which has been shifted to 328 and 274 cm^{-1} for nanopowders. And finally, amorphous PTA has peak at 946 cm^{-1} which is consistent with the W=O or W-O terminal bond.

Several images of the stretchable printed electrochromic device under various stress conditions are shown in Figure 3.8. A summary of electrochromic performances are

Ink	τ_{color}	τ_{bleach}	$\Delta OD\|_{\lambda=525nm}$
1	7	10	0.3667
2	15.3	16	0.7554
3	10.5	12	0.6347
4	8	13	0.5874

Table 3.2: Performance metrics of electrochromic inks

shown in Table 3.2. As noted, nanoparticles are used to circumvent high processing temperatures of traditional amorphous sol. Additionally, higher temperatures densify crystal phases which ultimately limit Li^+ ion intercolation into the WO_3 sites. Wojcik showed a major tradeoff between switching time kinetics, caused by highly crystal surfaces, and optical modulation, related to the amorphous phase of WO_3 (Wojcik *et al.*, 2012). As noted, TiO_2 is cathodic and loaded into the system to reduce switching potential. It appears that all measured factors in this case are highly dependant on the type of TiO_2 used in the electrochromic ink. Pure anatase NPs result in extremely fast switching times at the expense of optical modulation, and the exact opposite is true of W-TiO_2. These results suggest that in addition to the existing WO_3 and PTA compositions leading to electrochromic behavior that exist in the ink matrix, the W of TiO_2 also contribute to electrochromic activity because they also represent Li-ion insertion sites. However, due studies investigating W-TiO_2 in photocatalytic activity (Chang and Liu, 2014) have shown that W ions have high coordination numbers and high electronegativity (Pauling scale: 2.36) which bond to O^{2+} radicals. The W^{6+} in WO_3 has a coordination number of 6, whereas they are 4-coordinated in the TiO_2 matrix. This leads to tightly bound O^{2-} thereby impeding interfacial charge transfer. As a result, electrochromic activity within the ink matrix is increased, but will switch over a longer time-scale due to reduced conductivity.

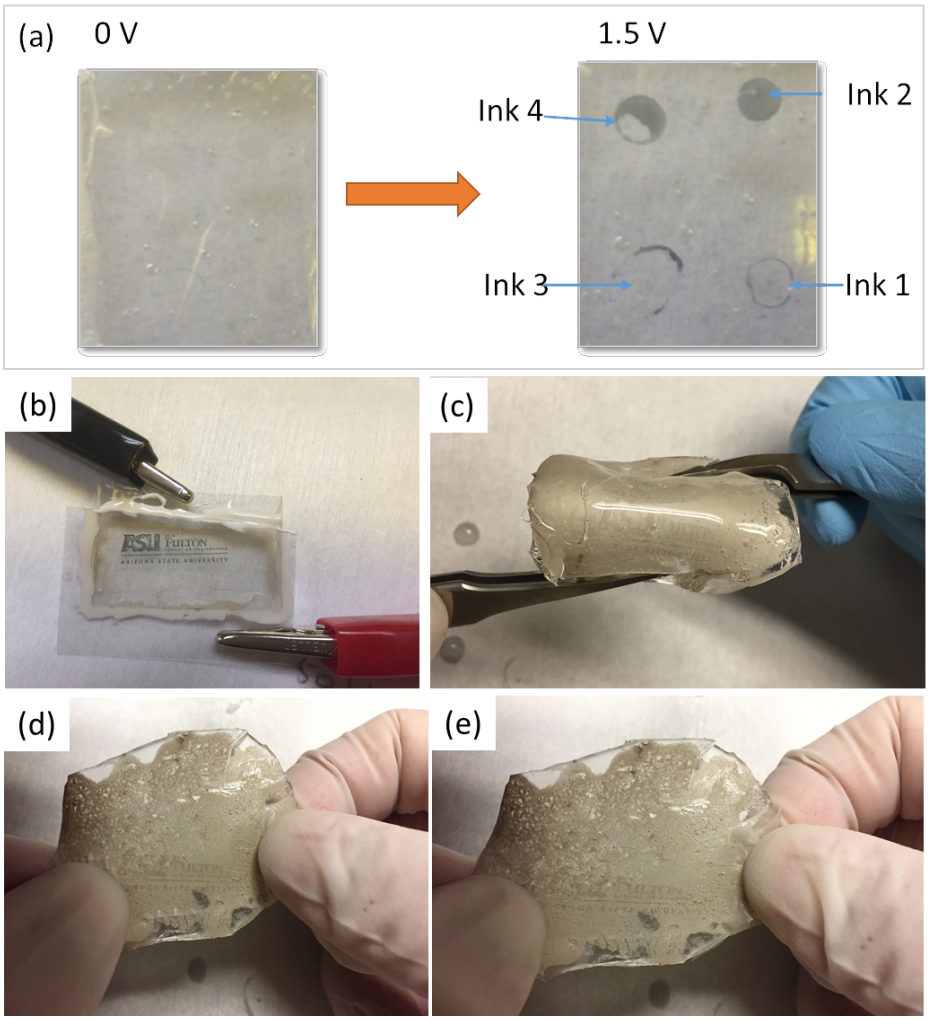

Figure 3.8: (a) Comparison of Ink coloration (b) Printed electrochromic device on ITO/PET (c) Printed electrochromic device on AgNW/PDMS under flexure (d) tension (e) compression

A stretchable capacitor (Figure 3.9(a)) and stretchable battery (Figure 3.9(b)) were formed without and with the inclusion of WO_3-based electrochromic ink, respectively. It can clearly be shown that the absence of WO_3, the system acts as a parallel-plate capacitor with $LiClO_4$ as the dielectric, with a 250 μm separation distance and area of 1 cm^2. In Figure 3.9(a), Charge-discharge cycles of the stretchable device was performed at a constant current density of 1 A/g at no applied tensile strain. Figure 3.9(b) shows the increase in specific capacitance with each

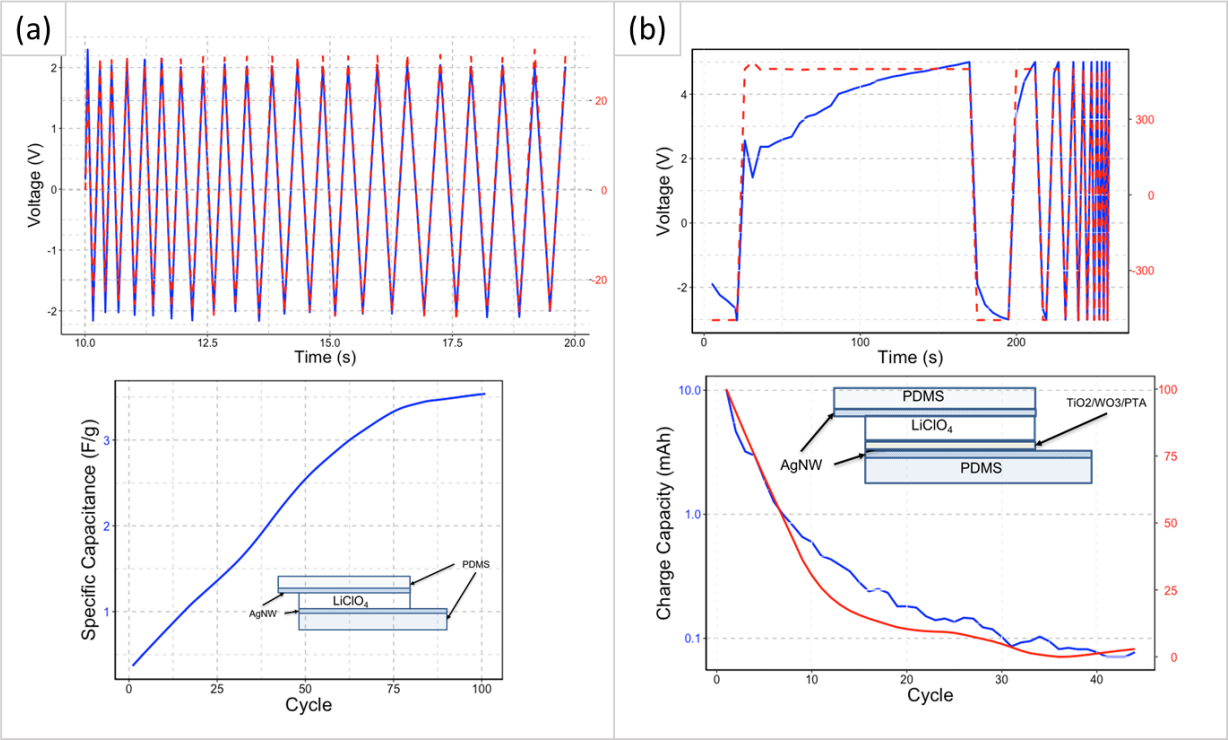

Figure 3.9: (a) Capacitive cycling and specific capacitance per cycle for device without EC ink and (b) voltage cycling and charge capacity per cycle for device with electrochromic ink

charge/discharge cycle, and saturating at 3.5 F/g. More cycling attempts are needed to understand the stability of the capacitor and to ensure that saturation behavior continues past 100 cycles. The specific capacitance (C) was calculated from the slope of the discharge capacitance (Yu *et al.*, 2009):

$$C = \frac{2I}{m\frac{\Delta V}{\Delta t}} \tag{3.1}$$

where I is the applied current and m is the average mass of the two AgNW electrodes. A cycling study was then conducted with WO_3 based ink on one set of AgNW electrodes and results clearly demonstrate charging (and electrochromic effect) from lithium intercolation (Figure 5c). In Figure 3.9(d), the areal capacity of battery device degrades considerably after each charging cycle, which indicates asymmetry either in the applied voltage offset or that the EC ink is inefficient at charge storage.

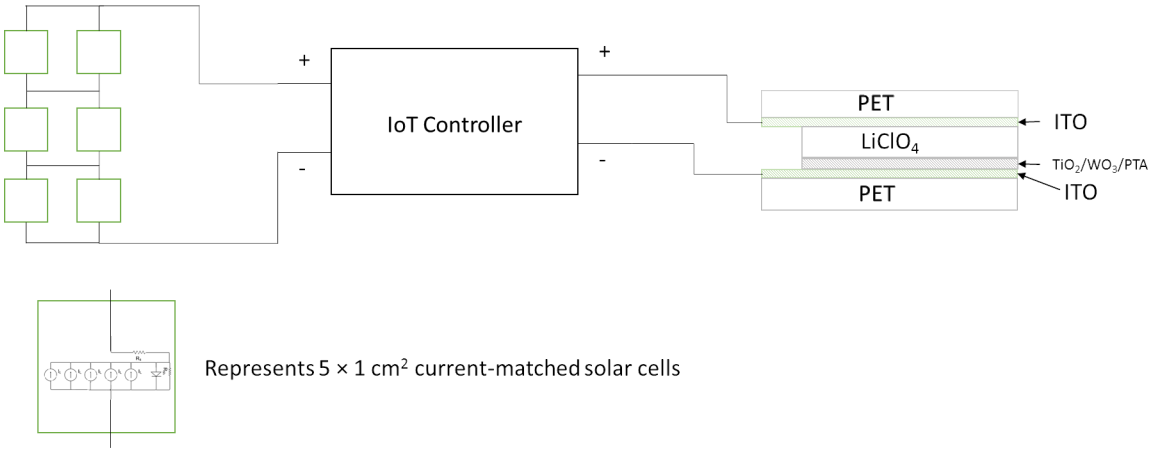

Figure 3.10: Circuit model of self-powered electrochromic device

Several OPV modules (3-6) wired in series (to increase voltage) and parallel (to current match) configurations, as well as the electrochromic device were paired using an Internet of Things (IoT) controller described in a configuration illustrated in Figure 3.1(b) and Figure 3.10. A pulse-width modulated output train was generated by the microcontroller (powered by the OPV device) which allowed for the tuning of the output potential. As a user changes intensity from a slider component provided by the mobile application, the electrochromic device treated as the load is accordingly transitioned.

3.5 Conclusion

In conclusion, self-powered electrochromic devices composed of dual-phased, inkjet printed TiO_2/WO_3/PTA nanoparticles for as the electrochromic device, and PCDTBT:PC_{70}BM organic solar cells were demonstrated on a stretchable platform. Electrochromic devices demonstrated excellent performance with 7 second coloration time, 8 s bleaching time, and 0.36-0.75 optical modulation at λ=525 nm. Organic cells demonstrated high power conversion efficiency needed to active and control the power delivery system (with PCE $\approx$ 3%, V_{oc} = 0.9V and $J_{sc} \approx$ 10-15 mA/cm^2),

enabled by an IoT personal controller. This work demonstrates the feasibility and potential impact of personalized, on-demand control of wearable smart-skins.

Chapter 4

CONCLUSION

In this dissertation, the integration of photovoltaic and electrochromic devices for self-powered smart window applications has been investigated. The design constraints for realizing such an integrated device may significantly interact with one another, compounding its complexity. For a photovoltaic device, high transparency yields reduced utilization of the terrestrial solar spectrum, and electrochromic films should be chosen such that the power requirements for initiating the reduction-oxidation reaction are minimal. This should be considered in conjunction with low transition (coloration and bleaching) times, and high optical density. The focus of this dissertation has been toward investigating three classes of solar cells (inorganic, hybrid organic, and fully organic) devices toward minimally powering electrochromic optimized for low transition voltages.

Inorganic Zinc Oxide (ZnO) thin film-based metal-semiconductor (MS), metal-insulator-semiconductor (MIS), and p-i-n heterojunction devices were investigated, and their photovoltaic conversion under ultraviolet (UV) illumination was evaluated. For MS devices, photoconductive behavior under ultraviolet illumination (λ=365 nm), suggesting the outsized role of surface states. Fitted against the generalized Bardeen model, Schottky parameters were used to estimate the density of interface states (D_{it} $\approx 8.0\times10^{11}$ $eV^{-1}cm^{-2}$) and the neutral level ($E_o \approx$ -5.2 eV). Post-metalization oxygen plasma treatment of Ag and Ti/Ag electrodes resulted in a net Schottky barrier height increase; linked to the formation of Ag_2O and TiO_x. The effective barrier potential maximized with a 20 Å electron blocking layer (EBL, SiO_2), suppressing recombination at the metal/semiconductor interface and blocking majority carrier current flow.

Photovoltaic performance of p-i-n heterojunction structures was maximized generating an open-circuit voltage (V_{oc}) of 1.2 V and short circuit current density (J_{sc}) of 0.68 mA/cm^2 for interdigitated devices under high energy monochromatic UV-C radiation. When properly scaled, ZnO thin film absorbers with sufficiently thin EBL and high surface barrier electrodes are suitable for visibly transparent, low-power smart-windows.

A fully organic photovoltaic, composed of poly[N-9'-heptadecanyl-2,7-carbazole-alt-5,5-(4',7'-di-2-thienyli2',1',3'-benzothiadiazole)]:phenyl-C71-butyric-acid-methyl (PCDTBT:PC70BM) was explored the final alternative approach toward powering electrochromic devices. The bulk heterojunction exhibited high transparency and relatively large power conversion efficiency and provided the requisite power for transitioning an inkjet printed, nano-particle-based, tungsten trioxide (WO_3) electrochromic films on substrates of varying mechanical flexibility. The printed electrochromic devices demonstrated clear switching behavior under external bias, with 7 second coloration time, 8 second bleaching time, and 0.36-0.75 optical modulation at λ=525 nm. The bulk heterojunction devices were evaluated with varying hole-transport layers and substrates, and exhibited the strongest performance of PCE$\approx$ 3%, V_{oc}=0.9V and J_{sc} $\approx$ 10-15 mA/cm^2. The devices were paired using an Internet of Things controller enabling wireless switching.

The purview of this dissertation focuses on the pairing of photovoltaic and electrochromic devices. The realization of such an integrated smart window presents various challenges that require tradeoffs among device design, selection of electrical and optical materials, and reproducibility/reliability of low-temperature processing. Here, we focused on the processing and performance of three classes of visibly-transparent photovoltaic materials. This interdisciplinary research approach, allowing for the reconciliation of multiple goals and trade-offs within a single design problem. The stages

of planning, executing, and analysis requires extensive due diligence in addition to confirming abstract expectations realized in the physical world. The broader impact of this work may affect household and building envelope energy consumption with the novel integrated device presented. Furthermore, the use of organic and nanomaterials may accelerate the pace of manufacturability of the burgeoning field of self-powered electrochromic devices.

BIBLIOGRAPHY

Allen, M. W., M. M. Alkaisi and S. M. Durbin, "Metal Schottky diodes on Zn-polar and O-polar bulk ZnO", Applied Physics Letters **89**, 10, 103520, URL http://doi.org/10.1063/1.2346137 (2006).

Allen, M. W. and S. M. Durbin, "Influence of oxygen vacancies on schottky contacts to ZnO", Applied Physics Letters **92**, 12, 122110, URL http://doi.org/10.1063/1.2894568 (2008).

Allen, M. W., S. M. Durbin and J. B. Metson, "Silver oxide schottky contacts on n-type ZnO", Applied Physics Letters **91**, 5, 053512, URL http://doi.org/10.1063/1.2768028 (2007).

Allen, M. W., R. J. Mendelsberg, R. J. Reeves and S. M. Durbin, "Oxidized noble metal Schottky contacts to n-type ZnO", Applied Physics Letters **94**, 10, N.PAG, URL http://doi.org/10.1063/1.3089871 (2009).

Ambrico, M., A. Cardone, T. Ligonzo, V. Augelli, P. F. Ambrico, S. Cicco, G. M. Farinola, M. Filannino, G. Perna and V. Capozzi, "Hysteresis-type current–voltage characteristics in Au/eumelanin/ITO/glass structure: Towards melanin based memory devices", Organic Electronics **11**, 11, 1809–1814, URL http://doi.org/10.1016/j.orgel.2010.08.001 (2010).

Amiruddin, R. and M. S. Kumar, "Role of p-NiO electron blocking layers in fabrication of (PN): ZnO/Al: ZnO UV photodiodes", Current Applied Physics **16**, 9, 1052–1061, URL http://doi.org/10.1016/j.cap.2016.06.003 (2016).

Andersson, P., R. Forchheimer, P. Tehrani and M. Berggren, "Printable All-Organic Electrochromic Active-Matrix Displays", Advanced Functional Materials **17**, 16, 3074–3082, URL http://doi.org/10.1002/adfm.200601241 (2007).

Angmo, D., T. T. Larsen-Olsen, M. Jørgensen, R. R. Søndergaard and F. C. Krebs, "Roll-to-Roll Inkjet Printing and Photonic Sintering of Electrodes for ITO Free Polymer Solar Cell Modules and Facile Product Integration", Advanced Energy Materials **3**, 2, 172–175, URL http://doi.org/10.1002/aenm.201200520 (2013).

Arena, A., N. Donato and G. Saitta, "Electrical characterization of solid-state heterojunctions between PEDOT:PSS and an anionic polyelectrolyte", Microelectronics Journal **38**, 6–7, 678–681, URL http://doi.org/10.1016/j.mejo.2007.05.011 (2007).

Aydogan, S., K. Cinar, H. Asil, C. Coskun and A. Turut, "Electrical characterization of Au/n-ZnO Schottky contacts on n-Si", Journal of Alloys and Compounds **476**, 1–2, 913–918, URL http://doi.org/10.1016/j.jallcom.2008.09.131 (2009).

Azhar, E. A., J. Vanjaria, S. Ahn, T. Fou, S. K. Dey, T. Salagaj, N. Sbrockey, G. S. Tompa and H. Yu, "Vapor-Transport Synthesis and Annealing Study of ZnxMg1xo Nanowire Arrays for Selective, Solar-Blind UV-C Detection", ACS Omega URL http://doi.org/10.1021/acsomega.7b01362 (2018).

Babinec, S. J., Y. Chen, D. L. Dermody and J. B. Vincent, "Electrochromic display device and compositions useful in making such devices", International Classification G02F1/155, G02F1/15, G02F1/17, C09K9/02; Cooperative Classification G02F1/176, G02F1/155, C09K9/02, G02F1/1523, G02F2001/1519; European Classification C09K9/02, G02F1/155, G02F1/15V, G02F1/17F (2004).

Bailey-Salzman, R. F., B. P. Rand and S. R. Forrest, "Semitransparent organic photovoltaic cells", Applied Physics Letters **88**, 23, 233502, URL http://doi.org/10.1063/1.2209176 (2006).

Banerjee, A. N. and K. K. Chattopadhyay, "Recent developments in the emerging field of crystalline p-type transparent conducting oxide thin films", Progress in Crystal Growth and Characterization of Materials **50**, 1-3, 52–105, URL http://doi.org/10.1016/j.pcrysgrow.2005.10.001, wOS:000235848000003 (2005).

Baxter, J. B. and E. S. Aydil, "Nanowire-based dye-sensitized solar cells", Applied Physics Letters **86**, 5, 053114 (2005).

Beaupré, S. and M. Leclerc, "PCDTBT: en route for low cost plastic solar cells", Journal of Materials Chemistry A **1**, 37, 11097–11105, URL http://doi.org/10.1039/C3TA12420G (2013).

Bechinger, C. and B. A. Gregg, "Development of a new self-powered electrochromic device for light modulation without external power supply", Solar Energy Materials and Solar Cells **54**, 1–4, 405–410, URL http://doi.org/10.1016/S0927-0248(98)00092-0, 00035 (1998).

Benson, D. K. and H. M. Branz, "Design goals and challenges for a photovoltaic-powered electrochromic window covering", Solar Energy Materials and Solar Cells **39**, 2–4, 203–211, URL http://doi.org/10.1016/0927-0248(95)00041-0 (1995).

Bock, F. X., T. M. Christensen, S. B. Rivers, L. D. Doucette and R. J. Lad, "Growth and structure of silver and silver oxide thin films on sapphire", Thin Solid Films **468**, 1–2, 57–64, URL http://doi.org/10.1016/j.tsf.2004.04.009 (2004).

Bond, W. L., "Measurement of the Refractive Indices of Several Crystals", Journal of Applied Physics **36**, 5, 1674–1677, URL http://doi.org/10.1063/1.1703106 (1965).

Bowden, S. and C. Honsberg, "Pvcdrom: Open-circuit voltage", PVEducation, National Science Foundation, UNSW, Sydney, Canberra, Australia, http://pveducation. org/pvcdrom (2014).

Brillson, L. J., "The structure and properties of metal-semiconductor interfaces", Surface Science Reports **2**, 2, 123–326, URL http://doi.org/10.1016/0167-5729(82)90001-2 (1982).

Brillson, L. J. and Y. Lu, "ZnO schottky barriers and ohmic contacts", Journal of Applied Physics **109**, 12, 121301, URL http://doi.org/10.1063/1.3581173 (2011).

Cai, G., P. Darmawan, M. Cui, J. Chen, X. Wang, A. L.-S. Eh, S. Magdassi and P. S. Lee, "Inkjet-printed all solid-state electrochromic devices based on NiO/WO3 nanoparticle complementary electrodes", Nanoscale **8**, 1, 348–357, URL http://doi.org/10.1039/C5NR06995E (2015).

Cannavale, A., P. Cossari, G. E. Eperon, S. Colella, F. Fiorito, G. Gigli, H. J. Snaith and A. Listorti, "Forthcoming perspectives of photoelectrochromic devices: a critical review", **9**, 9, 2682–2719, URL http://doi.org/10.1039/C6EE01514J (2016).

Cao, B. Q., M. Lorenz, A. Rahm, H. v. Wenckstern, C. Czekalla, J. Lenzner, G. Benndorf and M. Grundmann, "Phosphorus acceptor doped ZnO nanowires prepared by pulsed-laser deposition", Nanotechnology **18**, 45, 455707, URL http://doi.org/10.1088/0957-4484/18/45/455707 (2007).

Card, H. C., "Photovoltaic properties of MIS-Schottky barriers", Solid-State Electronics **20**, 12, 971–976, URL http://doi.org/10.1016/0038-1101(77)90206-4 (1977).

Chang, S.-m. and W.-s. Liu, "The roles of surface-doped metal ions (V, Mn, Fe, Cu, Ce, and W) in the interfacial behavior of TiO2 photocatalysts", Applied Catalysis B: Environmental **156–157**, 466–475, URL http://doi.org/10.1016/j.apcatb.2014.03.044 (2014).

Charlson, E., A. Shah and J. Lien, "A new silicon schottky photovoltaic energy converter", in "Electron Devices Meeting, 1972 International", vol. 18, pp. 16–16 (1972), URL http://doi.org/10.1109/IEDM.1972.249272, 00005.

Chen, B.-H., S.-Y. Kao, C.-W. Hu, M. Higuchi, K.-C. Ho and Y.-C. Liao, "Printed Multicolor High-Contrast Electrochromic Devices", ACS Applied Materials & Interfaces **7**, 45, 25069–25076, URL http://doi.org/10.1021/acsami.5b08061 (2015).

Chen, G., F. Abou-Galala, Z. Xu and B. M. Sadler, "Experimental evaluation of LED-based solar blind NLOS communication links", Optics Express **16**, 19, 15059–15068, URL http://doi.org/10.1364/OE.16.015059 (2008).

Cheng, J., F. Xie, Y. Liu, W. E. I. Sha, X. Li, Y. Yang and W. C. H. Choy, "Efficient hole transport layers with widely tunable work function for deep HOMO level organic solar cells", Journal of Materials Chemistry A **3**, 47, 23955–23963, URL doi.org/10.1039/C5TA06878A (2015).

Chin, Y.-M., J.-C. Lin, Y.-J. Lin and K.-C. Wu, "Effects of ultraviolet treatment on the photovoltaic property of poly(3,4-ethylenedioxythiophene) doped with poly(4-styrenesulfonate)/n-type Si diodes", Solar Energy Materials and Solar Cells **94**, 12, 2154–2157, URL http://doi.org/10.1016/j.solmat.2010.07.002, 00017 (2010).

Chua, L., "If it's pinched it's a memristor", Semiconductor Science and Technology **29**, 10, 104001, URL http://doi.org/10.1088/0268-1242/29/10/104001 (2014).

Collins, C. J., U. Chowdhury, M. M. Wong, B. Yang, A. L. Beck, R. D. Dupuis and J. C. Campbell, "Improved solar-blind detectivity using an AlxGa1-xN heterojunction p-i-n photodiode", Applied Physics Letters **80**, 20, 3754–3756, URL http://doi.org/10.1063/1.1480484, wOS:000175564100030 (2002).

Constantinou, I., T.-H. Lai, H.-Y. Hsu, S.-H. Cheung, E. D. Klump, K. S. Schanze, S.-K. So and F. So, "Effect of Thermal Annealing on Charge Transfer States and Charge Trapping in PCDTBT:PC70bm Solar Cells", Advanced Electronic Materials **1**, 9, 1500167, URL http://doi.org/10.1002/aelm.201500167, wOS:000363091100009 (2015).

Corr, D., U. Bach, D. Fay, M. Kinsella, C. McAtamney, F. O'Reilly, S. N. Rao and N. Stobie, "Coloured electrochromic "paper-quality" displays based on modified mesoporous electrodes", Solid State Ionics **165**, 1–4, 315–321, URL http://doi.org/10.1016/j.ssi.2003.08.054 (2003).

Costa, C., C. Pinheiro, I. Henriques and C. A. T. Laia, "Electrochromic properties of inkjet printed vanadium oxide gel on flexible polyethylene terephthalate/indium tin oxide electrodes", ACS Applied Materials & Interfaces **4**, 10, 5266–5275, URL http://doi.org/10.1021/am301213b (2012a).

Costa, C., C. Pinheiro, I. Henriques and C. A. T. Laia, "Inkjet Printing of Sol–Gel Synthesized Hydrated Tungsten Oxide Nanoparticles for Flexible Electrochromic Devices", ACS Applied Materials & Interfaces **4**, 3, 1330–1340, URL http://doi.org/10.1021/am201606m, 00022 (2012b).

Cowley, A. M. and S. M. Sze, "Surface States and Barrier Height of Metal-Semiconductor Systems", Journal of Applied Physics **36**, 10, 3212–3220, URL http://doi.org/10.1063/1.1702952 (1965).

Cui, W., D. Guo, X. Zhao, Z. Wu, P. Li, L. Li, C. Cui and W. Tang, "Solar-blind photodetector based on Ga2o3 nanowires array film growth from inserted Al2o3 ultrathin interlayers for improving responsivity", **6**, 103, 100683–100689, URL http://doi.org/10.1039/C6RA16108A (2016).

Das, A. K., P. Misra, R. S. Ajimsha, A. Bose, S. C. Joshi, S. Porwal, T. K. Sharma, S. M. Oak and L. M. Kukreja, "Effect of Mg diffusion on photoluminescence spectra of MgZnO/ZnO bi-layers annealed at different temperatures", Journal of Applied Physics **114**, 18, 183103, URL http://doi.org/10.1063/1.4830010 (2013).

Das, S. and T. L. Alford, "Optimization of the zinc oxide electron transport layer in P $_3$ HT:PC $_{61}$ BM based organic solar cells by annealing and yttrium doping", RSC Adv. **5**, 57, 45586–45591, URL http://doi.org/10.1039/C5RA05258K (2015).

Das, S., J.-Y. Choi and T. L. Alford, "P3ht:PC61bm based solar cells employing solution processed copper iodide as the hole transport layer", Solar Energy Materials and Solar Cells **133**, 255–259, URL http://doi.org/10.1016/j.solmat.2014.11.004 (2015).

Das, S., J. Joslin and T. L. Alford, "Self-assembled monolayer modified ITO in P3ht:PC61bm organic solar cells with improved efficiency", Solar Energy Materials and Solar Cells **124**, 98–102, URL http://doi.org/10.1016/j.solmat.2014.01.048 (2014).

Das, S. N., Kyeong-Ju Moon, J. P. Kar, Ji-Hyuk Choi, Junjie Xiong, Tae Il Lee and Jae-Min Myoung, "ZnO single nanowire-based UV detectors", Applied Physics Letters **97**, 2, 022103, URL http://doi.org/10.1063/1.3464287 (2010).

Davy, N. C., M. Sezen-Edmonds, J. Gao, X. Lin, A. Liu, N. Yao, A. Kahn and Y.-L. Loo, "Pairing of near-ultraviolet solar cells with electrochromic windows for smart management of the solar spectrum", Nature Energy **2**, 8, 17104, URL http://doi.org/10.1038/nenergy.2017.104 (2017).

Deb, S. K., S.-H. Lee, C. E. Tracy, J. R. Pitts, B. A. Gregg and H. M. Branz, "Stand-alone photovoltaic-powered electrochromic smart window", Electrochimica Acta **46**, 13, 2125–2130 (2001).

Deepa, M., A. G. Joshi, A. K. Srivastava, S. M. Shivaprasad and S. A. Agnihotry, "Electrochromic Nanostructured Tungsten Oxide Films by Sol-gel: Structure and Intercalation Properties", Journal of The Electrochemical Society **153**, 5, C365–C376, URL http://doi.org/10.1149/1.2184072 (2006a).

Deepa, M., M. Kar and S. A. Agnihotry, "Electrodeposited tungsten oxide films: annealing effects on structure and electrochromic performance", Thin Solid Films **468**, 1-2, 32–42, URL http://doi.org/10.1016/j.tsf.2004.04.056 (2004).

Deepa, M., T. K. Saxena, D. P. Singh, K. N. Sood and S. A. Agnihotry, "Spin coated versus dip coated electrochromic tungsten oxide films: Structure, morphology, optical and electrochemical properties", Electrochimica Acta **51**, 10, 1974–1989, URL http://doi.org/10.1016/j.electacta.2005.06.027 (2006b).

Deepa, M., A. K. Srivastava, M. Kar and S. A. Agnihotry, "A case study of optical properties and structure of sol–gel derived nanocrystalline electrochromic WO 3 films", Journal of Physics D: Applied Physics **39**, 9, 1885, URL http://doi.org/10.1088/0022-3727/39/9/025 (2006c).

DeForest, N., A. Shehabi, J. O'Donnell, G. Garcia, J. Greenblatt, E. S. Lee, S. Selkowitz and D. J. Milliron, "United States energy and CO2 savings potential from deployment of near-infrared electrochromic window glazings", Building and Environment **89**, 107–117, URL http://doi.org/10.1016/j.buildenv.2015.02.021 (2015).

Dey, S. K., J.-J. Lee and P. Alluri, "Electrical Properties of Paraelectric (Pb 0.72la 0.28)TiO3 Thin Films with High Linear Dielectric Permittivity: Schottky and Ohmic Contacts", Japanese Journal of Applied Physics **34**, 6R, 3142, URL http://doi.org/10.1143/JJAP.34.3142 (1995).

Di Ventra, M. and Y. V. Pershin, "Memory materials: a unifying description", Materials Today **14**, 12, 584–591, URL http://doi.org/10.1016/S1369-7021(11)70299-1 (2011).

Distler, A., T. Sauermann, H.-J. Egelhaaf, S. Rodman, D. Waller, K.-S. Cheon, M. Lee and D. M. Guldi, "The Effect of PCBM Dimerization on the Performance of Bulk Heterojunction Solar Cells", Advanced Energy Materials **4**, 1, n/a–n/a, URL http://doi.org/10.1002/aenm.201300693 (2014).

Djurišić, A. B., Y. H. Leung, K. H. Tam, Y. F. Hsu, L. Ding, W. K. Ge, Y. C. Zhong, K. S. Wong, W. K. Chan, H. L. Tam, K. W. Cheah, W. M. Kwok and D. L. Phillips, "Defect emissions in ZnO nanostructures", Nanotechnology **18**, 9, 095702, URL http://doi.org/10.1088/0957-4484/18/9/095702 (2007).

Dong, B., G. Xu, X. Luo, Y. Cai and W. Gao, "A bibliometric analysis of solar power research from 1991 to 2010", Scientometrics **93**, 3, 1101–1117 (2012).

Dyer, A. L., R. H. Bulloch, Y. Zhou, B. Kippelen, J. R. Reynolds and F. Zhang, "A Vertically Integrated Solar-Powered Electrochromic Window for Energy Efficient Buildings", Advanced Materials **26**, 28, 4895–4900, URL http://doi.org/10.1002/adma.201401400 (2014).

EIA, "EIA - Annual Energy Outlook 2017", (2017).

El-Shimy, M. A. and S. Hranilovic, "Binary-Input Non-Line-of-Sight Solar-Blind UV Channels: Modeling, Capacity and Coding", Journal of Optical Communications and Networking **4**, 12, 1008–1017, URL http://doi.org/10.1364/JOCN.4.001008 (2012).

Etzold, F., I. A. Howard, R. Mauer, M. Meister, T.-D. Kim, K.-S. Lee, N. S. Baek and F. Laquai, "Ultrafast Exciton Dissociation Followed by Nongeminate Charge Recombination in PCDTBT:PCBM Photovoltaic Blends", Journal of the American Chemical Society **133**, 24, 9469–9479, URL http://doi.org/10.1021/ja201837e (2011).

Fan, Z., J. C. Ho, Z. A. Jacobson, R. Yerushalmi, R. L. Alley, H. Razavi and A. Javey, "Wafer-Scale Assembly of Highly Ordered Semiconductor Nanowire Arrays by Contact Printing", Nano Letters **8**, 1, 20–25, URL http://doi.org/10.1021/nl071626r (2008).

Fan, Z., J. C. Ho, T. Takahashi, R. Yerushalmi, K. Takei, A. C. Ford, Y.-L. Chueh and A. Javey, "Toward the Development of Printable Nanowire Electronics and Sensors", Advanced Materials **21**, 37, 3730–3743, URL http://doi.org/10.1002/adma.200900860 (2009).

Faraz, S. M., M. Willander and Q. Wahab, "Interface state density distribution in Au/n-ZnO nanorods Schottky diodes", IOP Conference Series: Materials Science and Engineering **34**, 1, 012006, URL http://doi.org/10.1088/1757-899X/34/1/012006 (2012).

Feng, Z. C., *Handbook of zinc oxide and related materials: volume two, devices and nano-engineering*, vol. 2 (CRC press, 2012).

Fonash, S., *Solar Cell Device Physics, Second Edition* (Academic Press, Burlington, MA, 2010), 2 edition edn.

Gajdoš, M., A. Eichler and J. Hafner, "Ab initio density functional study of O on the Ag(0 0 1) surface", Surface Science **531**, 3, 272–286, URL http://doi.org/10.1016/S0039-6028(03)00514-4 (2003).

Ganapati, P., "Ntera Prints a Display on Almost Any Surface", URL https://www.wired.com/2010/04/ntera-printable-display/ (2010).

Greene, L. E., M. Law, D. H. Tan, M. Montano, J. Goldberger, G. Somorjai and P. Yang, "General Route to Vertical ZnO Nanowire Arrays Using Textured ZnO Seeds", Nano Letters **5**, 7, 1231–1236, URL http://doi.org/10.1021/nl050788p (2005).

Hagiwara, Y., T. Nakada and A. Kunioka, "Improved jsc in CIGS thin film solar cells using a transparent conducting ZnO:b window layer", Solar Energy Materials and Solar Cells **67**, 1–4, 267–271, URL http://doi.org/10.1016/S0927-0248(00)00291-9 (2001).

Han, H., J. W. Mayer and T. L. Alford, "Effect of various annealing environments on electrical and optical properties of indium tin oxide on polyethylene napthalate", Journal of Applied Physics **99**, 12, 123711, URL http://doi.org/10.1063/1.2204815 (2006).

Han-Ki Kim, R. S. Kyoung-Kook Kim, Seong-Ju Park, Tae-Yeon Seong and I. Adesida, "Formation of low resistance nonalloyed Al/Pt ohmic contacts on n-type ZnO epitaxial layer", Journal of Applied Physics **94**, 6, 4225 (2003).

Hao, Y.-M., S.-Y. Lou, S.-M. Zhou, R.-J. Yuan, G.-Y. Zhu and N. Li, "Structural, optical, and magnetic studies of manganese-doped zinc oxide hierarchical microspheres by self-assembly of nanoparticles", Nanoscale Research Letters **7**, 1, 100, URL http://doi.org/10.1186/1556-276X-7-100 (2012).

Herrera Rocher, F. R., "Ag NWs for Organic Photovoltaic Cells: Semitransparent and Stretchable Devices", (2015).

Hong, Y.-K., D.-W. Lee, H.-J. Eom and K.-Y. Lee, "The catalytic activity of Sulfided Ni/W/TiO2 (anatase) for the hydrodeoxygenation of Guaiacol", Journal of Molecular Catalysis A: Chemical **392**, 241–246, URL http://doi.org/10.1016/j.molcata.2014.05.025 (2014).

Hsu, N. E., W. K. Hung and Y. F. Chen, "Origin of defect emission identified by polarized luminescence from aligned ZnO nanorods", Journal of Applied Physics **96**, 8, 4671–4673, URL http://doi.org/10.1063/1.1787905 (2004).

Huang, L.-M., C.-W. Hu, H.-C. Liu, C.-Y. Hsu, C.-H. Chen and K.-C. Ho, "Photovoltaic electrochromic device for solar cell module and self-powered smart glass applications", Solar Energy Materials and Solar Cells **99**, 154–159, URL http://doi.org/10.1016/j.solmat.2011.03.036, 00016 (2012a).

Huang, L.-M., C.-W. Hu, C.-Y. Peng, C.-H. Su and K.-C. Ho, "Integration of polyelectrolyte based electrochromic material in printable photovoltaic electrochromic module", Solar Energy Materials and Solar Cells **145, Part 1**, 69–75, URL http://doi.org/10.1016/j.solmat.2015.05.011 (2016).

Huang, L.-M., C.-P. Kung, C.-W. Hu, C.-Y. Peng and H.-C. Liu, "Tunable photovoltaic electrochromic device and module", Solar Energy Materials and Solar Cells **107**, 390–395, URL http://doi.org/10.1016/j.solmat.2012.07.021 (2012b).

Huso, J., H. Che, D. Thapa, A. Canul, M. D. McCluskey and L. Bergman, "Phonon dynamics and Urbach energy studies of MgZnO alloys", Journal of Applied Physics **117**, 12, 125702, URL http://doi.org/10.1063/1.4916096 (2015).

Huso, J., H. Che, D. Thapa, J. L. Morrison, M. G. Norton and L. Bergman, "Phonon dynamics and anharmonicity in phase segregated structural domains of MgZnO film", Applied Physics Letters **104**, 3, 031908, URL http://doi.org/10.1063/1.4863094, 00001 (2014).

Huso, J., J. L. Morrison, H. Hoeck, E. Casey, L. Bergman, T. D. Pounds and M. G. Norton, "Low temperature LO-phonon dynamics of MgZnO nanoalloys", Applied Physics Letters **91**, 11, 111906, URL http://doi.org/10.1063/1.2784189, 00015 (2007).

Hussain, I., M. Y. Soomro, N. Bano, O. Nur and M. Willander, "Interface trap characterization and electrical properties of Au-ZnO nanorod Schottky diodes by conductance and capacitance methods", Journal of Applied Physics **112**, 6, 064506, URL http://doi.org/10.1063/1.4752402 (2012).

Hwang, D.-K., M.-C. Jeong and J.-M. Myoung, "Effects of deposition temperature on the properties of Zn1xMgxO thin films", Applied Surface Science **225**, 1–4, 217–222, URL http://doi.org/10.1016/j.apsusc.2003.10.003 (2004).

IDTechEx, I., "Electrochromic displays progress | IDTechEx Research Article", URL https://www.printedelectronicsworld.com/articles/315/electrochromic-displays-progress (2005).

Javey, A., "Nano for Macro: The Integration of Nanomaterials for High Performance Flexible Marco-Electronics", Nanotechnology Law & Business **3**, 14 (2006).

Ji, L.-W., C.-Z. Wu, C.-M. Lin, T.-H. Meen, K.-T. Lam, S.-M. Peng, S.-J. Young and C.-H. Liu, "Characteristic Improvements of ZnO-Based Metal–Semiconductor–Metal Photodetector on Flexible Substrate with ZnO Cap Layer", Japanese Journal of Applied Physics **49**, 5R, 052201, URL http://doi.org/10.1143/JJAP.49.052201 (2010).

Jiang, D. Y., J. Y. Zhang, K. W. Liu, Y. M. Zhao, C. X. Cong, Y. M. Lu, B. Yao, Z. Z. Zhang and D. Z. Shen, "A high-speed photoconductive UV detector based on an Mg 0.4 Zn 0.6 O thin film", Semiconductor Science and Technology **22**, 7, 687, URL http://doi.org/10.1088/0268-1242/22/7/001 (2007).

Jung, S., A. Sou, K. Banger, D.-H. Ko, P. C. Y. Chow, C. R. McNeill and H. Sirringhaus, "All-Inkjet-Printed, All-Air-Processed Solar Cells", Advanced Energy Materials **4**, 14, n/a–n/a, URL http://doi.org/10.1002/aenm.201400432 (2014).

Kang, W., C. Yan, C. Y. Foo and P. S. Lee, "Foldable Electrochromics Enabled by Nanopaper Transfer Method", Advanced Functional Materials **25**, 27, 4203–4210, URL http://doi.org/10.1002/adfm.201500527 (2015).

Kar, J. P., M. C. Jeong, W. K. Lee and J. M. Myoung, "Fabrication and characterization of vertically aligned ZnMgO/ZnO nanowire arrays", Materials Science and Engineering: B **147**, 1, 74–78, URL http://doi.org/10.1016/j.mseb.2007.11.010 (2008).

Karazhanov, S. Z., P. Ravindran, H. Fjellvag and B. G. Svensson, "Electronic structure and optical properties of znsio3 and zn2sio4", Journal of Applied Physics **106**, 12, 123701, URL http://doi.org/10.1063/1.3268445, wOS:000273216500041 (2009).

Kasap, S. O., *Principles of Electronic Materials and Devices* (McGraw-Hill Education, New York, NY, 2017), 4 edition edn.

Kawahara, J., P. Andersson Ersman, D. Nilsson, K. Katoh, Y. Nakata, M. Sandberg, M. Nilsson, G. Gustafsson and M. Berggren, "Flexible active matrix addressed displays manufactured by printing and coating techniques", Journal of Polymer Science Part B: Polymer Physics **51**, 4, 265–271, URL http://doi.org/10.1002/polb.23213 (2013).

Khalil, A., Z. Ahmed, F. Touati and M. Masmoudi, "Review on organic solar cells", in "2016 13th International Multi-Conference on Systems, Signals & Devices (SSD)", pp. 342–353 (IEEE, 2016).

Kim, D. C., J. H. Lee, S. K. Mohanta, H. K. Cho, H. Kim and J. Y. Lee, "Density and aspect ratio controlled MgZnO nanowire arrays by spontaneous phase separation effect", Crystengcomm **13**, 3, 813–818, URL http://doi.org/10.1039/c0ce00114g, wOS:000286387600018 (2011).

Kim, H. W., S. H. Shim and C. Lee, "Effects of thermal annealing on the properties of ZnO-coated MgO nanowires", Materials Science and Engineering: B **136**, 2–3, 148–153, URL http://doi.org/10.1016/j.mseb.2006.09.019 (2007).

Koerner, B., "View dynamic glass", URL https://lucept.com/2014/01/17/view-dynamic-glass/ (2014).

Kohan, A. F., G. Ceder, D. Morgan and C. G. Van de Walle, "First-principles study of native point defects in ZnO", Physical Review B **61**, 22, 15019–15027, URL http://doi.org/10.1103/PhysRevB.61.15019, wOS:000087654100029 (2000).

Krebs, F. C., *Polymer Photovoltaics: A Practical Approach* (SPIE Publications, Bellingham, Wash, 2008), illustrated edition edition edn.

Lamoreaux, R., D. Hildenbrand and L. Brewer, "High-temperature vaporization behavior of oxides ii. oxides of be, mg, ca, sr, ba, b, al, ga, in, tl, si, ge, sn, pb, zn, cd, and hg", Journal of Physical and Chemical Reference Data **16**, 3, 419–443 (1987).

Lange, M., C. P. Dietrich, J. Zuniga-Perez, H. v. Wenckstern, M. Lorenz and M. Grundmann, "MgZnO/ZnO quantum well nanowire heterostructures with large confinement energies", Journal of Vacuum Science & Technology A **29**, 3, 03A104, URL http://doi.org/10.1116/1.3531709, 00009 (2011).

Law, J. B. K. and J. T. L. Thong, "Simple fabrication of a ZnO nanowire photodetector with a fast photoresponse time", Applied Physics Letters **88**, 13, 133114, URL http://doi.org/10.1063/1.2190459 (2006).

Layani, M., P. Darmawan, W. L. Foo, L. Liu, A. Kamyshny, D. Mandler, S. Magdassi and P. S. Lee, "Nanostructured electrochromic films by inkjet printing on large area and flexible transparent silver electrodes", Nanoscale **6**, 9, 4572–4576, URL http://doi.org/10.1039/C3NR06890K (2014).

Lee, C.-T., T.-S. Lin and C.-H. Chen, "ZnO-Based Solar Blind Ultraviolet-B Photodetectors Using MgZnO Absorption Layer", Journal of Electronic Materials **44**, 12, 4722–4725, URL http://doi.org/10.1007/s11664-015-4068-y (2015).

Lee, E., "Advancement of Electrochromic Windows", (2006).

Li, W., C. W. Wu, W. G. Qin, G. C. Wang, S. Q. Lu, X. J. Dong, H. B. Dong and Q. L. Sun, "Characterization of photovoltage evolution of ZnO films using a scanning Kelvin probe system", Physica B: Condensed Matter **404**, 16, 2197–2201, URL http://doi.org/10.1016/j.physb.2009.04.026 (2009).

Li, W.-X., C. Stampfl and M. Scheffler, "Insights into the function of silver as an oxidation catalyst by \textit{ab initio} atomistic thermodynamics", Physical Review B **68**, 16, 165412, URL http://doi.org/10.1103/PhysRevB.68.165412 (2003).

Liang, S., H. Sheng, Y. Liu, Z. Huo, Y. Lu and H. Shen, "ZnO schottky ultraviolet photodetectors", Journal of Crystal Growth **225**, 2–4, 110–113, URL http://doi.org/10.1016/S0022-0248(01)00830-2 (2001).

Lim Dong Chan, Jeong Jae Hoon, Hong Kihyon, Nho Sungho, Lee Joo-Yul, Hoang Quoc Viet, Lee Sang Kyu, Pyo Kyunglim, Lee Dongil and Cho Shinuk, "Semitransparent plastic solar cell based on oxide-metal-oxide multilayer electrodes", Progress in Photovoltaics: Research and Applications **26**, 3, 188–195, URL http://doi.org/10.1002/pip.2965 (2017).

Lin, Y.-J., "Comment on "Schottky contact on a ZnO (0001) single crystal with conducting polymer" [Appl. Phys. Lett.91, 142113 (2007)]", Applied Physics Letters **92**, 4, 046101, URL http://doi.org/10.1063/1.2836949, 00006 (2008a).

Lin, Y.-J., "Hysteresis-type current-voltage characteristics of indium tin oxide/poly (3,4-ethylenedioxythiophene) doped with poly (4-styrenesulfonate)/indium tin oxide devices", Journal of Applied Physics **103**, 6, 063702, URL http://doi.org/10.1063/1.2885096 (2008b).

Lin, Y.-J., C.-C. Chang, S.-J. Cherng, J.-W. Chen and C.-M. Chen, "Manipulation of light harvesting for efficient dye-sensitized solar cell by doping an ultraviolet light-capturing fluorophore", Progress in Photovoltaics **23**, 1, 106–111, URL http://doi.org/10.1002/pip.2407 (2015).

Liu, H., Z. Wu, J. Hu, Q. Song, B. Wu, H. Lam Tam, Q. Yang, W. Hong Choi and F. Zhu, "Efficient and ultraviolet durable inverted organic solar cells based on an aluminum-doped zinc oxide transparent cathode", Applied Physics Letters **103**, 4, 043309, URL http://doi.org/10.1063/1.4816786 (2013).

Liu, W., S. Gu, S. Zhu, J. Ye, F. Qin, S. Liu, X. Zhou, L. Hu, R. Zhang, Y. Shi and Y. Zheng, "The deposition and annealing study of MOCVD ZnMgO", Journal of Crystal Growth **277**, 1–4, 416–421, URL http://doi.org/10.1016/j.jcrysgro.2005.01.086 (2005).

Liu, W., Y. Liang, H. Xu, L. Wang, X. Zhang, Y. Liu and S. Hark, "Heteroepitaxial Growth and Spatially Resolved Cathodoluminescence of ZnO/MgZnO Coaxial Nanorod Arrays", The Journal of Physical Chemistry C **114**, 39, 16148–16152, URL http://doi.org/10.1021/jp102395t (2010).

Liu, X., X. Wu, H. Cao and R. P. H. Chang, "Growth mechanism and properties of ZnO nanorods synthesized by plasma-enhanced chemical vapor deposition", Journal of Applied Physics **95**, 6, 3141–3147, URL http://doi.org/10.1063/1.1646440 (2004).

Lu, C. Y., S. P. Chang, S. J. Chang, Y. Z. Chiou, C. F. Kuo, H. M. Chang, C. L. Hsu and I. C. Chen, "Noise Characteristics of ZnO-Nanowire Photodetectors Prepared on ZnO:Ga/Glass Templates", IEEE Sensors Journal **7**, 7, 1020–1024, URL http://doi.org/10.1109/JSEN.2007.896567 (2007).

Lu, Y., Y. Lin, T. Xie, S. Shi, H. Fan and D. Wang, "Enhancement of visible-light-driven photoresponse of mn/ZnO system: photogenerated charge transfer properties and photocatalytic activity", Nanoscale **4**, 20, 6393–6400, URL http://doi.org/10.1039/C2NR31671D (2012).

Lunt, R. R., "Theoretical limits for visibly transparent photovoltaics", Applied Physics Letters **101**, 4, 043902–043902–4, URL http://doi.org/10.1063/1.4738896 (2012).

Mackintosh, A. R. and J. J. Liggat, "Dynamic mechanical analysis of poly(trimethylene terephthalate) - A comparison with poly(ethylene terephthalate) and poly(ethylene naphthalate)", Journal of Applied Polymer Science **92**, 5, 2791–2796, URL http://doi.org/10.1002/app.20290, wOS:000220759400007 (2004).

Mahmood, M. A., S. Baruah and J. Dutta, "Enhanced visible light photocatalysis by manganese doping or rapid crystallization with ZnO nanoparticles", Materials Chemistry and Physics **130**, 1–2, 531–535, URL http://doi.org/10.1016/j.matchemphys.2011.07.018 (2011).

Majumdar, H. S., A. Bandyopadhyay, A. Bolognesi and A. J. Pal, "Memory device applications of a conjugated polymer: Role of space charges", Journal of Applied Physics **91**, 4, 2433–2437, URL http://doi.org/10.1063/1.1445281 (2002).

Mannerbro, R., M. Ranlöf, N. Robinson and R. Forchheimer, "Inkjet printed electrochemical organic electronics", Synthetic Metals **158**, 13, 556–560, URL http://doi.org/10.1016/j.synthmet.2008.03.030 (2008).

Martensson, T., C. P. T. Svensson, B. A. Wacaser, M. W. Larsson, W. Seifert, K. Deppert, A. Gustafsson, L. R. Wallenberg and L. Samuelson, "Epitaxial IIIV Nanowires on Silicon", Nano Letters **4**, 10, 1987–1990, URL http://doi.org/10.1021/nl0487267 (2004).

Mayoufi, A., M. Faouzi Nsib and A. Houas, "Doping level effect on visible-light irradiation W-doped TiO2–anatase photocatalysts for Congo red photodegradation", Comptes Rendus Chimie **17**, 7–8, 818–823, URL http://doi.org/10.1016/j.crci.2014.01.019 (2014).

Meloni, S., T. Moehl, W. Tress, M. Franckevicius, M. Saliba, Y. H. Lee, P. Gao, M. K. Nazeeruddin, S. M. Zakeeruddin and U. Rothlisberger, "Ionic polarization-induced current–voltage hysteresis in ch3nh3pbx3 perovskite solar cells", Nature communications **7**, 10334 (2016).

Mercaldo, L. V., M. L. Addonizio, M. D. Noce, P. D. Veneri, A. Scognamiglio and C. Privato, "Thin film silicon photovoltaics: Architectural perspectives and technological issues", Applied Energy **86**, 10, 1836–1844, URL http://doi.org/10.1016/j.apenergy.2008.11.034 (2009).

Mishra, K. C., K. H. Johnson, B. G. DeBoer, J. K. Berkowitz, J. Olsen and E. A. Dale, "First principles investigation of electronic structure and associated properties of zinc orthosilicate phosphors", Journal of Luminescence **47**, 5, 197–206, URL http://doi.org/10.1016/0022-2313(91)90012-K (1991).

Mohammadnejad, S., S. E. Maklavani and E. Rahimi, "Dark Current Reduction in ZnO-Based MSM Photodetectors with Interfacial Thin Oxide Layer", in "2008 International Symposium on High Capacity Optical Networks and Enabling Technologies", pp. 259–264 (2008), URL http://doi.org/10.1109/HONET.2008.4810246.

Moller, M., N. Leyland, G. Copeland and M. Cassidy, "Self-powered electrochromic display as an example for integrated modules in printed electronics applications", The European Physical Journal - Applied Physics **51**, 03, URL http://doi.org/10.1051/epjap/2010105, 00005 (2010).

Moon, J. S., J. Jo and A. J. Heeger, "Nanomorphology of PCDTBT:PC70bm Bulk Heterojunction Solar Cells", Advanced Energy Materials **2**, 3, 304–308, URL http://doi.org/10.1002/aenm.201100667 (2012).

Moreno, I., N. Navascues, S. Irusta and J. Santamaría, "Silver nanowires/polycarbonate composites for conductive films", IOP Conference Series: Materials Science and Engineering **40**, 1, 012001, URL http://doi.org/10.1088/1757-899X/40/1/012001 (2012).

Moujoud, A., S. H. Oh, K. Y. Heo, K. W. Lee and H. J. Kim, "Indium zinc oxide ohmic contact to poly(3,4-ethylenedioxythiophene) poly(styrenesulfonate) induced by UV light", Organic Electronics **10**, 5, 785–790, URL http://doi.org/10.1016/j.orgel.2009.03.014 (2009).

Moujoud, A., S. H. Oh, H. S. Shin and H. J. Kim, "On the mechanism of conductivity enhancement and work function control in PEDOT:PSS film through UV-light treatment", physica status solidi (a) **207**, 7, 1704–1707, URL http://doi.org/10.1002/pssa.200983711 (2010).

Nakano, M., T. Makino, A. Tsukazaki, K. Ueno, A. Ohtomo, T. Fukumura, H. Yuji, S. Akasaka, K. Tamura, K. Nakahara *et al.*, "Transparent polymer Schottky contact for a high performance visible-blind ultraviolet photodiode based on ZnO", Applied Physics Letters **93**, 12, 351, URL http://doi.org/10.1063/1.2989125 (2008).

Nakano, M., A. Tsukazaki, R. Y. Gunji, K. Ueno, A. Ohtomo, T. Fukumura and M. Kawasaki, "Schottky contact on a ZnO (0001) single crystal with conducting polymer", Applied Physics Letters **91**, 14, 142113, URL http://doi.org/10.1063/1.2789697 (2007).

Nandi, S. K., S. Chatterjee, S. K. Samanta, P. K. Bose and C. K. Maiti, "Electrical characterization of low temperature deposited oxide films on ZnO/n-Si substrate", Bulletin of Materials Science **26**, 7, 693–697, URL http://doi.org/10.1007/BF02706765 (2003).

Nguyen, T.-T.-N., C.-Y. Chan and J.-L. He, "One-step inkjet printing of tungsten oxide-poly(3,4-ethylenedioxythiophene):polystyrene sulphonate hybrid film and its applications in electrochromic devices", Thin Solid Films **603**, 276–282, URL http://doi.org/10.1016/j.tsf.2016.02.031 (2016).

NREL, N., "Photovoltaic Research | NREL", URL https://www.nrel.gov/pv/ (2018).

NREL, x., "Organic Photovoltaic Solar Cells | Photovoltaic Research | NREL", (2016).

Ochiai, S., M. Uchiyama, S. Kannappan, R. Jayaraman and P.-K. Shin, "Evaluation of the Performance of an Organic Thin Film Solar Cell Prepared Using the Active Layer of Poly[[9-(1-octylnonyl)-9h-carbazole-2.7-diyl]-2.5-thiophenediyl-2.1.3-benzothiadiazole-4.7-Diyl-2.5-thiophenediyl]/[6,6]-Phenyl C $_{71}$ Butyric Acid Methyl Ester Composite Thin Film", Transactions on Electrical and Electronic Materials **13**, 1, 43–46, URL http://doi.org/10.4313/TEEM.2012.13.1.43 (2012).

Oh, B.-Y., M.-C. Jeong, T.-H. Moon, W. Lee, J.-M. Myoung, J.-Y. Hwang and D.-S. Seo, "Transparent conductive Al-doped ZnO films for liquid crystal displays", Journal of Applied Physics **99**, 12, 124505, URL http://doi.org/10.1063/1.2206417 (2006).

Ozgur, U., Y. I. Alivov, C. Liu, A. Teke, M. A. Reshchikov, S. Doğan, V. Avrutin, S.-J. Cho and H. Morkoç, "A comprehensive review of ZnO materials and devices", Journal of Applied Physics **98**, 4, 041301, URL http://doi.org/10.1063/1.1992666 (2005).

Parlak, E. A., T. Aslı Tumay, N. Tore, Sarıoğlan, P. Kavak and F. Türksoy, "Efficiency improvement of PCDTBT solar cells with silver nanoparticles", Solar Energy Materials and Solar Cells **110**, 58–62, URL http://doi.org/10.1016/j.solmat.2012.12.002 (2013).

Patel, M., H.-S. Kim, J. Kim, J.-H. Yun, S. J. Kim, E. H. Choi and H.-H. Park, "Excitonic metal oxide heterojunction (NiO/ZnO) solar cells for all-transparent module integration", Solar Energy Materials and Solar Cells **170**, 246–253, URL http://doi.org/10.1016/j.solmat.2017.06.006 (2017).

Peng, S.-M., Y.-K. Su, L.-W. Ji, C.-Z. Wu, W.-B. Cheng and W.-C. Chao, "ZnO Nanobridge Array UV Photodetectors", The Journal of Physical Chemistry C **114**, 7, 3204–3208, URL http://doi.org/10.1021/jp909299y (2010).

Petter Jelle, B., C. Breivik and H. Drolsum Røkenes, "Building integrated photovoltaic products: A state-of-the-art review and future research opportunities", Solar Energy Materials and Solar Cells **100**, 69–96, URL http://doi.org/10.1016/j.solmat.2011.12.016 (2012).

Piccolo, A. and F. Simone, "Performance requirements for electrochromic smart window", Journal of Building Engineering **3**, 94–103, URL http://doi.org/10.1016/j.jobe.2015.07.002 (2015).

Pietrzyk, M. A., M. Stachowicz, A. Wierzbicka, P. Dluzewski, D. Jarosz, E. Przezdziecka and A. Kozanecki, "Growth conditions and structural properties of ZnMgO nanocolumns on Si(111)", Journal of Crystal Growth **408**, 102–106, URL http://doi.org/10.1016/j.jcrysgro.2014.09.003 (2014).

Polyakov, A. Y., N. B. Smirnov, A. V. Govorkov, E. A. Kozhukhova, A. I. Belogorokhov, D. P. Norton, H. S. Kim and S. J. Pearton, "Shallow and Deep Centers in As-Grown and Annealed MgZnO/ZnO Structures with Quantum Wells", Journal of Electronic Materials **39**, 5, 601–607, URL http://doi.org/10.1007/s11664-009-0973-2 (2009).

Qi, J. and J. Peterson, "Nanocomposite Polymers for Smart Window Films | SBIR.gov", (2001).

Qingjiang, L., A. Khiat, I. Salaoru, C. Papavassiliou, X. Hui and T. Prodromakis, "Memory Impedance in TiO2 based Metal-Insulator-Metal Devices", Scientific Reports **4**, URL http://doi.org/10.1038/srep04522 (2014).

R. Mateker, W., J. D. Douglas, C. Cabanetos, I. T. Sachs-Quintana, J. A. Bartelt, E. T. Hoke, A. E. Labban, P. M. Beaujuge, J. M. J. Fréchet and M. D. McGehee, "Improving the long-term stability of PBDTTPD polymer solar cells through material purification aimed at removing organic impurities", Energy & Environmental Science **6**, 8, 2529–2537, URL doi.org/10.1039/C3EE41328D (2013).

Ratcliff, E. L., A. Garcia, S. A. Paniagua, S. R. Cowan, A. J. Giordano, D. S. Ginley, S. R. Marder, J. J. Berry and D. C. Olson, "Investigating the influence of interfacial contact properties on open circuit voltages in organic photovoltaic performance: work function versus selectivity", Advanced Energy Materials **3**, 5, 647–656 (2013).

Ratcliff, E. L., J. Meyer, K. X. Steirer, N. R. Armstrong, D. Olson and A. Kahn, "Energy level alignment in PCDTBT:PC70bm solar cells: Solution processed NiOx for improved hole collection and efficiency", Organic Electronics **13**, 5, 744–749, URL `http://doi.org/10.1016/j.orgel.2012.01.022` (2012).

Richardson, G., S. E. O'Kane, R. G. Niemann, T. A. Peltola, J. M. Foster, P. J. Cameron and A. B. Walker, "Can slow-moving ions explain hysteresis in the current–voltage curves of perovskite solar cells?", Energy & Environmental Science **9**, 4, 1476–1485 (2016).

Rogers, J. A., T. Someya and Y. Huang, "Materials and mechanics for stretchable electronics", Science (New York, N.Y.) **327**, 5973, 1603–1607, URL `http://doi.org/10.1126/science.1182383` (2010).

Rühle, S., A. Y. Anderson, H.-N. Barad, B. Kupfer, Y. Bouhadana, E. Rosh-Hodesh and A. Zaban, "All-oxide photovoltaics", The Journal of Physical Chemistry Letters **3**, 24, 3755–3764, URL `http://doi.org/10.1021/jz3017039` (2012).

Saha, S., S. K. Pandey, S. Nagar and S. Chakrabarti, "Effect of annealing temperature on optical and electrical properties of nitrogen implanted p-type ZnMgO thin films", Journal of Materials Science: Materials in Electronics **26**, 12, 9759–9765, URL `http://doi.org/10.1007/s10854-015-3646-3` (2015).

Said, E., P. Andersson, I. Engquist, X. Crispin and M. Berggren, "Electrochromic display cells driven by an electrolyte-gated organic field-effect transistor", Organic Electronics **10**, 6, 1195–1199, URL `http://doi.org/10.1016/j.orgel.2009.06.008` (2009).

Santos, L., P. Wojcik, J. V. Pinto, E. Elangovan, J. Viegas, L. Pereira, R. Martins and E. Fortunato, "Structure and Morphologic Influence of WO3 Nanoparticles on the Electrochromic Performance of Dual-Phase a-WO3/WO3 Inkjet Printed Films", Advanced Electronic Materials **1**, 1-2, n/a–n/a, URL `http://doi.org/10.1002/aelm.201400002` (2015).

Scheirs, J. and T. E. Long, *Modern Polyesters: Chemistry and Technology of Polyesters and Copolyesters* (John Wiley & Sons, 2005), google-Books-ID: ZgxgZ5vfxTkC.

Schroder, D. K., *Semiconductor Material and Device Characterization* (Wiley-IEEE Press, Piscataway, NJ : Hoboken, N.J, 2015), 3 edition edn.

Serreze, H. B., "Optimizing solar cell performance by simultaneous consideration of grid pattern design and interconnect configuration", 13th Photovoltaic Specialists Conference pp. 609–614 (1978).

Shankland, T. J., "Band Gap of Forsterite", Science **161**, 3836, 51–53 (1968).

Shimpi, P., Y. Ding, E. Suarez, J. Ayers and P.-X. Gao, "Annealing induced nanostructure and photoluminescence property evolution in solution-processed Mg-alloyed ZnO nanowires", Applied Physics Letters **97**, 10, 103104, URL http://doi.org/10.1063/1.3483614, 00012 (2010).

Shimpi, P., P.-X. Gao, D. G. Goberman and Y. Ding, "Low temperature synthesis and characterization of MgO/ZnO composite nanowire arrays", Nanotechnology **20**, 12, 125608, URL http://doi.org/10.1088/0957-4484/20/12/125608, 00038 (2009).

Singh, A., D. Kumar, P. K. Khanna, A. Kumar, M. Kumar and M. Kumar, "Anomalous behavior in ZnMgO thin films deposited by sol–gel method", Thin Solid Films **519**, 17, 5826–5830, URL http://doi.org/10.1016/j.tsf.2010.12.188 (2011).

Snaith, H. J., A. Abate, J. M. Ball, G. E. Eperon, T. Leijtens, N. K. Noel, S. D. Stranks, J. T.-W. Wang, K. Wojciechowski and W. Zhang, "Anomalous Hysteresis in Perovskite Solar Cells", The Journal of Physical Chemistry Letters **5**, 9, 1511–1515, URL http://doi.org/10.1021/jz500113x (2014).

Soci, C., A. Zhang, B. Xiang, S. A. Dayeh, D. P. R. Aplin, J. Park, X. Y. Bao, Y. H. Lo and D. Wang, "ZnO Nanowire UV Photodetectors with High Internal Gain", Nano Letters **7**, 4, 1003–1009, URL http://doi.org/10.1021/nl070111x (2007).

Son, D. I., B. W. Kwon, J. D. Yang, D. H. Park, B. Angadi and W. K. Choi, "High efficiency ultraviolet photovoltaic cells based on ZnO–C60 core–shell QDs with organic–inorganic multilayer structure", Journal of Materials Chemistry **22**, 3, 816–819, URL http://doi.org/10.1039/C1JM14555J (2011).

Son, D. I., B. W. Kwon, J. D. Yang, D. H. Park, W. S. Seo, H. Lee, Y. Yi, C. L. Lee and W. K. Choi, "Charge separation and ultraviolet photovoltaic conversion of ZnO quantum dots conjugated with graphene nanoshells", Nano Research **5**, 11, 747–761, URL http://doi.org/10.1007/s12274-012-0258-6 (2012).

Song, D., A. G. Aberle and J. Xia, "Optimisation of ZnO:al films by change of sputter gas pressure for solar cell application", Applied Surface Science **195**, 1–4, 291–296, URL http://doi.org/10.1016/S0169-4332(02)00611-6 (2002).

Spivak, J., "Smart Glass out of the Shadows", URL https://urbanland.uli.org/industry-sectors/infrastructure-transit/smart-glass-shadows/ (2016).

Staniec, P. A., A. J. Parnell, A. D. F. Dunbar, H. Yi, A. J. Pearson, T. Wang, P. E. Hopkinson, C. Kinane, R. M. Dalgliesh, A. M. Donald, A. J. Ryan, A. Iraqi, R. A. L. Jones and D. G. Lidzey, "The Nanoscale Morphology of a PCDTBT: PCBM Photovoltaic Blend", Advanced Energy Materials **1**, 4, 499–504, URL http://doi.org/10.1002/aenm.201100144, wOS:000293795800006 (2011).

Stashans, A., L. Eras and G. Chamba, "Modelling of al impurity in perovskite and ilmenite structures of mgsio3", Physics and Chemistry of Minerals **37**, 4, 191–199, URL http://doi.org/10.1007/s00269-009-0323-1 (2010).

Steckl, A. and G. Mohammed, "The Effect of Ambient Atmosphere in the Annealing of Indium Tin Oxide-Films", Journal of Applied Physics **51**, 7, 3890–3895, URL http://doi.org/10.1063/1.328135, wOS:A1980KA66600076 (1980).

Steirer, K. X., P. F. Ndione, N. E. Widjonarko, M. T. Lloyd, J. Meyer, E. L. Ratcliff, A. Kahn, N. R. Armstrong, C. J. Curtis, D. S. Ginley *et al.*, "Enhanced efficiency in plastic solar cells via energy matched solution processed niox interlayers", Advanced Energy Materials **1**, 5, 813–820 (2011).

Sun, Y., C. J. Takacs, S. R. Cowan, J. H. Seo, X. Gong, A. Roy and A. J. Heeger, "Efficient, Air-Stable Bulk Heterojunction Polymer Solar Cells Using MoOx as the Anode Interfacial Layer", Advanced Materials **23**, 19, 2226–2230, URL http://doi.org/10.1002/adma.201100038 (2011).

Swanson, R. M., "A vision for crystalline silicon photovoltaics", Progress in Photovoltaics: Research and Applications **14**, 5, 443–453, URL http://doi.org/10.1002/pip.709 (2006).

Sze, S. M. and K. K. Ng, *Physics of Semiconductor Devices* (Wiley-Interscience, Hoboken, N.J, 2006), 3 edition edn.

Tang, H., B. J. Kwon and J.-Y. Park, "Characterizations of individual ZnMgO nanowires synthesized by a vapor-transport method", physica status solidi (a) **207**, 11, 2478–2482, URL http://doi.org/10.1002/pssa.201026120, 00004 (2010).

Taylor, D. J., J. P. Cronin, L. F. Allard and D. P. Birnie, "Microstructure of Laser-Fired, SolGel-Derived Tungsten Oxide Films", Chemistry of Materials **8**, 7, 1396–1401, URL http://doi.org/10.1021/cm950570b (1996).

Thierry, R., G. Perillat-Merceroz, P. H. Jouneau, P. Ferret and G. Feuillet, "Core–shell multi-quantum wells in ZnO/ZnMgO nanowires with high optical efficiency at room temperature", Nanotechnology **23**, 8, 085705, URL http://doi.org/10.1088/0957-4484/23/8/085705, 00020 (2012).

Thomas, R., R. North and C. Norman, "Low-Cost - High-Efficiency Mis-Inversion Layer Solar-Cells", Electron Device Letters **1**, 5, 79–80, wOS:A1980JS29100005 (1980).

Ting Li, D. Lambert, M. Wong, C. Collins, B. Yang, A. Beck, U. Chowdhury, R. Dupuis and J. Campbell, "Low-noise back-illuminated Al/sub x/Ga/sub 1-x/N-based p-i-n solar-blind ultraviolet photodetectors", IEEE Journal of Quantum Electronics **37**, 4, 538–545, URL http://doi.org/10.1109/3.914403 (2001).

Tuzemen, E. , S. Eker, H. Kavak and R. Esen, "Dependence of film thickness on the structural and optical properties of ZnO thin films", Applied Surface Science **255**, 12, 6195–6200, URL http://doi.org/10.1016/j.apsusc.2009.01.078 (2009).

Ullah, R. and J. Dutta, "Photocatalytic degradation of organic dyes with manganese-doped ZnO nanoparticles", Journal of Hazardous Materials **156**, 1–3, 194–200, URL http://doi.org/10.1016/j.jhazmat.2007.12.033 (2008).

Unalan, H. E., P. Hiralal, N. Rupesinghe, S. Dalal, W. I. Milne and G. A. J. Amaratunga, "Rapid synthesis of aligned zinc oxide nanowires", Nanotechnology **19**, 25, 255608, URL http://doi.org/10.1088/0957-4484/19/25/255608 (2008).

Unger, E. L., E. T. Hoke, C. D. Bailie, W. H. Nguyen, A. R. Bowring, T. Heumüller, M. G. Christoforo and M. D. McGehee, "Hysteresis and transient behavior in current–voltage measurements of hybrid-perovskite absorber solar cells", Energy & Environmental Science **7**, 11, 3690–3698, URL http://doi.org/10.1039/C4EE02465F (2014).

US Department of Energy, x., "Annual energy outlook", (2018).

Vanheusden, K., W. L. Warren, C. H. Seager, D. R. Tallant, J. A. Voigt and B. E. Gnade, "Mechanisms behind green photoluminescence in ZnO phosphor powders", Journal of Applied Physics **79**, 10, 7983 (1996).

Vanjaria, J. V., E. A. Azhar and H. Yu, "Broad range tuning of structural and optical properties of zn(x)mg(1-x)o nanostructures grown by vapor transport method", Journal of Physics D: Applied Physics **49**, 46, 465103, URL http://doi.org/10.1088/0022-3727/49/46/465103 (2016).

Verrengia, J., "Smart Windows: Energy Efficiency with a View - News Feature | NREL", (2010).

Wang, D. H., J. K. Kim, J. H. Seo, O. O. Park and J. H. Park, "Stability comparison: A PCDTBT/PC71bm bulk-heterojunction versus a P3ht/PC71bm bulk-heterojunction", Solar Energy Materials and Solar Cells **101**, 249–255, URL doi.org/10.1016/j.solmat.2012.02.005 (2012).

Wang, J., C. Yan, G. Cai, M. Cui, A. Lee-Sie Eh and P. See Lee, "Extremely Stretchable Electroluminescent Devices with Ionic Conductors", Advanced Materials pp. n/a–n/a, URL http://doi.org/10.1002/adma.201504187 (2015).

Wei, X. Q., R. R. Zhao, Y. J. Wang, L. Y. Liu and B. Q. Cao, "Annealing effects in non-polar ZnMgO thin films fabricated by PLD", Surface Engineering **28**, 9, 678–682, URL http://doi.org/10.1179/1743294412Y.0000000042 (2012).

Wojcik, P. J., A. S. Cruz, L. Santos, L. Pereira, R. Martins and E. Fortunato, "Microstructure control of dual-phase inkjet-printed a-WO3/TiO2/WOX films for high-performance electrochromic applications", Journal of Materials Chemistry **22**, 26, 13268–13278, URL http://doi.org/10.1039/C2JM31217D (2012).

Wojcik, P. J., L. Pereira, R. Martins and E. Fortunato, "Statistical Mixture Design and Multivariate Analysis of Inkjet Printed a-WO3/TiO2/WOX Electrochromic Films", ACS Combinatorial Science **16**, 1, 5–16, URL http://doi.org/10.1021/co400011q (2014).

Wojcik, P. J., L. Santos, L. Pereira, R. Martins and E. Fortunato, "Tailoring nanoscale properties of tungsten oxide for inkjet printed electrochromic devices", Nanoscale **7**, 5, 1696–1708, URL http://doi.org/10.1039/C4NR05765A (2015).

Wong, K. V. and R. Chan, "Smart Glass and Its Potential in Energy Savings", Journal of Energy Resources Technology **136**, 1, 012002–012002–6, URL http://doi.org/10.1115/1.4024768 (2013).

Xia, F., L. T. Yang, L. Wang and A. Vinel, "Internet of things", International Journal of Communication Systems **25**, 9, 1101 (2012).

Xiang, B., P. Wang, X. Zhang, S. A. Dayeh, D. P. R. Aplin, C. Soci, D. Yu and D. Wang, "Rational Synthesis of p-Type Zinc Oxide Nanowire Arrays Using Simple Chemical Vapor Deposition", Nano Letters **7**, 2, 323–328, URL http://doi.org/10.1021/nl062410c (2007).

Xie, X., Z. Zhang, B. Li, S. Wang, M. Jiang, C. Shan, D. Zhao, H. Chen and D. Shen, "Enhanced solar-blind responsivity of photodetectors based on cubic MgZnO films via gallium doping", Optics Express **22**, 1, 246, URL http://doi.org/10.1364/OE.22.000246 (2014).

Xie, Z., X. Jin, G. Chen, J. Xu, D. Chen and G. Shen, "Integrated smart electrochromic windows for energy saving and storage applications", Chemical Communications **50**, 5, 608–610, URL http://doi.org/10.1039/C3CC47950A (2013).

Ya-Bin, Z., H. Wei, N. Jie, H. Fan, Z. Yue-Liang and C. Cong, "PEDOT:PSS Schottky contacts on annealed ZnO films", Chinese Physics B **20**, 4, 047301, URL http://doi.org/10.1088/1674-1056/20/4/047301 (2011).

Yakuphanoglu, F., "Controlling of electrical and interface state density properties of ZnO:Co/p-silicon diode structures by compositional fraction of cobalt dopant", Microelectronics Reliability **51**, 12, 2195–2199, URL http://doi.org/10.1016/j.microrel.2011.05.013 (2011).

Yan, C., X. Wang, M. Cui, J. Wang, W. Kang, C. Y. Foo and P. S. Lee, "Stretchable Silver-Zinc Batteries Based on Embedded Nanowire Elastic Conductors", Advanced Energy Materials **4**, 5, n/a–n/a, URL http://doi.org/10.1002/aenm.201301396 (2014).

Yang, J., X. Y. Li, F. Zhao, X. Y. Chen and P. Shao, "An Algorithm of Channel Sharing for the Solar Blind NLOS Ultraviolet Ad-Hoc Network Based on the Hybrid Genetic Algorithm", Applied Mechanics and Materials **543-547**, 2850–2853, URL http://doi.org/10.4028/www.scientific.net/AMM.543-547.2850 (2014).

Yang, X., Y. Gu, M. A. Migliorato and Y. Zhang, "Impact of insulator layer thickness on the performance of metal–MgO–ZnO tunneling diodes", Nano Research **9**, 5, 1290–1299, URL http://doi.org/10.1007/s12274-016-1024-y (2016a).

Yang, X., C.-X. Shan, Y.-J. Lu, X.-H. Xie, B.-H. Li, S.-P. Wang, M.-M. Jiang and D.-Z. Shen, "Transparent ultraviolet photovoltaic cells", Optics Letters **41**, 4, 685–688, URL http://doi.org/10.1364/OL.41.000685, wOS:000369942900008 (2016b).

Ye, J. D., K. W. Teoh, X. W. Sun, G. Q. Lo, D. L. Kwong, H. Zhao, S. L. Gu, R. Zhang, Y. D. Zheng, S. A. Oh, X. H. Zhang and S. Tripathy, "Effects of alloying and localized electronic states on the resonant Raman spectra of Zn1xMgxO nanocrystals", Applied Physics Letters **91**, 9, 091901, URL http://doi.org/10.1063/1.2775813 (2007).

Young, S. J., L. W. Ji, S. J. Chang and X. L. Du, "ZnO metal-semiconductor-metal ultraviolet photodiodes with Au contacts", Journal of the Electrochemical Society **154**, 1, H26–H29, URL http://doi.org/10.1149/1.2387058, wOS:000242538600065 (2007).

Yu, C., C. Masarapu, J. Rong, B. Wei and H. Jiang, "Stretchable Supercapacitors Based on Buckled Single-Walled Carbon-Nanotube Macrofilms", Advanced Materials **21**, 47, 4793–4797, URL http://doi.org/10.1002/adma.200901775 (2009).

Yu, H., E. A. Azhar, T. Belagodu, S. Lim and S. Dey, "ZnO nanowire based visible-transparent ultraviolet detectors on polymer substrates", **111**, 10, 102806, URL http://doi.org/10.1063/1.4714698 (2012a).

Yu, J.-S., I. Kim, J.-S. Kim, J. Jo, T. T. Larsen-Olsen, R. R. Søndergaard, M. Hösel, D. Angmo, M. Jørgensen and F. C. Krebs, "Silver front electrode grids for ITO-free all printed polymer solar cells with embedded and raised topographies, prepared by thermal imprint, flexographic and inkjet roll-to-roll processes", Nanoscale **4**, 19, 6032–6040, URL http://doi.org/10.1039/C2NR31508D (2012b).

Yu, X., J. Ma, F. Ji, Y. Wang, X. Zhang, C. Cheng and H. Ma, "Effects of sputtering power on the properties of ZnO:Ga films deposited by r.f. magnetron-sputtering at low temperature", Journal of Crystal Growth **274**, 3–4, 474–479, URL http://doi.org/10.1016/j.jcrysgro.2004.10.037 (2005).

Zhang, C., L. Xu, H. Zhang, J. Yang, J. Du and Z. Liu, "Determination of solid products from the de-polymerization of poly(trimethylene terephthalate) in supercritical methanol", Journal of Chromatography A **1055**, 1–2, 115–121, URL http://doi.org/10.1016/j.chroma.2004.08.146 (2004).

Zhang, W. F., Z. B. He, G. D. Yuan, J. S. Jie, L. B. Luo, X. J. Zhang, Z. H. Chen, C. S. Lee, W. J. Zhang and S. T. Lee, "High-performance, fully transparent, and flexible zinc-doped indium oxide nanowire transistors", Applied Physics Letters **94**, 12, 123103, URL http://doi.org/10.1063/1.3100194 (2009).

Zhang, Y., E. Bovill, J. Kingsley, A. R. Buckley, H. Yi, A. Iraqi, T. Wang and D. G. Lidzey, "PCDTBT based solar cells: one year of operation under real-world conditions", Scientific Reports **6**, 21632, URL http://doi.org/10.1038/srep21632 (2016).

Zhao, L., S. Zhao, Z. Xu, W. Gong, Q. Yang, X. Fan and X. Xu, "Influence of morphology of PCDTBT:PC71bm on the performance of solar cells", Applied Physics a-Materials Science & Processing **114**, 4, 1361–1368, URL http://doi.org/10.1007/s00339-013-7987-6, wOS:000332421700046 (2014).

Zhong, Y., X. Xia, W. Mai, J. Tu and H. J. Fan, "Integration of Energy Harvesting and Electrochemical Storage Devices", Advanced Materials Technologies **2**, 12, n/a–n/a, URL http://doi.org/10.1002/admt.201700182 (2017).

Zhou, J., Y. Gu, P. Fei, W. Mai, Y. Gao, R. Yang, G. Bao and Z. L. Wang, "Flexible Piezotronic Strain Sensor", Nano Letters **8**, 9, 3035–3040, URL http://doi.org/10.1021/nl802367t (2008).

Zhou, W. W., L. Sun, T. Yu, J. X. Zhang, H. Gong and H. J. Fan, "The morphology of Au@MgO nanopeapods", Nanotechnology **20**, 45, 455603, URL http://doi.org/10.1088/0957-4484/20/45/455603 (2009).

Zhu, L., G. Shao and J. K. Luo, "Numerical study of metal oxide Schottky type solar cells", Solid State Sciences **14**, 7, 857–863, URL http://doi.org/10.1016/j.solidstatesciences.2012.04.020 (2012).

APPENDIX A

EMPIRICAL MODELING OF PHOTO-ENHANCED CURRENT-VOLTAGE HYSTERESIS IN PEDOT:PSS/ZNO THIN FILM DEVICES

A.1 Abstract

Organic/inorganic "hybrid" semiconducting devices of zinc oxide (ZnO) thin films coated with poly (3,4-ethylenedioxythiophene):poly(4-styrenesulfonate) (PEDOT:PSS) were fabricated and electrically characterized. These devices exhibited photostimulated current-voltage (I-V) hysteresis behavior, in which dissimilar electrical current is observed based on the voltage sweep direction, notably as a function of the illuminated wavelength exposed on the device surface during electrical characterization. Ultraviolet-induced oxygen desorption on the ZnO surface, leading to electrons transitioning into the conduction band, gives rise to an increase of accumulated charges between the PEDOT:PSS and ZnO layers. This effect, coupled with trap states within PEDOT:PSS films, produces a hysteresis effect that is amplified by photoconduction. Characteristic I-V hysteresis was empirically modeled under a series of first-order multiple linear regression (MLR) expressions that decouple device processing and device characterization conditions. These models unravel and describe the numerical markers of hysteresis measured across the organic layer, including scaled and shifted transformations. The results of this analysis indicate that illumination is statistically a stronger explanatory variable for hysteresis than device size, which further suggests that stored space charges on the metal/polymer interface more significantly influence hysteresis than trapped charges alone.

A.2 Introduction

Organic conductive polymers have become integral to the growth of materials for flexible memory devices, such as "write-once, read-many" devices, potentially realizing low-cost memristive applications. As a highly effective hole transport material for organic photovoltaic and light emitting applications, poly(3,4-ethylenedioxythiophene) polystyrene sulfonate (PEDOT:PSS) has been extensively studied due to its tunable conductivity, solubility in water, transparency in the visible spectrum, and a high work function (Nakano *et al.*, 2007; Lin, 2008a). However, a particular artifact of spin-on PEDOT:PSS film-based devices is the presence of hysteresis in current-voltage (I-V) characteristics (Arena *et al.*, 2007; Ambrico *et al.*, 2010; Lin, 2008b), to which these discrepancies, for photovoltaic applications, can create highly inflated power conversion efficiencies. Studies of Peroskovite and other hybrid organic solar cells have established that the level of power generation can often be ambiguous when the voltage scan rate exceeds the time-scale required for the device to reach electronic steady state (Unger *et al.*, 2014; Snaith *et al.*, 2014). This phenomenon has been attributed to the presence of deep trap states within the organic layer, as well as stored space charges on the metal/polymer interface. Lin et al performed a controlled study of ITO/PEDOT:PSS devices, and described displacement current in terms of a differential model that related applied voltage, device area, and voltage sweep rate to the observed hysteresis (Lin, 2008b). This displacement current model has largely been applied to analyze open-hysteresis behavior (where the forward and reverse current-voltage characteristic do not intersect), while lacking specificity for pinched hysteresis (where the current intersects at or near the origin on the forward and return path, and which is necessary for memristor classification) (Chua, 2014).

Although the mechanics governing transport in PEDOT:PSS have been explored

extensively, few thorough attempts have been made toward numerically modeling such complex hysteresis behavior. Hysteresis response can manifest from a wide variety of processing conditions and device structure considerations, such as the choice of substrate, surface electrode, and PEDOT:PSS conductivity (as varied through solid content). Additionally, various conditions during characterization such as the spectra of illumination exposure, latent dwell time, and the number of repeated measurements on the same device can modify the PEDOT:PSS chemical structure, thereby having a significant effect on the shape and position of the hysteresis profile. Understanding the relative significance of factors that contribute to I-V hysteresis in PEDOT:PSS film-based devices provides a framework toward optimizing and diagnosing performance degradation in hybrid organic/inorganic optoelectronic devices.

In this study, a combinatorial experimental approach was used to generate a series of first-order empirical models from sets of extracted I-V hysteretic parameters, utilizing a multiple linear regression (MLR) methodology. Stepwise model selection techniques were employed to form a decision criteria toward filtering potential explanatory variables. The refined models were used to decouple the magnitude of relative effects of material, processing, and testing conditions on the hysteretic I-V behavior of PEDOT:PSS/ZnO thin film-based devices.

A.3 Experimental Details

Highly doped Si (p-type boron doped 20 mΩ-cm) and indium tin oxide (ITO, Delta Technologies, CG-61IN) were prepared by immersing in Piranha (70% sulfuric acid, 30% hydrogen peroxide) for 10 minutes and buffered oxide etchant (2% hydroflouric acid) for 5 minutes. A 1 μm ZnO electron transport layer was deposited via magnetron sputtering system (Lesker PVD 250) atop the substrates. An oxygen plasma treatment (200 W for 15 minutes, Tegal Asher) was applied to substrates and ZnO

thin films prior to spin coating in order to clean and passivate coated surfaces. Two conductive grades of PEDOT:PSS—Heraeus-Clevios PH 500 (1.0-1.3% solid content) and P VP AI 4083 (1.3-1.7% solid content)—were spun onto Si and ITO/SiO_2 substrates at 5000 rpm for 30 seconds, and were subsequently hotplate-baked at 160 °C for 5 minutes, each. Metallization was performed with an electron beam evaporator system (CHA 600-SE) with Al, Au, and Ag contacts, with five sets of circular patterns from ascending diameters of 300 - 700 μm. A schematic of device configurations and energy band diagrams are shown in Figure A.1.

Post-fabrication, vertical capacitance-voltage (C-V) measurements were conducted with a mercury probe system (Materials Development Corporation) with an attached LCR meter (HP4284). Current-voltage (I-V) characteristics were collected with a semiconductor analyzer system (Keithly 4200). Electrical testing was conducted under varying illumination conditions: dark, halogen broad band white light (Princeton Instruments TS-425), and monochromatic (λ=365 nm) ultraviolet (UVP EL Series). Characterization was also conducted under three different voltage sweep rates: 38.5 mV/s, 50 mV/s, 71.42 mV/s. The devices were allotted a latent "wait" period of approximately 5 minutes between measurements to stabilize response from prior measurements. Additionally, the effect of voltage amplitude, repeated bias stress, and dormant time between characterization was studied by varying applied voltage from [-3,3] V and [-5,5] V, repeating 10 voltage sweeps, and re-measuring after two years from a representative subset of devices, respectively. Exploratory analysis was first undertaken to screen for hysteresis behavior.

From each measurement, a set of parameters were exhaustively extracted in order to devise a descriptive empirical model correlating the variation of hysteresis parameters as a function of processing and characterization conditions. These parameters included the intersection point of the forward and return sweep, the loop areas formed

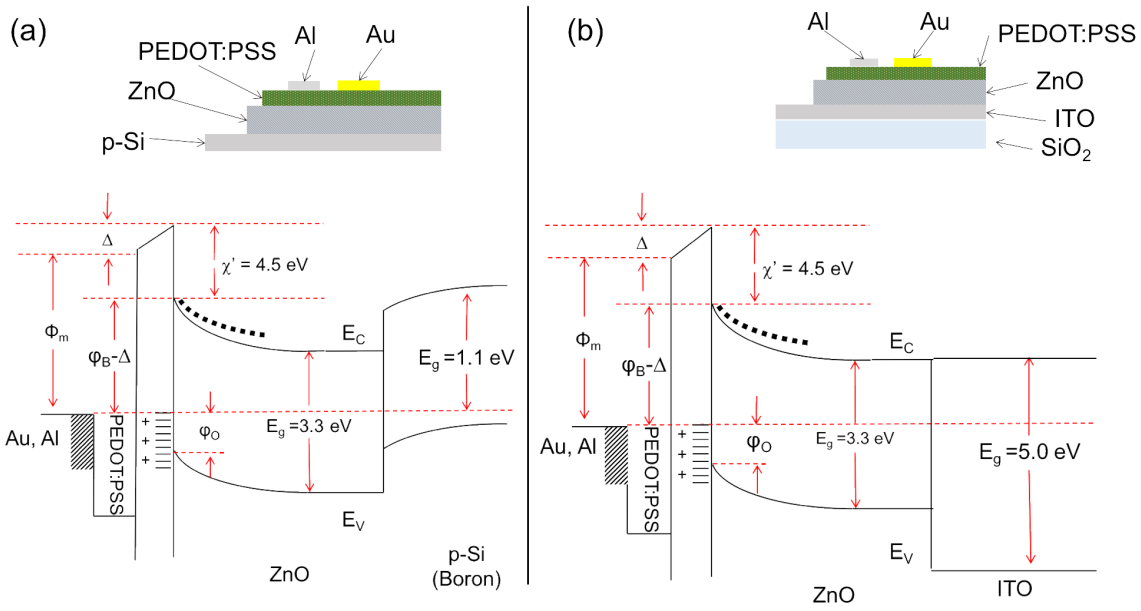

Figure A.1: Device Structure Schematic and Band Diagram of PEDOT:PSS/ZnO devices for (a) Si and (b) ITO Substrates

from the portions left and right of the intersection (numerically determined with a composite Simpson's 3/8 technique), and the axes intercepts: V_{oc+}, V_{oc-}, $I_{sc+}$and I_{sc-}, in which a positive subscript refers to a forward sweep, and a negative subscript refers to a reverse sweep (numerically determined with a modified Secant method). The extracted parameters were tabulated and treated as response variables, while the fabrication and testing conditions were treated as explanatory variables. Due to the large number of regressors, a first iteration of main effects were explored, and a series of stepwise model selection parameters including adjusted R^2 (forward and backward), Mallow's CP, and Baysian Information Criteria (BIC) were evaluated to compare models and to reduce the dimensionality of predictors. A refined model was generated and analyzed with the remaining regressors for each subset of hysteresis response variables. Post-processing of data, which included data set transformation, parameter extraction, model generation, model selection, and model visualization were performed in R language with the ggplot2 library.

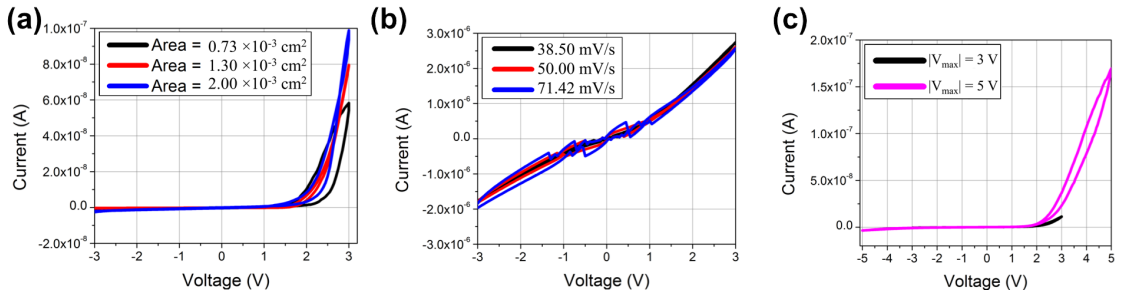

Figure A.2: Current-Voltage Measurements of PEDOT:PSS device with modified (a) device size (b) voltage sweep rate (c) amplitude

A.4 Results and Discussion

A.4.1 Exploratory Data Analysis

The degree of observed hysteresis, absent of illumination, was found to be a strong function of device size, voltage scan rate, and voltage amplitude, as illustrated in Figure A.2 (a), (b), and (c) respectively. The asymmetric current response between forward and reverse bias can be explained by the formation of a Schottky barrier with PEDOT:PSS in the case of Al, leading to rectifying behavior and suppressed conduction for negative bias. As noted by others (Lin, 2008b; Moujoud *et al.*, 2009; Ambrico *et al.*, 2010), this behavior has been explained in terms of the displacement current model, which relates the total current ($\sum$I) in terms of the linear sum of the resistive component (I_r) and the displacement component (I_d), as shown in equation (A.1).

$$\sum I = I_r + I_d = I_r + (V\frac{dC}{dt} + C\frac{dV}{dt}) \tag{A.1}$$

As device area (which is directly proportional to device capacitance) increases, displacement current increases, as shown in Figure A.2(a), and is modeled by varying C in equation (A.1). Lin et al. concluded that separation distance between electrodes directly affected the degree of hysteresis exhibited, due to a larger den-

sity of trapped charges contributing to displacement current. The effect of voltage scan rate is considered in the model as $\frac{dV}{dt}$, and its relative effect on hysteresis is experimentally confirmed in this analysis; illustrated in Figure A.2(b). The fastest measured scan rate (71.42 mV/s) exhibited the greatest oscillatory behavior, which is an indication of a significant density of interface trap states. Carrier trapping and detrapping within the organic layer has been known to create large time constants for measured current to reach equilibrium, and these trap states are unable to unfill trap charges rapidly enough in relation to the scan rate of the voltage sweep (Ambrico *et al.*, 2010; Schroder, 2015). Another indicator of interface trap charges is from a shifted capacitance-voltage (C-V) profile (A.3), which distorts and transforms due to the contribution of the interface trap capacitance (Schroder, 2015). Finally, a larger hysteresis loop is observed with larger voltage amplitude, which is illustrated in in Figure A.2(c), and is considered in the voltage (V) term from equation (A.1). Under the displacement current model, space charge accumulation at the metal/polymer interface is prevalent, thereby screening the electric field and limiting carrier injection. These observations are in agreement with prior studies indicating that the density of stored charges is a function of the amplitude of the voltage applied, as higher potential differences allow deeper interface states to become occupied (Majumdar *et al.*, 2002). Thus, the combination of these controlled factors confirm the general behavior of the displacement current model, in which larger charge accumulation area, with deeper trap states and less mobile trap charges increases the level of hysteresis observed.

A limitation of the displacement current model is the lack of specificity regarding illumination. In this study, increased hysteresis was observed under illumination, relative to dark conditions, with both broadband white light and monochromatic UV irradiation, as illustrated in Figure A.4(a) for Al top electrode and Figure A.4(b) for Au top electrode on conductive PEDOT:PSS devices. While other studies note

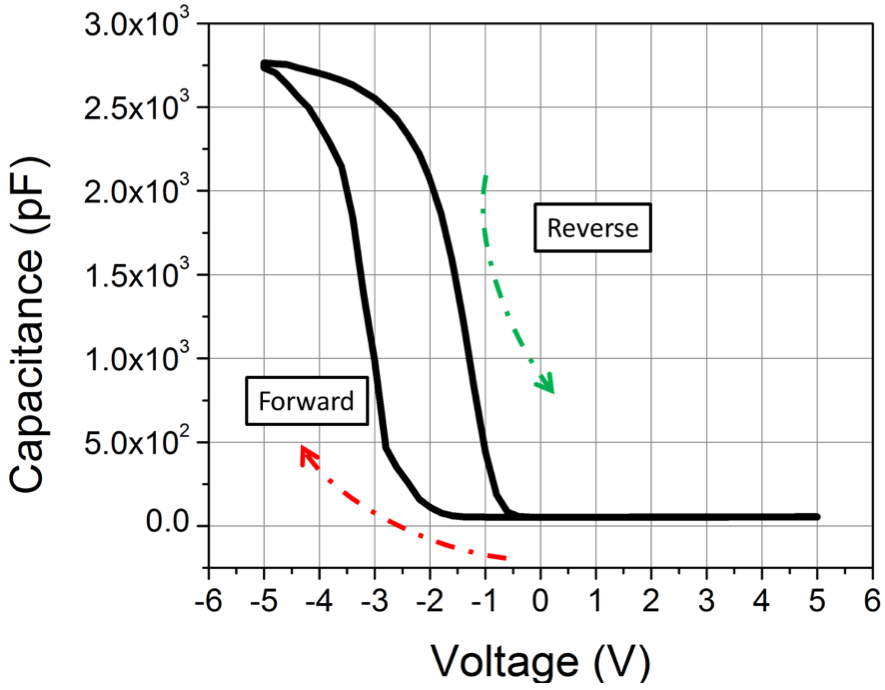

Figure A.3: Shifted Capacitance-Voltage measurements of devices (Non-Conductive PEDOT:PSS, Au electrode, ITO Substrate)

that UV treatment of PEDOT:PSS decreased the number of charge trapping defects and increased conductivity of the PEDOT:PSS Chin *et al.* (2010), the magnetude of displacement current, in this work, is found to amplify with illumination. A marker for the reduced density of trap states manifests when comparing differential resistance under illumination, in which the devices exhibited strong oscillatory characteristics when measured in the dark, but this behavior is suppressed under UV illumination (A.5). Reduced oscillations may reconcile why devices had greater conductivity and stability post-illumination.

The hysteresis effect from space charge storage and traps states is found to persist over two years of storage in air (A.6) as I-V characteristics exhibit reduced conductivity, in addition to increased oscillatory behavior. Over time, ambient moisture chemically binds to PEDOT:PSS, increasing the density of trap states Moujoud *et al.* (2009, 2010). Despite the dormant chemical modification of PEDOT:PSS, illumina-

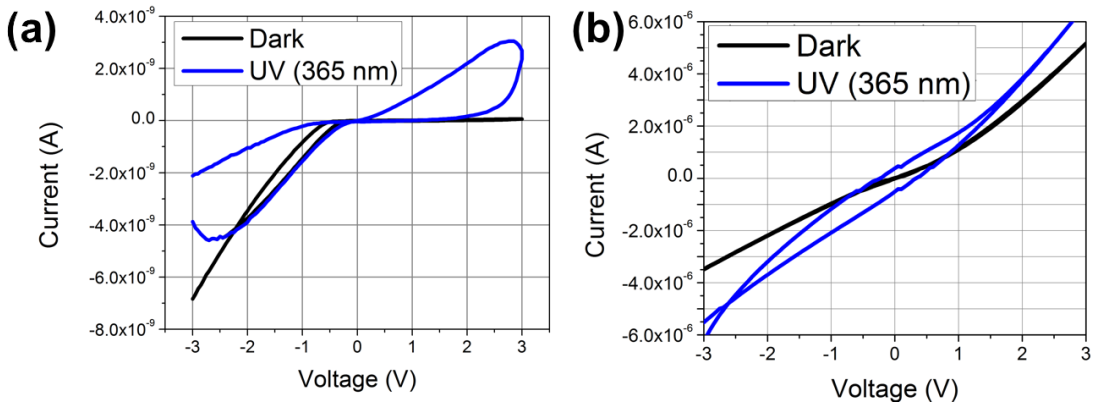

Figure A.4: Current-Voltage Measurements of PEDOT:PSS device as a function of illumination for (a) Al and (b) Au contacts

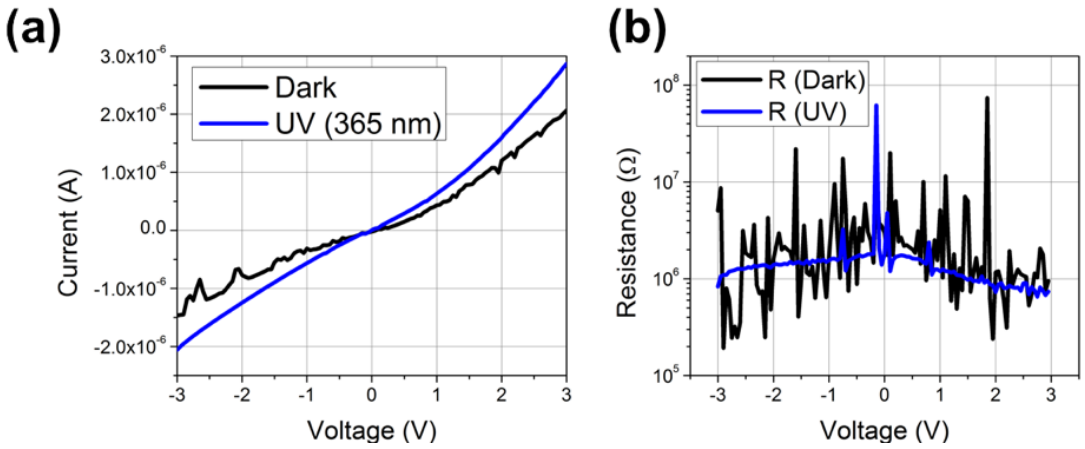

Figure A.5: (a) Current-Voltage characteristics and (b) Differential Resistance of device (Conductive PEDOT:PSS, Au electrode, Si Substrate) illustrating degree of oscillatory behavior indicating reduced trap states with illumination

tion is still found to produce a net increase in measured hysteresis, suggesting that charge accumulation along the ZnO/PEDOT:PSS interface and into the space charge region dominates over reduced trap states in the PEDOT:PSS layer alone (Ambrico *et al.*, 2010).

A.4.2 Descriptive Analysis and Modeling

A series of first order multiple linear regression (MLR) models were generated to decouple the relationship between numerical markers for hysteresis and their underly-

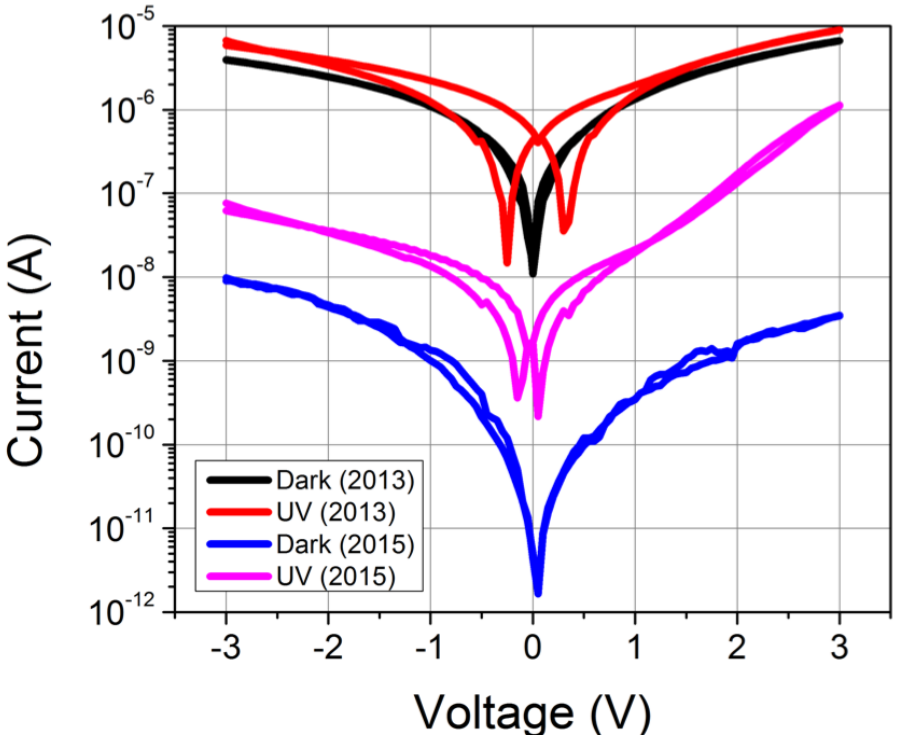

Figure A.6: Degradation of PEDOT:PSS device conductivity for dark and illuminated test conditions over time. Note increased hysteresis behavior and reduced oscillatory behavior with UV illumination.

ing relative underlying causes stemming from device processing and characterization considerations. Due to its fairly anomalous behavior, which has been attributed to several factors including polarized and mobile ions (Richardson *et al.*, 2016; Meloni *et al.*, 2016), a theoretical model that perfectly describes I-V hysteresis across organic polymers is highly impracticable, especially if derived from Fermi-Dirac statistics for solid-state semiconductors. This analysis, instead uses an empirical parametric least squares approach toward estimating first-order response (magnitude and sign) from the set of probable factors that contribute to hysteresis. While hysteretical responses would be expected to locally optimize, as uncovered through Response Surface Methodologies (RSM), axial (face-centered) experimental points were not considered in this study, lending less statistical power to model specifications including interaction and higher order terms. A simplistic first order linear specification is reported

due to the constrained nature of the experimental exploration space—predominately due to the range of device sizes available during fabrication. As determined through experimental screening, stepwise model selection, and model refinement, the factors of *Device Area* and *Illumination* accounted for most of the variation of the hysteresis loop parameters (see Supporting Information). Additionally, all other explanatory variables in each model were treated as categorical (with an unambiguous evolution in hysteresis response from each categorical level). The estimators for each set of model parameters are tabulated, and the results are visualized for each numerical hysteresis response marker, along with an overlayed 95% confidence interval.

Current and Voltage Axis Intercepts

The short circuit current (I_{sc}, graphically defined as the intercept along the current axis) and open circuit voltage (V_{oc}, graphically defined as the intercept along the voltage axis) were tabulated and modeled for both forward and reverse I-V sweeps. Included in this model are device subsets composed of non-conductive PEDOT:PSS with Al and Au contacts (Note: all other characterized subsets intercepted the origin and therefore did not exhibit an appreciable I_{sc}). These results are summarized throughout Figure A.7.

The variation of I_{sc} is illustrated in Figure A.7 (a) for forward (I_{sc+}) and (b) for reverse (I_{sc-}) I-V traces. As previously noted, the magnitude of I_{sc} predominately increases as a function of contact size and illumination. For a conventional diodic solar cell, the total current is expressed as a linear combination of drift/diffusion transport, displacement current, and an illumination current (I_L), as shown in equation (A.2) and (A.3), and each component is a strong function of device area (Sze and Ng, 2006).

$$I = I_s[exp(\frac{qV}{kT}) - 1] + (V\frac{dC}{dt} + C\frac{dV}{dt}) - I_L \tag{A.2}$$

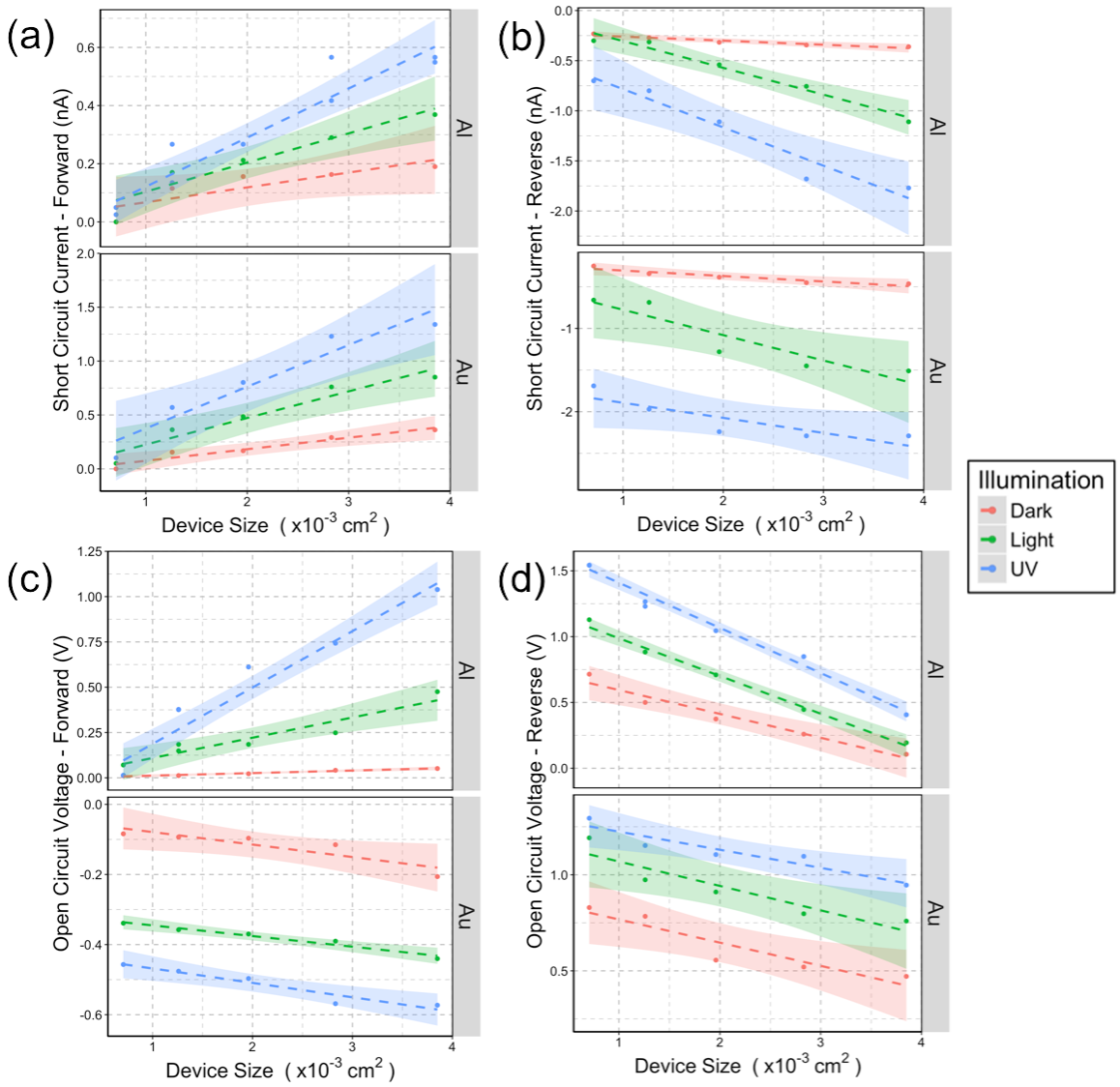

Figure A.7: Short Circuit Current (I_{sc}) for (a) forward and (b) reverse traces and Open Circuit Voltage (V_{oc}) for (c) forward and (d) reverse traces as a function of device size, illumination, and contact electrode

where illuminated current is:

$$I_L = Aq \int_{h\nu=E_g}^{\infty} \frac{\mathrm{d}\Phi}{\mathrm{d}h\nu}\,\mathrm{d}h\nu \tag{A.3}$$

However, absent of illumination, this increase is less pronounced, suggesting that the variability of I_{sc} is a stronger function of I_L and I_d interacting, rather than to I_d alone. Broad band white light illumination consistently results in less short circuit

current than UV illumination, because as noted in equation (A.3), the integral of total incident light flux only considers wavelengths greater than the band edge energy of ZnO. Illumination at $h\nu \geq E_{g(ZnO)}$ is a stronger driver for I_{sc} precisely because photo-generated carriers inject into the organic layer, and occupy trap states before able to sweep across the depletion region. As a result, carriers accumulate at the metal-polymer interface, shifting the total current away from equilibrium (dark) levels.

A summary of extracted open circuit voltages are presented in Figure A.7 (c) for forward (V_{oc+}) and (d) reverse (V_{oc-}) traces, subsetted by contact electrode. In all cases, the effect of illumination (progressing from dark, to white light, to UV) increases the magnitude of the V_{oc} measured. However, the direction of voltage sweep in correspondence with the device size and metal work function, affects whether the magnitude of V_{oc} increases or decreases. With Au, the magnitude of V_{oc+} increases (becomes more negative) with increasing device size, however, in the reverse case, V_{oc-} decreases, corresponding to a left-shift of the hysteresis loops. For Al, the opposite effect is observed: with increasing device sizes, the forward trace (V_{oc+}) is observed to increase while the reverse trace (V_{oc-}) decreases; and the net transformation is a right-shift in the hysteresis profile. Assuming a metal-semiconductor interface in which thermionic emission dominates, the effect of superposition from illumination can be described as (Sze and Ng, 2006; Fonash, 2010):

$$V_{oc} = \phi_B + \frac{kT}{q} ln(\frac{J_{sc}}{A^* T^2}) \approx \phi_B + \frac{kT}{q} ln(\frac{I_L}{I_s}) = \phi_B + \frac{kT}{q}[ln(I_L) - ln(I_s)] \qquad (A.4)$$

From equation (A.4) V_{oc} is both a function of the Schottky barrier height (ϕ_B), and saturation current (I_s). Despite similar Schottky barrier heights, the negative dipole from the PEDOT:PSS surface, in tandem with Al (anodic index $\approx$ 0.9 V) having a dissimilar nobility to that of Au (anodic index $\approx$ 0 V), modifies the ratio of I_L to I_s. Thus, the difference between saturation and illuminated current, stemming from the

relative positions of the top metal electrodes along the Galvanic series, reverses the coordination of V_{oc} shift (Ya-Bin *et al.*, 2011; Nakano *et al.*, 2007).

The empirical MLR model describing the relationship of each directional intercept is shown in equation (A.5) with model estimator coefficients in Table A.1 (Note: *Contact* and *Illumination* are treated as dummy variables referenced to *Al* and *Dark* levels, respectively).

$$\left.\begin{array}{l} I_{sc}+ \\ \\ I_{sc}- \\ \\ V_{oc}+ \\ \\ V_{oc}- \end{array}\right\} = \beta_0+\beta_1\times Contact(Au)+\beta_2\times Illum.(Light)+\beta_3\times Illum.(UV)+\beta_4\times DeviceSize \tag{A.5}$$

Current and Voltage Intersection

The point of intersection between forward and reverse sweeps was extracted for all PEDOT:PSS devices that exhibited pinched hysteresis. Ideally, this intersection should occur at the origin, however a subset of devices (Si substrate, non-conducting PEDOT:PSS, and Au top contact) exhibited shifted intersection voltage and intersection current. These results are illustrated in Figure A.8, and the model describing the intersection behavior are presented equation (A.6) with model estimator coefficients in Table A.2.

$$\left.\begin{array}{l} I_{intersection} \\ \\ V_{intersection} \end{array}\right\} = \beta_0+\beta_1\times Illum.(Light)+\beta_2\times Illum.(UV)+\beta_3\times DeviceSize \tag{A.6}$$

Response	$\hat{\beta}_0$	$\hat{\beta}_1$	$\hat{\beta}_2$	$\hat{\beta}_3$	$\hat{\beta}_4$
$I_{sc}+$	-3.645 $\times 10^{-10}$ *** (8.064 $\times 10^{-11}$)	3.019 $\times 10^{-10}$ *** (5.852 $\times 10^{-11}$)	2.058 $\times 10^{-10}$ ** (7.482 $\times 10^{-11}$)	3.673 $\times 10^{-10}$ *** (7.054 $\times 10^{-11}$)	1.761 $\times 10^{-7}$ *** (2.515 $\times 10^{-8}$)
$I_{sc}-$	3.416 $\times 10^{-10}$ * (1.294 $\times 10^{-10}$)	-4.901 $\times 10^{-10}$ *** (9.391 $\times 10^{-11}$)	-5.188 $\times 10^{-10}$ *** (1.150 $\times 10^{-10}$)	-1.312 $\times 10^{-9}$ *** (1.150 $\times 10^{-10}$)	-2.067 $\times 10^{-7}$ *** (4.197 $\times 10^{-8}$)
$V_{oc}+$	0.06626 (0.12584)	-0.63629 *** (0.09132)	-0.02882 (0.11676)	0.10762 (0.11008)	97.22499 * (39.24511)
$V_{oc}-$	0.88797 *** (0.06609)	0.18099 *** (0.04796)	0.28652 *** (0.06132)	0.58511 *** (0.05781)	-220.13372 *** (20.61129)

Table A.1: Model estimators of current and voltage intercepts for reverse and forward traces. Standard error of the coefficient reported in parenthesis below coefficient. Note: asterisks after the coefficients indicates the level of statistical significance as follows: *** indicates the coefficient is statistically different from zero at the 1% level, ** at the 5% level, and * at the 10% level.

Both intersection current and intersection voltage increase for each illumination level, but intersection voltage decreases and intersection current increases with device size, respectively. Previous exploration of non-zero intersection behavior has been linked an interaction of distinct memory effects (namely memristive, memcapacitive, and meminductive) to the quadrant in which the intersection occurs (Di Ventra and Pershin, 2011; Qingjiang *et al.*, 2014). Because non-conductive PEDOT:PSS has a greater density of trap states, the memcapacitance effect will be more pronounced for greater device area. Here, the competing reduction of the intersection voltage, with an increasing intersection current lead to an overall increase of deviation from the origin (0 V, 0 A). Shifting into the first quadrant indicates that a stronger memcapacitance effect will be expressed with increasing device area and illumination levels.

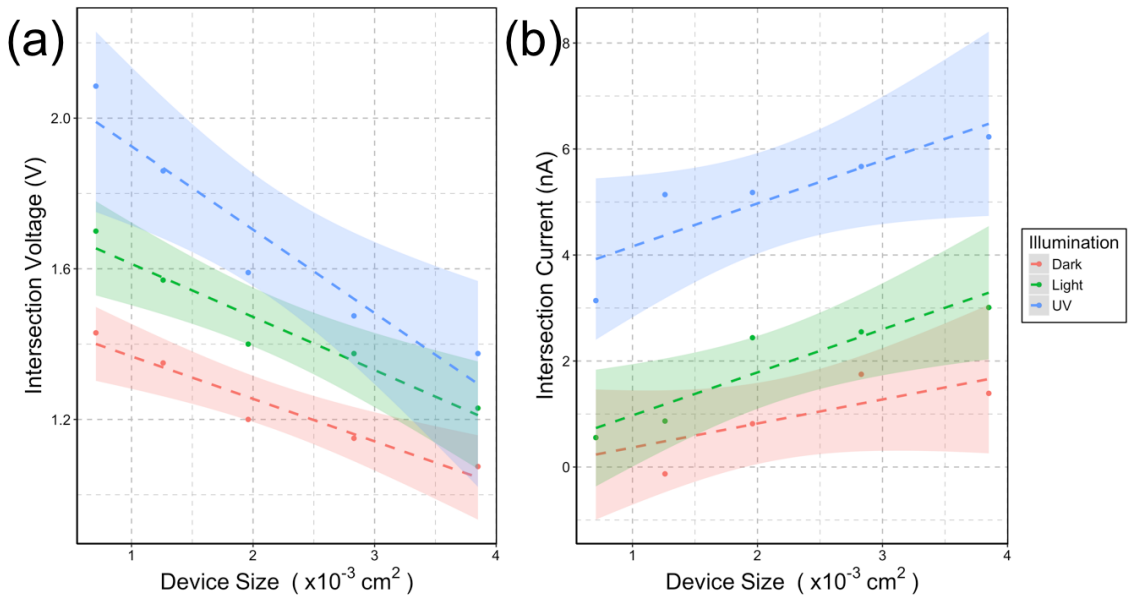

Figure A.8: Intersection (a) voltage and (b) current between forward and reverse traces as a function of illumination and device size

Loop Area

The total loop area represents an extraction of the area between forward and reverse traces of the I-V measurements. Figure A.9 shows the extracted loop areas for devices on (a) Si and (b) ITO, subsetted by metal electrode and PEDOT:PSS conductivity. The MLR model describing the total loop area is expressed in equation (A.7) with model estimator coefficients enumerated in Table A.3.

$$TotalArea = \beta_0 + \beta_1 \times Substrate(Si) + \beta_2 \times Grade(NC) + \beta_3 \times Contact(Au) + \beta_4 \times Illum.(Light) + \beta_5 \times Illum.(UV) + \beta_6 \times DeviceSize \tag{A.7}$$

In most cases the total loop area increases for every increase in device area, and with each progressive illumination level. The exceptions to this include conductive PEDOT:PSS with a Si substrate and Au top electrodes, as well as ITO substrates with Al top electrodes. In the case of the former, hysteresis is suppressed with increasing device size, and in the case of the latter, it is suppressed with increasing illumination

levels. For the first exception, a cathodic material over heavily doped n-type Si, as well as larger device area, increases conduction paths for carriers through the conductive PEDOT:PSS medium, thereby increasing the rate at which carriers can de-trap. The second exception is found for Al on ITO, in which the combination of an anodic contact over a p-type substrate reduces hysteresis in current traces, as carriers photo-generate from the ZnO layer. Both phenomena have the net effect of suppressing hysteresis, thereby reducing the total area measured within the I-V loops.

A.5 Conclusion

In this work exploratory analysis and numerical modeling of hysteresis behavior in current-voltage characteristics of PEDOT:PSS films have been investigated. Several device processing parameters and characterization conditions have been confirmed to affect I-V hysteresis, and these factors were assessed in terms of displacement current theory. A comprehensive series of specified parametric MLR empirical models describing the scale and direction of hysteresis profile transformation (e.g. loop

Response	$\hat{\beta}_0$	$\hat{\beta}_1$	$\hat{\beta}_2$	$\hat{\beta}_3$
$I_{intersection}$	-5.926 $\times 10^{-10}$	1.008 $\times 10^{-9}$	4.195 $\times 10^{-9}$	6.926 $\times 10^{-7}$
		*	***	***
	(3.691 $\times 10^{-10}$)	(3.520 $\times 10^{-10}$)	(3.520 $\times 10^{-10}$)	(1.284 $\times 10^{-7}$)
$V_{intersection}$	1.57703	0.214	0.436	-158.40232
	***	**	***	***
	(0.05891)	(0.05619)	(0.05619)	(20.50364)

Table A.2: Model estimators for intersection points between reverse and forward traces. Standard error of the coefficient reported in parenthesis below coefficient. Note: asterisks after the coefficients indicates the level of statistical significance as follows: *** indicates the coefficient is statistically different from zero at the 1% level, ** at the 5% level, and * at the 10% level.

Estimator	Coefficient
$\hat{\beta}_0$	5.833×10^{-5} ** (2.228×10^{-5})
$\hat{\beta}_1$	-1.547×10^{-4} *** (1.464×10^{-5})
$\hat{\beta}_2$	6.721×10^{-5} *** (1.464×10^{-5})
$\hat{\beta}_3$	-1.093×10^{-5} (1.462×10^{-5})
$\hat{\beta}_4$	2.706×10^{-5} (1.780×10^{-5})
$\hat{\beta}_5$	6.565×10^{-5} *** (1.803×10^{-5})
$\hat{\beta}_6$	1.566×10^{-2} * (6.532×10^{-3})

Table A.3: Model estimators for Total Hysteresis Loop Area. Standard error of the coefficient reported in parenthesis below coefficient. Note: asterisks after the coefficients indicates the level of statistical significance as follows: *** indicates the coefficient is statistically different from zero at the 1% level, ** at the 5% level, and * at the 10% level.

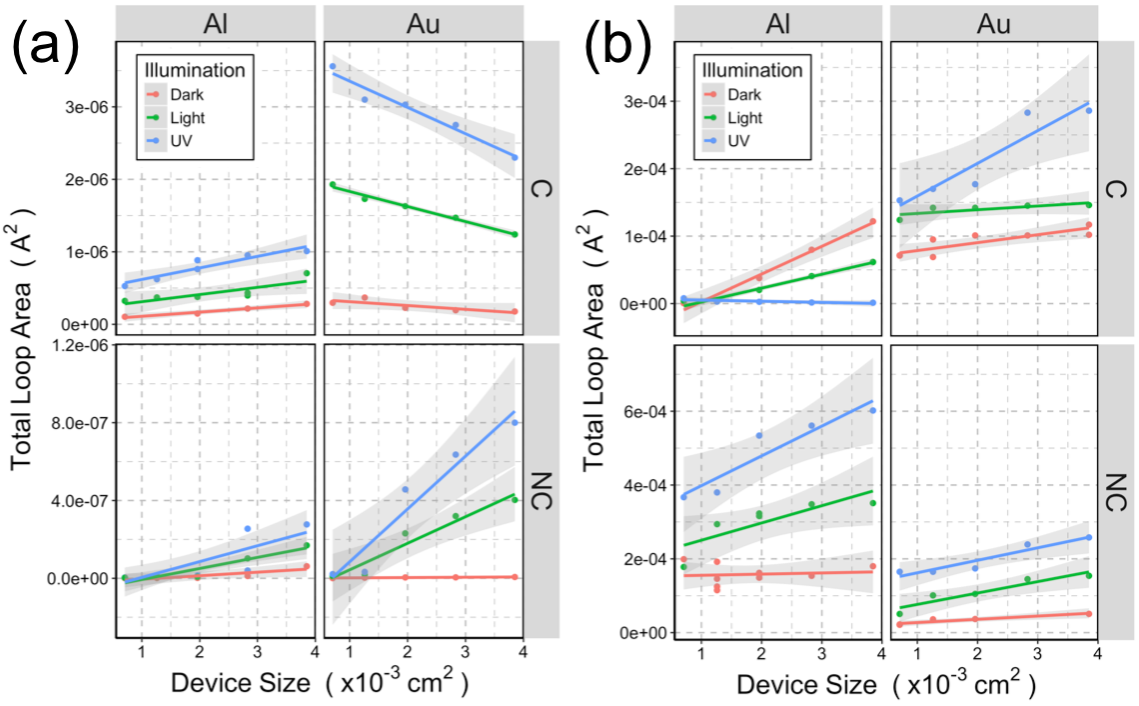

Figure A.9: Loop Area between forward and reverse traces for (a) Si and (b) ITO substrates as a function of device size and illumination, subsetted by contact metal and PEDOT:PSS conductivity. (Note: C and NC refer to conductive and non-conductive PEDOT:PSS respectively)

area and functional shifting) have been generated and analyzed. With an extended experimental exploration space, processing parameters could conceivably be investigated to minimize hysteretical response as a design objective. Evaluated in terms of fundamental electronic transport, these models provide a predictive framework for estimating general transformations of hysteresis behavior from the I-V characteristics of hybrid organic/inorganic semiconducting polymers. This work represents a principle undertaking in developing hysteresis mitigation objectives through a deeper understanding of how the studied processing and characterization factors interact to form the resultant hysteresis.

APPENDIX B

ZNO NANOWIRE BASED VISIBLE-TRANSPARENT ULTRAVIOLET DETECTORS ON POLYMER SUBSTRATES

B.1 Abstract

The fabrication and characterization of fully visible-transparent and flexible ultraviolet (UV) detectors, on polyethylene 2,6-naphthalate (PEN) with active channels of zinc oxide (ZnO) nanowires and ohmic indium tin oxide (ITO) contacts, are reported and discussed. The fabricated detector has an average transmittance of 80% in the visible spectral range and is most responsive at or below 370 nm, the onset of UV light, with a UV/vis rejection ratio of 1.42×10^3. A five orders of magnitude difference in the photocurrent, between UV illumination and dark conditions, is also observed. The single-sided UV response further shows that the PEN substrate performs well as a UV reflector. The noise analysis on the nanowire UV detector indicates a noise equivalent power (NEP) and detectivity (D^*) of 5.88×10^{-13} $WHz^{-0.5}$ and $2.13 \times 10^9 cmHz^{0.5}W^{-1}$, respectively.

B.2 Introduction

In recent years, research effort in the field of flexible and transparent electronics has demonstrated the potential to completely revolutionize consumer products (Javey, 2006; Rogers *et al.*, 2010). Unlike the trend in microelectronics, where scaling and performance are the driving force, flexible electronics offer the unique possibility to create integrated devices with multiple functionalities and form factors including implantable, conformable, and multilayer designs with visible transparency. Wide

bandgap UV detectors, especially those based on Zinc Oxide (ZnO), have gained particular momentum (Soci *et al.*, 2007; Peng *et al.*, 2010; Das *et al.*, 2010; Law and Thong, 2006) due to the ease of fabrication on both rigid and opaque substrates. Most recently, a flexible UV detector based on ZnO thin film has been reported (Ji *et al.*, 2010), however no report exists of a visible-transparent, nanowire (NW)-based UV detector on a transparent substrate with both transparent active material and transparent contact material. An "all-visible" transparent UV detector, as described below, would enable novel applications including the potential to be attached to windows, or atop other devices which require full exposure to visible light. These devices will eventually further the goals of transparent thin-film electronics, but for now can be used to control automated blinds on smart-windows and support UV photovoltaics. Zinc Oxide has been explored as an active material for UV detectors because of its large band gap that falls in the UV spectral range (370 nm or 3.3 eV). Furthermore, ZnO NWs grown from a high temperature process are found to be transparent and mechanically flexible (Zhou *et al.*, 2008), and their one dimensional formation lend themselves to reduced linear or planar structural defects (Martensson *et al.*, 2004). Additionally, the likelihood of unwanted trap-state emissions, most notoriously the green band from ZnO thin films and solution-grown ZnO NWs (Ozgur *et al.*, 2005; Unalan *et al.*, 2008; Kohan *et al.*, 2000; Liu *et al.*, 2004; Vanheusden *et al.*, 1996), is reduced. Therefore, these high-quality NWs were used to fabricate fully transparent and flexible UV detector devices on polyethylene 2,6-naphthalate (PEN) substrates with indium tin oxide (ITO) contacts. The PEN polymer is chosen for its improved resistance to oxidation and its ability to withstand temperatures; higher than comparable polymers such as polyethylene terephthalate (PET) and polytrimethylene terephthalate (PTT) (Mackintosh and Liggat, 2004). Furthermore, PEN has the unique property of exhibiting very low transmittance for shorter UV wavelengths,

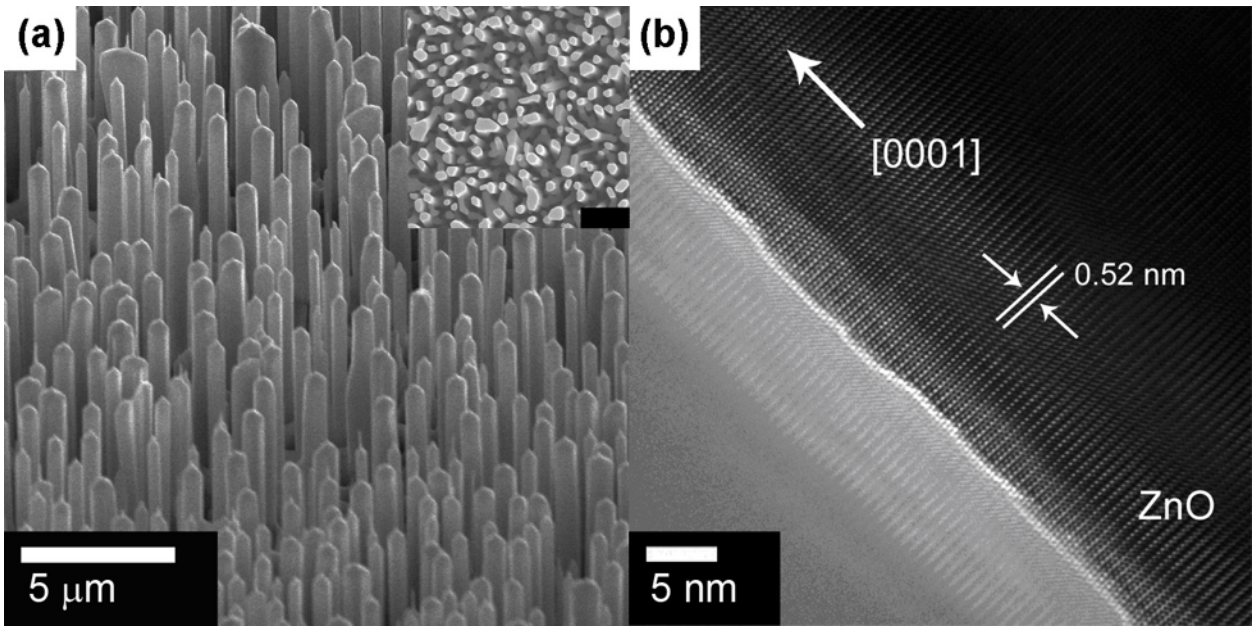

Figure B.1: (a) Scanning electron micrograph of ZnO NWs grown in vertical array (inset: top view–scale bar 1 μm) and (b) high resolution transmission electron micrograph of ZnO NW indicating highly ordered single crystal structure.

specifically below 383 nm in comparison to 313 nm for PET (Scheirs and Long, 2005). This makes PEN a suitable candidate for single-sided detection, with high transmittance in the visible range and high rejection in a wider UV range.

B.3 Experimental Details

In this study, the NWs were grown by a typical high temperature Vapor-Liquid-Solid (VLS) process (Greene *et al.*, 2005). Zinc oxide, in high purity powder form, was mixed with graphite in a 1:1 molar ratio and placed at the center of a tube furnace (930 °C). Silicon (100) substrates, with sputtered ZnO thin film (20-30 nm), were placed along the tube at the 700 °C growth zone. The flow rates of 110 sccm for argon and 3 sccm for oxygen were maintained at a steady state pressure of 150 Torr.

The Field Emission Scanning Electron Micrograph (FESEM), shown in Figure B.1(a), exhibits an array of vertically aligned NWs about 3-10 microns in length with hexagonal ends that are about 200 nm in diameter. Figure B.1(b) is the high

resolution transmission electron micrograph (HRTEM) of a NW; a well ordered single-crystal material free of line defects, with d_{0001} of 0.52 nm are observed. The absence of deep level defects are further supported by room temperature (295 K) photoluminescence (PL) data, collected with a HeCd laser (325 nm line), in Figure B.2. A strong emission due to the band edge transition, with a full width at half maximum (FWHM) of 18 nm, and the absence of dominant broad band peaks in the visible spectral range are clear. The inset in Figure B.2, from low temperature PL (12 K), demonstrates a focused narrow band edge emission peak at approximately 369 nm.

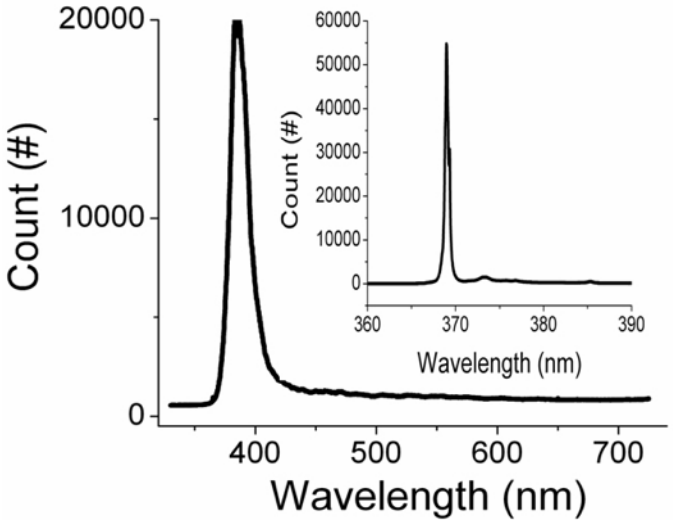

Figure B.2: Room temperature photoluminescence (PL) of ZnO NW indicating band edge energy peak and the lack of broad band peaks is attributed to high temperature growth (inset: low temperature PL).

The NWs were transferred onto the PEN substrate using a mechanical slide setup (Fan *et al.*, 2008). The contacts were photolithographically pattered on each end of the NWs and an ITO blanket was deposited using an electron-beam evaporator. The as-deposited ITO is low density, amorphous, and opaque, but after post-liftoff heat treatment (Han *et al.*, 2006) in oxygen, which was optimized to 150 °C for 6 hours, the ITO progressively became more transparent as shown in the device of Figure B.3(a).

B.4 Results and Discussion

The current-voltage characteristics of the two-terminal metal-semiconductor-metal (i.e., ITO-ZnO-ITO) UV detector device are illustrated in Figures B.3(b) and B.3(c). When illuminated with an UV lamp at 365 nm wavelength and power density of 48 mW/cm^2, the current response at 3 V bias demonstrates a low dark current level of 2 $\times$ 10^{-11} A and a high photoconducting current of 6 $\times$ 10^{-6} A. The highly linear trace at low bias indicates good ohmic behavior due to the ZnO-annealed ITO contact. Note, annealing the ITO electrodes resulted in the crystallization and densification, which resulted in the sharp drop in resistivity due to increased mobility (Steckl and Mohammed, 1980). An 80% transmittance was produced by the annealed ITO contacts, and from four-point probe measurements, a resistivity of 2.85 $\times$ 10^{-4} Ω-cm was determined. Furthermore, as noted in the logarithmic plot, the photocurrent increases by about 5 orders of magnitude when the single-NW device is illuminated. Note, at least 20 devices were tested in this manner with most exhibiting comparable characteristics. In relation to similar ZnO UV detectors, the result of this work is superior to reported ratios of illuminated to dark currents (Soci *et al.*, 2007; Peng *et al.*, 2010; Ji *et al.*, 2010).

The spectral photoresponse of the device was determined using a grating monocromator setup (Newport QE/IPCE) that measured the photocurrent at wavelengths from 300 nm to 700 nm. The ZnO UV detector was operated in air at a bias of 1.5 V, applied through a load matching resistor (100 kΩ) and the photocurrent signal (I_{ph}) was measured with a lock-in amplifier. In addition, a reference photocurrent (I_{ref}) was also measured using a detector of known responsivity (R_{ref}). The wavelength dependence of the photoresponse ($\frac{I_{ph}}{I_{ref}}$ x R_{ref}) is shown in Figure B.4. Note, within the 360-380 nm range, which parallels the FWHM of the PL data, there is a sharp

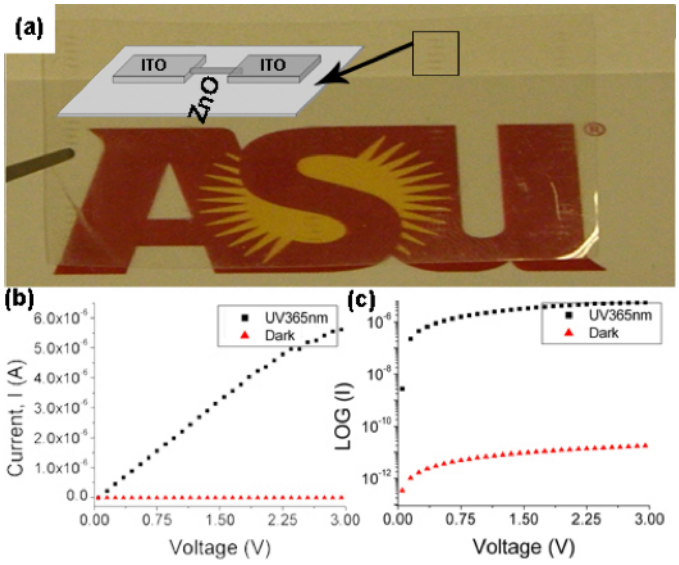

Figure B.3: (a) Fully fabricated visible transparent UV detector after heat treatment (inset: Schematic of nanowire device) (b) IV characteristics under 356 nm UV illumination (black square) and dark conditions (red triangle), Linear plot and (c) Logarithmic plot. Note, the differential resistance of the dark current is found from the inverse slope of the IV characteristics in (b) and is determined to be $1.59\times10^{11}\Omega$

attenuation in the photoresponse. This result further suggests that the fabricated device performs well as a UV-only detector, as opposed to exhibiting absorption from impurity levels in the visible range that are typical of low-temperature, solution-grown ZnO NW detectors. Additionally, the rejection ratio of UV to visible light, defined as the ratio of the responsivities at 360 nm and 410 nm, is 1.42×10^3 for this fully visible-transparent UV detector.

Figure B.5a illustrates the novel functionality, enabled by the transparent substrate, in which both the front and back (or reverse) side I-V characteristics of the NW device on PEN can be determined. The schematic for the test setup is shown in the right inset and the results indicate that although PEN is transparent in the visible range, exhibiting an illuminated current level of 56 mA at 1.5 V from the front side, a significantly reduced performance (0.298 mA) from reverse-side illumination occurs due to cutoff transmission wavelength of PEN in the lower energy UV range.

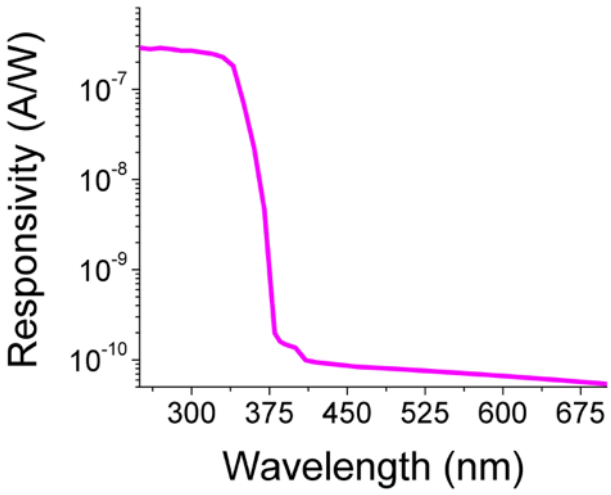

Figure B.4: Measured spectral responsivity of ZnO NW detector at 1.5V bias. Note, the responsivity at the cutoff wavelength of 360 nm is 2.98×10^{-7} A/W.

A plot of the device's response to the dark condition is plotted for comparison. Thus, the magnitude of reduced current from reverse-side illumination may be attributed to the reduced transmittance of PEN; specifically, a reduction in transmittance of three orders of magnitude results in three orders of magnitude difference in the current level between the front and reverse side illuminations.

The photoconductive gain (G) is an important performance metric used to characterize photodetectors. It is defined as the ratio of the number of electrons collected to the number of photons absorbed per unit time as follows:

$$G = \frac{N_{e^-}}{N_{ph}} = \frac{\frac{I_p h}{e}}{\frac{P}{h\nu}} \tag{B.1}$$

where I_{ph} is the photocurrent at the operating voltage, P is the total power impinging on the wire, h is the bandgap energy of ZnO, and e is the electronic charge. By geometrically modeling the NW as a cylinder that is exposed on one half, assuming a NW length of 5 μm and a diameter of 200 nm and with an external light power density of 48 mW/cm^2, the photoconductive gain at 3 V was calculated to be 4 $\times$

10^5. Note, the value of G is quite comparable with other reports at this specified operating level (Soci *et al.*, 2007); the considerable gain being largely attributed to (a) reduced electron transit time due to the miniaturized dimensions of the active NW channel, and (b) the long carrier lifetime brought upon by ZnO NW surface as explained below (Soci *et al.*, 2007).

The use of ZnO NWs for UV detection was reported by Soci et. al. and the mechanism for photoconductive gain has been attributed to the high density of surface trap states; the high surface-to-volume ratio make these trap states a dominant factor. The trap states apparently stem from adsorbed oxygen molecules that capture free electrons under no illumination or illumination with sub-band gap energy of ZnO. The consequent formation of an interface depletion layer with low surface conductivity leads to the suppressed conductivity under dark conditions. Under UV illumination, electrons and holes are created within the ZnO NW. The photogenerated holes readily migrate to the surface to neutralize the charged oxygen molecules. Consequently, the free electrons, with high carrier lifetimes, directly contribute to the high conductivity within the depletion-free NW, and can be efficiently collected at the electrode.

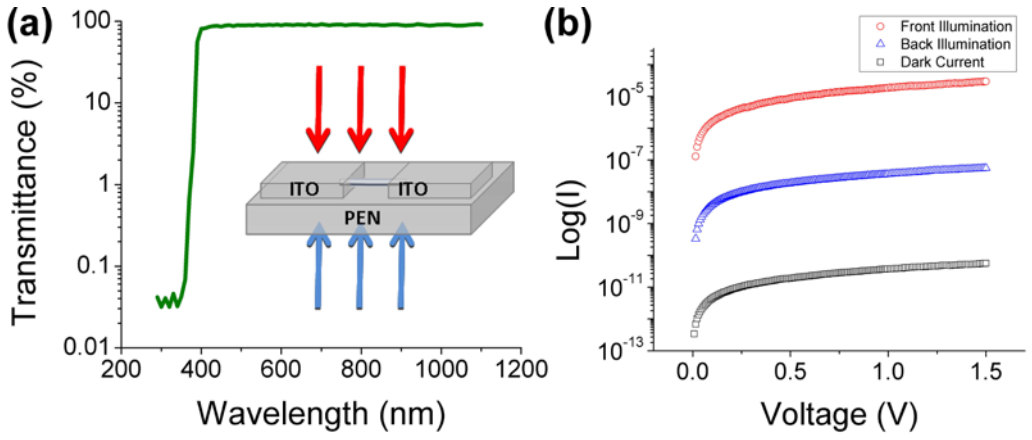

Figure B.5: (a) Transmittance of bare PEN on a logarithmic scale (inset: schematic of test setup for illumination) and (b) Current-Voltage characteristics for front (red arrows on top) and reverse (blue arrows under bottom) side illuminations on device compared to dark conditions.

The fabrication of UV detectors on PEN serves as a good application on a window, for example, when UV detection coupled with the simultaneous blocking of harmful UV energy from transmission needs to take place. Moreover, exploration of other polymer substrates, with shorter cutoff wavelengths, could enable detection on both sides if required. Reports of NW devices fabricated on PET (Zhang *et al.*, 2009) would allow for photodetection of wavelengths at least 70 nm below PEN and devices fabricated on PTT (Zhang *et al.*, 2004) would even permit another 60 nm below PET. The current work on fully visible-transparent application and previous studies on using ZnO NWs for UV detection may enable a variety of innovative design architectures in the future.

Finally, two figure of merits characterizing the noise of the fabricated photodetector, namely the noise equivalent power (NEP) and detectivity (D*), were also analyzed at room temperature. It is widely known that defects in ZnO (i.e., Zn interstitials and O vacancies) give rise to the observed n-type behavior (Banerjee and Chattopadhyay, 2005; Xiang *et al.*, 2007; Cao *et al.*, 2007); the device's dark current is evidence of free electrons. Shot noise is a consequence of the dark current of the nanowire detector, and has a noise magnitude of 5.83×10^{-13} $WHz^{-0.5}$, which exceeds both the Johnson noise (7.66×10^{-14} $WHz^{-0.5}$) and 1/f noise at the measured amplifier bandwidth of 1 kHz. Thus, since the thermally-limited model may not be applicable, NEP and D* are evaluated using the following relations(Jiang *et al.*, 2007): NEP = $(\frac{1}{R_\lambda})$*$(2qI_d+4kT/R_\nu)^{1/2}$ and D* = $(A*f)^{1/2}$, where R_λ is the responsivity at the selected detection wavelength of 360 nm, q is the elementary electronic charge, I_d is the dark current at the detection bias of 1.5 V, R_v is the device differential resistance, k is the Boltzmann constant, and A is the device area, and f is the amplifier bandwidth (Sze and Ng, 2006). Note, R_v and I_d from Figure B.3 are 1.59×10^{11} Ω and 9.42×10^{-12} A, respectively. For an exposed surface area (A) of 1.57×10^{-13} m^2 and

R_λ of 2.98 $\times$ 10^{-7} A/W, the room-temperature NEP is found to be 5.88 $\times$ 10^{-13} $WHz^{-0.5}$ and the corresponding D^* is 2.13 $\times$ 10^9 $cmHz^{0.5}W^{-1}$. The NEP of this work is comparable to thin film UV detectors; this is attributed to the low dark current, which is also an indication of high quality ZnO nanowires. Typically, thin-film ZnO UV detectors exhibit higher D^* compared to NW-based detectors; for unprotected single-nanowire devices, the lower D^* may be attributed to more pronounced carrier trapping and detrapping effects, stemming from a large surface-to-volume ratio, and consequently a much smaller effective device area (Lu *et al.*, 2007). Here, a summary of various literature reports for comparison with the current data is given in Table 1.

B.5 Conclusion

Fully visible-transparent and flexible UV detectors have been fabricated and characterized by using high quality ZnO NWs and ITO electrodes on a PEN substrate. The photoconductive properties on the resultant devices have been thoroughly examined, which indicate a five orders of magnitude difference in the photocurrent difference between UV illumination and dark conditions. In addition, the rejection ratio of the NW devices' responsivity to both the UV and visible spectrum was found to be 1.47 $\times$ 10^3, which is quite large and comparable to related reports. The photocurrent response of the ZnO NW detector to the reverse-side exposure of light was studied and found to be a function of the cutoff transmittance frequency of PEN. Combined with the substantial photoconductive gain (G=4 $\times$ 10^5), the fabricated device performs well as a single-sided and fully visible-transparent UV detector. The noise analysis of the nanowire UV detector indicates a noise equivalent power (NEP) and detectivity (D^*) of 5.88 $\times$ 10^{-13} $WHz^{-0.5}$ and 2.13 $\times$ $10^9 cmHz^{0.5}W^{-1}$, respectively. A comparison of noise parameters, in detectors employing ZnO in various geometries, shows the efficacy and potential of NW based devices.

B.6 Acknowledgments

The authors acknowledge the support of the National Science Foundation-ECCS (0926017), the Arizona State University Center for Solid State Electronic Research (CSSER) for processing facilities, the Center for Solid State Science (CSSS) for NW growth facilities, and the Flexible Display Center (FDC) for use of polymer substrates. We thank Luying Li, Martha McCartney and David Smith for assistance with HRTEM and Christian Poweleit for assistance with PL measurements.

ZnO material	Illuminated/ dark current (@ 3 V)	Rejection ratio (UV/vis)	Photo-conductive gain	NEP ($WHz^{-0.5}$)	Detectivity ($cmHz^{0.5}W^{-1}$)
Nanowire (Soci *et al.*, 2007)	7.5×10^4	4.3×10^1 (air)	2×10^7	NR	NR
Thin film (Ji *et al.*, 2010)	1.61×10^3	1.56×10^3	NR	NR	NR
Nanowire (Lu *et al.*, 2007)	20	10	NR	7.89×10^{-11}	1.9×10^8 @2V
Thin film (Young *et al.*, 2007)	10^4	10^3	NR	3.17×10^{-13}	2.23×10^{12}@1V
Thin film (Jiang *et al.*, 2007)	NR	5×10^5	NR	NR	1.37×10^{11}@3V
Nanowire (this work)	10^5	1.42×10^3	4×10^5	5.88×10^{-13}	2.13×10^9@1.5V

Table B.1: Performance Metrics of ZnO UV Detectors

APPENDIX C

VAPOR-TRANSPORT SYNTHESIS AND ANNEALING STUDY OF $ZN_XMG_{1-X}O$ NANOWIRE ARRAYS FOR SELECTIVE, SOLAR-BLIND UV-C DETECTION

C.1 Abstract

This work uniquely reports the synthesis of $Zn_xMg_{1-x}O$ nanowires and submicron columns by utilizing a traditional carbothermal reduction process toward forming ZnO nanowire ultraviolet detectors, while simultaneously utilizing Mg_3N_2 as the source of Mg. To investigate the relationship between Mg content in the ZnO lattice and the cutoff wavelength for high spectral responsivity, the nanowires were annealed in a series of designed conditions, while chemical, nanostructural, and optoelectronic characteristics were compared before and after treatment. Post-anneal scanning electron micrographs revealed a reduction of the average ensemble nanowire dimensions, which was correlated to the modification of ZnO lattice parameters stemmin from Zn^{2+} dissociation and Mg^{2+} substitution (confirmed via Raman spectroscopy). Analysis of cathodoluminescence spectra revealed a blue-shift of the peak alloy band edge emission along with a red-shift of the ZnO band edge emission; and both were found to be strong functions of annealing temperature. The conversion of Zn_2SiO_4 to Mg_2SiO_4 (in O_2) and $MgSiO_3$ (in Ar), was found to correspond to transformations (shifting and scaling) of high energy luminescence peaks, and was confirmed with XRD analysis. The tunability of the cutoff photodetection wavelength was evaluated as the nanowire arrays exhibited selective absorption by retaining elevated conduction under high-energy UV-C irradiation after thermal treatment, but exhibiting suppressed

conductivity and a single order of magnitude reduction in both spectral responsivity (R_λ) and photoconductive gain (G) under UV-A illumination. Noise analysis revealed that the variation of detectivity (D^*) depended on the regime of ultraviolet irradiation, and that these variations are related to thermal noise resulting from oxygen-related defects on both nanowire and substrate surfaces. These results suggest a minor design tradeoff between the noise characteristics of thermally treated ZnMgO nanowire array UV detectors and the tunability of their spectral sensitivity.

C.2 Introduction

Ultraviolet, solar-blind communication systems that exploit atmospheric scattering to propagate signals toward a non-line of sight (NLOS) receiver (with ranges on the order of kilometers) have been examined extensively, yet the detectors in these receiver systems have largely been dominated by bulky and costly photomultiplier tubes (PMT) (Chen *et al.*, 2008; El-Shimy and Hranilovic, 2012; Yang *et al.*, 2014). Semiconductor-based deep-UV detectors have consequently become of great interest due to their potential advantages of producing low-cost, low-power-consumption, highly scalable solutions. While ZnO nanowire-based photodetectors have been heavily investigated, this material system only exhibits a cutoff detection corresponding to the band edge energy of ZnO in the UV-A spectrum (3.10-3.94 eV) (Ting Li *et al.*, 2001; Collins *et al.*, 2002; Cui *et al.*, 2016). Substitutional doping of Mg with ZnO, on the other hand, has been described as a means of engineering the bandgap of a ternary $Zn_xMg_{1-x}O$ system as high as a 5.8 eV for solar blind photodetectors (Tang *et al.*, 2010; Liu *et al.*, 2010; Lange *et al.*, 2011; Vanjaria *et al.*, 2016). Although Mg has been reported as a feasible dopant to ZnO (due to the similar ionic radii of Zn^{2+} and Mg^{2+}) (Hwang *et al.*, 2004; Liu *et al.*, 2005), Mg/ZnO alloy systems have also shown to phase segregate for high Mg content (Huso *et al.*, 2007). Thus, the development of reliable

techniques toward synthesizing aligned ZnO nanowires, and appreciably incorporating Mg during synthesis is of great significance. Prior work investigating ZnMgO nanostructures have been reported based on deposition methods, which have ranged from: molecular beam epitaxy (Pietrzyk *et al.*, 2014), metal-organic chemical vapor deposition (Kim *et al.*, 2011; Thierry *et al.*, 2012), pulsed-laser deposition (Polyakov *et al.*, 2009), hydrothermal techniques (Liu *et al.*, 2010; Shimpi *et al.*, 2009), RF magnetron co-sputtering (Kar *et al.*, 2008), and vapor-phase transport (Zhou *et al.*, 2009; Tang *et al.*, 2010; Vanjaria *et al.*, 2016). The vapor-phase transport technique, yields highly crystalline nanostructures and is a relatively straightforward synthesis route, able to encompass equilibrium formation in one step, rather than necessitating *ex-situ* incorporation. Additionally, understanding the changes in optical and physical properties due to post-growth thermal treatment of ZnMgO nanowires is of importance toward tuning the cutoff wavelength for solar-blind photodetectors.

In this study, ZnMgO nanowires and submicron columns were synthesized on Si via two equilibrium processes occurring simultaneously: (1) the carbothermal reduction of ZnO and (2) the incorporation of Mg from dissociated Mg_3N_2, which to the best knowledge of the authors has not been reported. Furthermore, a controlled study varying annealing environment and annealing temperature was conducted, demonstrating an evolution of the chemical, spectral, and optoelectronic properties of the synthesized ZnMgO nanostructures. Assessed both before and after thermal treatments, these modified characteristics were investigated via Field Emission Scanning Electron Microscopy (FESEM), Energy-dispersive X-ray spectroscopy (EDX), X-ray diffraction (XRD), Raman spectroscopy, cathodoluminescence (CL), and current-voltage (I-V) behavior. The structural changes of ZnMgO nanowires manifested as modifications of aspect ratio, while also correlating to modified estimates of Mg incorporation due to each annealing condition. Analysis of spectral responsivity and

Anneal Environment	Anneal Temperature (°C)	2θ Peak (100) Plane	2θ Peak (002) Plane	c (Å)	a (Å)
Control	Control	31.71708287	34.39533709	5.21	3.25
Ar	650	31.86748429	34.40787054	5.21	3.24
Ar	900	31.96775190	34.52067161	5.19	3.23
O_2	650	31.86748429	34.50813816	5.19	3.24
O_2	900	31.99281881	34.62093923	5.18	3.23

Table C.1: Lattice Parameter modification of ZnMgO wires as a function of annealing condition

photoconductive gain between treatment and control groups was conducted under dissimilar ultraviolet regimes to numerically compare the differences within detector performance. By exploiting these controlled reaction kinetics from thermal annealing, enhanced selective filtering of high energy UV-C absorption on the nanowire ensemble is demonstrated, accompanied by suppressed conductivity under UV-A illumination. Additionally, analysis of detector noise characteristics demonstrated that their variation from ultraviolet irradiation was linked to the increase of thermal noise from increased oxygen-related defects, presenting potential performance tradeoffs.

C.3 Experimental Details

ZnMgO nanowires were synthesized using a vapor phase transport method comprised of a carbothermal reduction of ZnO in tandem with the dissociation of Mg_3N_2 as the source of Mg. In a single zone reaction tube furnace, a ceramic boat containing a 1:1 molar ratio mixture of ZnO and graphite powder (total 3 g) was placed upstream to another ceramic boat containing 10 g of Mg_3N_2 powder. Silicon (100) substrates were cleaned in piranha solution (70% H_2SO_4, 30% H_2O_2) and were treated using a buffered oxide etchant (BOE, 2% HF). Subsequently, a thin 10 nm ZnO film

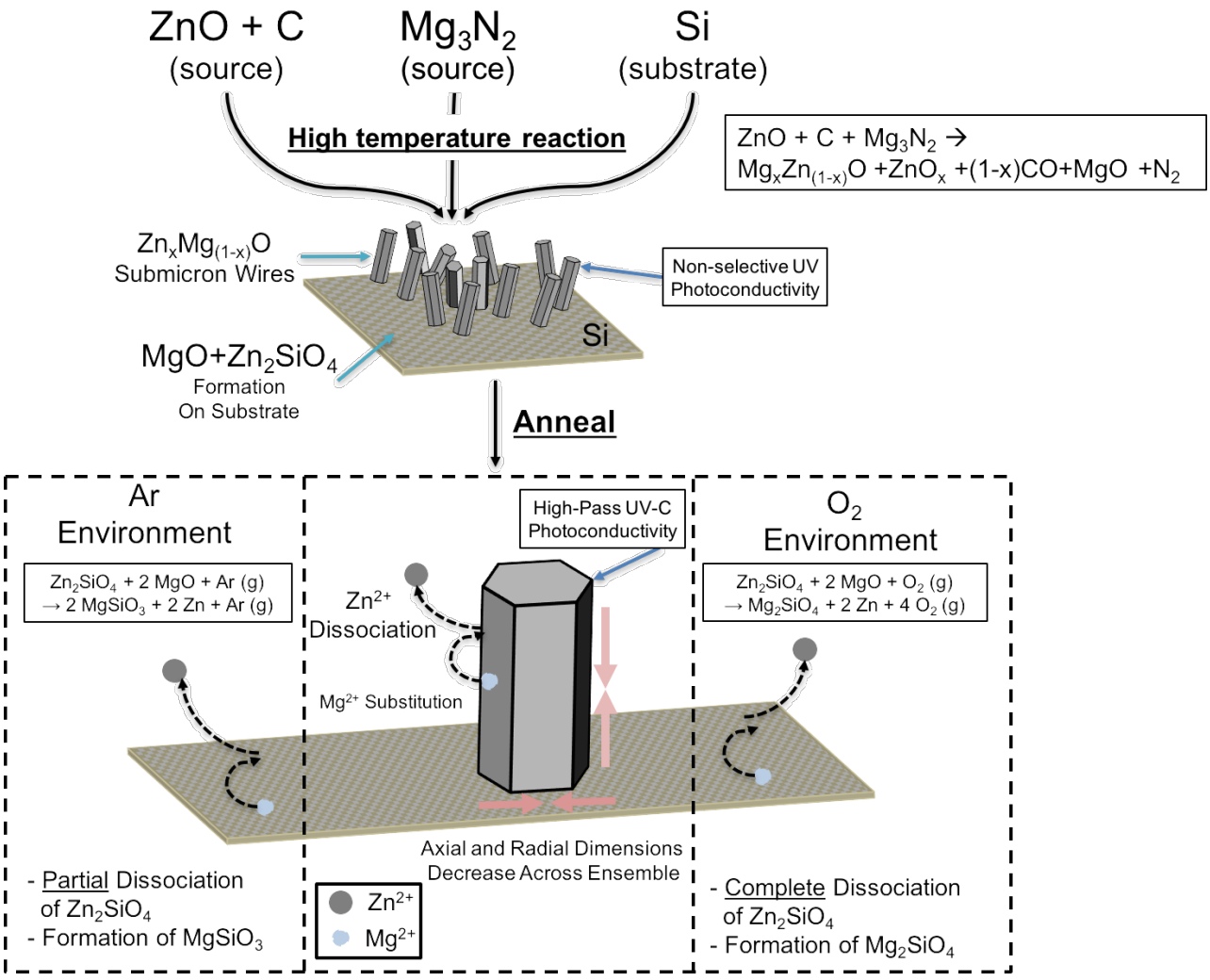

Figure C.1: Schematic of reaction mechanisms forming ZnMgO nanowires, along with structural and chemical modifications from thermal treatment.

was sputtered (Lesker PVD 250) atop substrates to form a catalyst seed. The samples were then cleaned using acetone, isopropanol, and water before being positioned downsteam relative to the source materials. The tube furnace was evacuated and brought to 500 °C. Upon reaching the target temperature, Ar was introduced to the system at a flow rate of 87.4 sccm, while maintaining a steady state pressure of 150 Torr throughout the process. At a rate of 500 °C/hour, the furnace temperature continued increasing up to 1100 °C, upon which the temperature was held for 24 minutes. In the final 10 minutes of this growth period, O_2 was introduced to the system at

a flow rate of 7.5 sccm. Finally, the system was allowed to cool naturally, without gas flow, under vacuum. This process produced a conformal, coarse, light-gray deposition consisting of nanowire and submicron columnar growth on the substrate surface. The sample was then cleaved into 5 equally sized pieces, four of which were sealed in separate quartz ampoules of Ar and O_2 environments. The sealed samples underwent a unique combination of thermal annealing (650 °C and 900 °C), with a fixed anneal time of 30 minutes (conditions summarized in Table 1). In all cases, a reflective metallic reduced Zn deposit (confirmed with EDX) was found to have condensed along the ampoule walls. The four samples, along with the unnannealed "control" case, were morphologically characterized with a field emission scanning electron microscope (FESEM, Hitachi S4700-II, excitation 15 kV). Post-growth analysis of nanowire size distributions was conducted by tracing radial and axial dimensions of a sample size of approximately n=1000 nanowires, for each treatment group, along 9 equally spaced sample regions (corners, edges, center) within imageJ (image processing) software. Relative Mg content was determined using an Energy-dispersive X-ray spectroscopy (EDX) attachment by sampling the aforementioned regions along each sample surface, at an excitation energy of 15 kV. Modification of crystal structures was determined with a High Resolution X-ray Diffractometer (PANalytical XPert PRO XRD, $\kappa\alpha_1$=1.540598 Å, $\kappa\alpha_2$=1.544426 Å). Ultraviolet luminescence spectra were ascertained using a JEOL JSM 630 SEM with an attached cathodoluminescence (CL) system, operating at an excitation current of 0.5 nA for UV-A analysis and 2 nA for UV-C analysis. Raman spectra were gathered with a Renishaw InVia spectroscopy system with a 100× objective lens, using a laser source of λ = 488 nm. Finally, conductance modification subject to UV illumination (UVP EL Series Lamp, 45 mW/cm^2) were determined with a Kiethly 4200 Semiconductor Analyzer System within a "light-tight" micromanipulator probe-station, utilizing tungsten-tipped soft

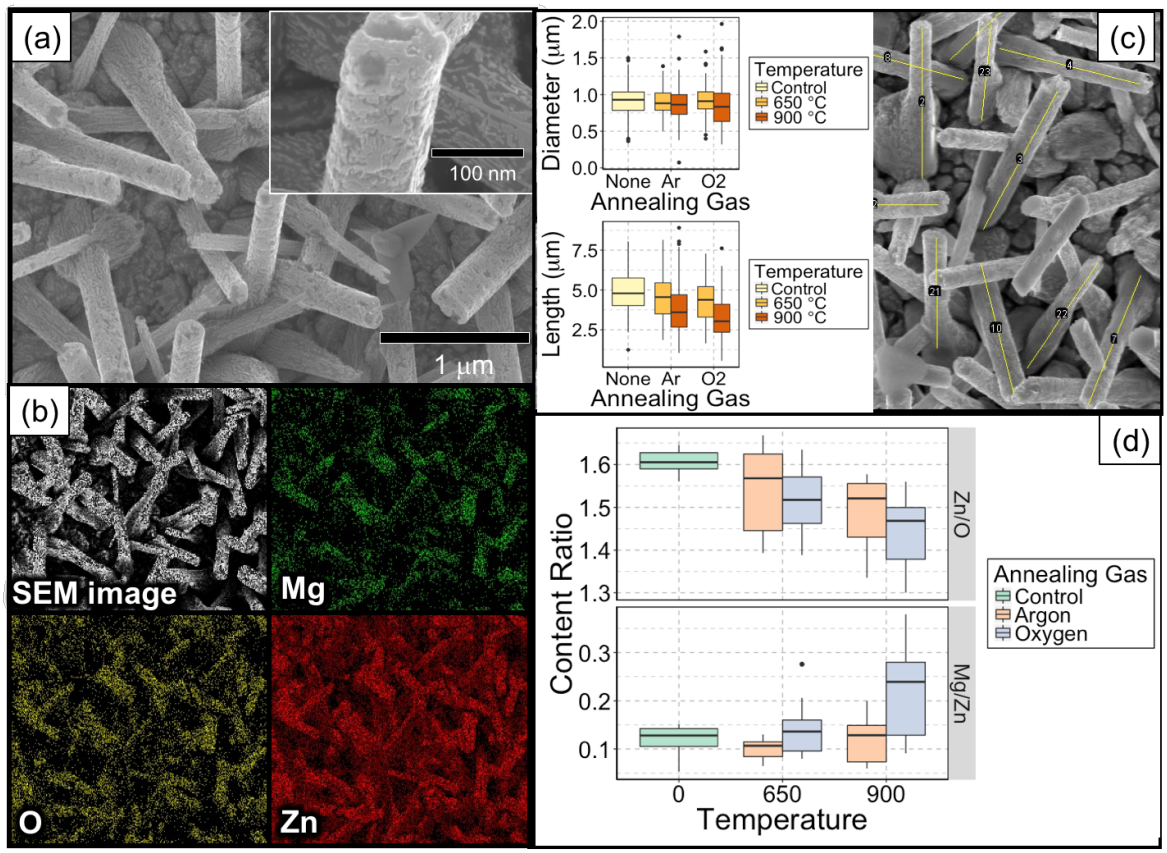

Figure C.2: (a) SEM Micrograph of ZnMgO nanowire array (inset: zoomed view of single wire) (b) EDX Mapping of grown nanowires, uncovering spatial resolution of Zn, Mg, and O_2 constituents (c) Left: Measured size distributions (top: diameter, bottom: length) of nanowires for each anneal treatment group. Right: sample micrograph of traced nanowire lengths, post-anneal. (d) Elemental atomic ratio as a function of anneal temperature and anneal gas

probes. Post-experimental processing of data which included cleaning, analysis, and visualization were performed in R language with the ggplot2 library.

C.4 Results and Discussion

Figure C.2(a) shows the scanning electron micrograph (SEM) of the as-synthesized ZnMgO nanowire arrays, with a zoomed view of a single nanowire in the inset. The wires exhibited a vertical (yet regularly offset by a slight angle) growth pattern with a characteristic coarse surface texture. Energy-dispersive X-ray spectroscopy (EDX)

mapping in Figure C.2(b) further revealed the elemental composition of the nanowires, confirming the incorporation of Mg. As seen in Figure C.2(d), EDX quantification analysis shows that the Mg content relative to Zn extends as high as 15% upon the initial synthesis. A growth mechanism that accounts for the carbothermal reduction of ZnO with a Mg_3N_2 source yields reaction products of $Zn_xMg_{(1-x)}O$, ZnO, MgO, and Zn_2SiO_4, as illustrated in Figure C.1. Upon subjecting the nanowires to each anneal condition, the average relative composition of Mg in all anneal cases widens in variance, and is most pronounced when annealed in O_2 at 900 °C. In this case, the median Mg content relative to Zn is found to be approximately 24%, as shown in Figure C.2(d). Similarly reported behavior has indicated that the alloying Mg content reaches saturation due to phase segregation, despite larger annealing temperatures (Liu *et al.*, 2010). From Figure C.2(c) the effect of annealing on nanowire size (diameter and length) does not ostensibly appear pronounced, however an analysis of variance (ANOVA) coupled with a pairwise Tukey's range test confirms a statistically significant reduction in the distributions of both nanowire dimensions, especially for higher temperature (see supporting information Table S.1 and S.2). This reduction is explained by a modification of the underlying ZnO nanostructure, with Zn^{2+} vaporizing and dissociating from the nanowire (Lamoreaux *et al.*, 1987), allowing Mg^{2+} to occupy the vacancies and integrate within the crystal lattice. As presented in Figure C.2(d), this process is evidenced by a decrease of relative Zn:O content for all nanowire arrays, while Mg content is found to increased relative to Zn, post-anneal. In a similar study, Kim et al. describe coating MgO nanowire surfaces with particle-like ZnO crystallites that sinter upon annealing, giving rise to increased dimensions (Kim *et al.*, 2007), and was further attributed to an increase in oxygen vacancies that allowed for the relaxation of interfacial strain (Shimpi *et al.*, 2010). In our work, we find that the ZnO lattice consumes Mg^{2+}, and nanowire dimensions decrease as the

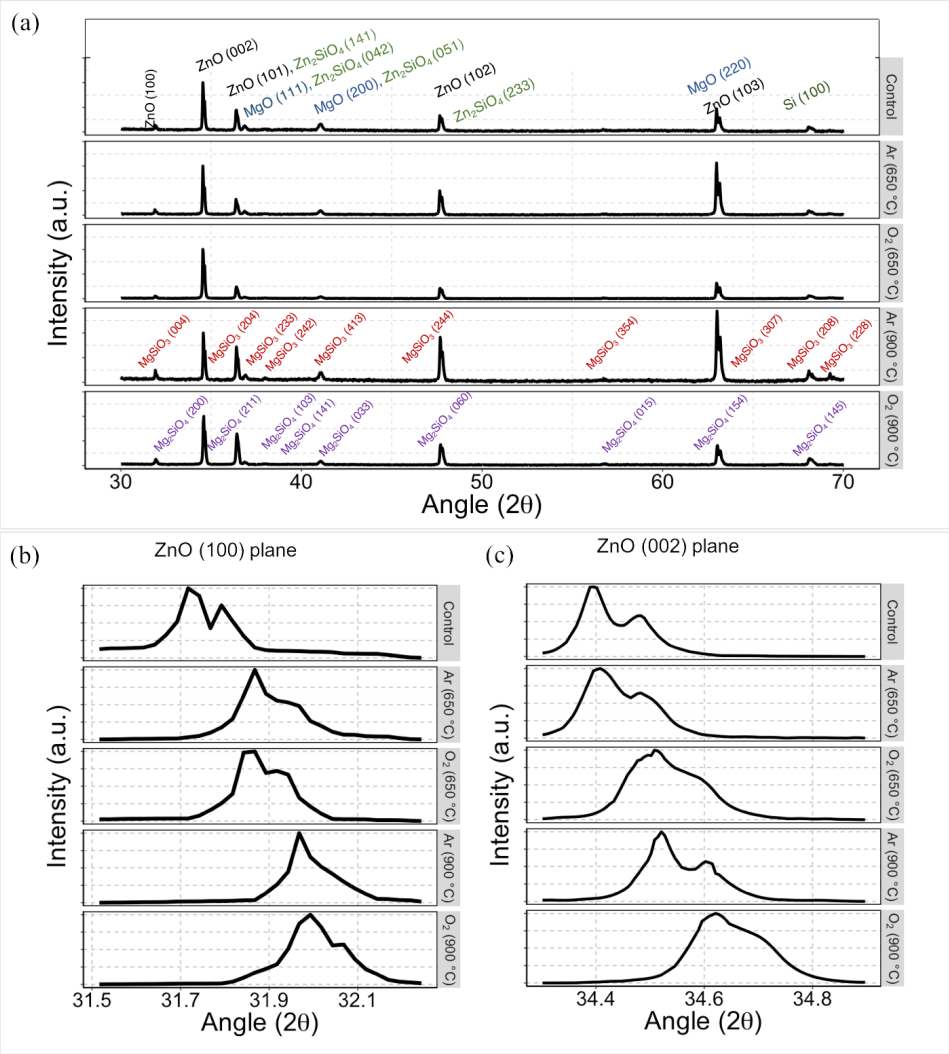

Figure C.3: (a) Compiled XRD Spectra of as-synthesized nanowires (labeled as control) and all nanowire anneal conditions. (b) Zoomed view of ZnO peaks emerging from the (100) plane and (c) ZnO (002) plane

atomic exchange kinetics are reversed.

Presented in Figure C.3(a) are the x-ray diffractograms (XRD) of all annealed ZnMgO nanostructure arrays, along with the as-synthesized case (labeled as *control*). From the diffraction pattern of the as-synthesized nanowires, characteristic peaks associated with ZnO, Zn_2SiO_4, and MgO (JCPDS 05-0664, JCPDS 00-024-1469, and JCPDS 04-0849, respectively) can be observed (which indicates a slight degree of phase segregation between wurtzite ZnO and cubic MgO phases). Because

the nanostructures retain hexagonal form, cubic MgO is not as predominant a reaction product as ZnO. Additionally, the formation of Zn_2SiO_4 is largely confined to the substrate, as confirmed by EDX mapping. As shown in Figures C.3(b) and C.3(c), annealing results in a right-shift of the ZnO a-axis corresponding to the (100) plane (2θ = 31.7°), as well as the ZnO c-axis corresponding to the (002) plane (2θ = 34.4°), by as high as $\Delta 2\theta$ = 0.3° in both cases (Note: the presence of bimodal peaks arises from dissimilar $\kappa\alpha$ excitation energies emitted from the diffractometer). Principally, the combined effect of a smaller electronegativity and electronic radius of Mg^{2+} (Pauling electronegativity: 1.31 and 0.57 Å radius) to that of Zn^{2+} (Pauling electronegativity: 1.65 and 0.60 Å radius) facilitates the formation of the Mg—O bond and leads to the decrease of observed lattice parameters (Liu *et al.*, 2005; Singh *et al.*, 2011; Wei *et al.*, 2012; Das *et al.*, 2013; Saha *et al.*, 2015). Thus, Mg^{2+} is effectively substituting Zn^{2+} without significantly modifying the ZnO nanowire crystal structure, which further explains the reduced nanowire size distributions from Figure C.2(c). However, when these modified lattice parameters are scaled up to the average nanowire dimensions, we find that this phenomenon alone does not completely account for the observed reduction in array aspect ratio. Instead, reduced radial and axial dimensions also stem from Zn^{2+} dissociating completely from the nanowires, which is especially evident at high temperatures; and is supported by Zn deposits found along the sealed ampoule walls. Nonetheless, a summary of the 2θ peak shifts and lattice parameters is presented in Table C.1. In addition to shifts of ZnO related peaks, new peaks emerge due to reactions on the substrate surface when annealed at high temperatures. Annealing in inert Ar results in the formation of $MgSiO_3$ (enstatite, JCPDS 01-088-1924), whereas annealing in reactive O_2 results in the formation of Mg_2SiO_4 (forsterite, JCPDS 01-079-1490). Notably, the diffraction pattern and luminescence spectra of these mineral forms are a strong function of

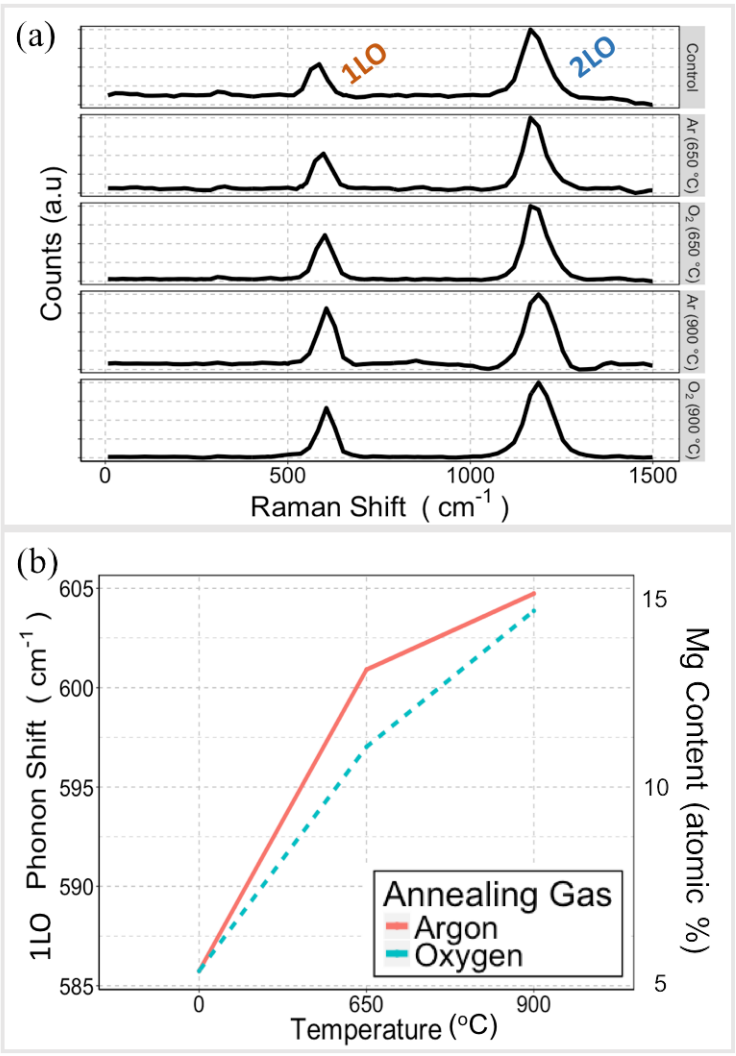

Figure C.4: (a) Compiled Raman Spectra of control group and all anneal conditions (b) Extracted 1LO Phonon shift extracted from Raman spectra as a function of temperature

crystal structure and imperfect stochiometry, and these results are further discussed in the context of cathodoluminescence analysis.

The presence of Mg^{2+} behaving as a substitutional ion in a fundamentally ZnO nanostructure is suported by the Raman spectrogram shown in Figure C.4(a). Increasing temperature shifts the peak position of the 1LO phonon mode from approximately 585 cm^{-1} to 605 cm^{-1}, as summarized in Figure C.4(b). The modification of the 1LO peak position is found to be a greater function of temperature than that

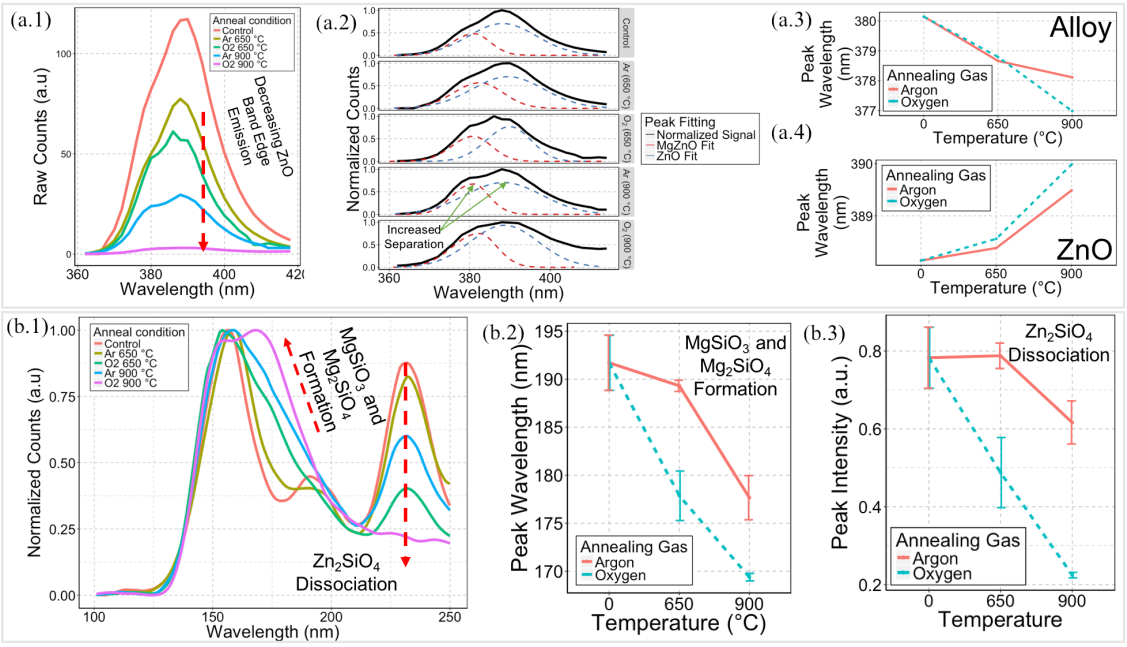

Figure C.5: (a.1) Raw cathodoluminescence spectra at low-energy ultraviolet range (UV-A) near the ZnO band edge with (a.2) normalization of peak intensity and extracted peak intensities of (a.3) ZnMgO alloy and (a.4) ZnO. (b.1) Cathodoluminescence Spectra at higher-energy ultraviolet range (UV-C) highlighting (b.2) $MgSiO_3$ and Mg_2SiO_4 formation from 170-190 nm peak shift and (b.3) Zn_2SiO_4 dissociation at 230 nm with reduced peak intensity as a function of temperature and annealing gas environment.

of the ambient gas environment, and is attributed to temperature-sensitive contributions from the LO mode of MgO (Huso *et al.*, 2014) at 720 cm^{-1}. Prior studies have reported that the maximal Mg content that the ZnO crystal can accommodate is 30%, corresponding to a Raman shift (Huso *et al.*, 2015) of 615 cm^{-1}. A model that maps Raman shift to Mg content was developed by Huso et al. utilizing fine control of Mg in sputtered ZnO thin films to explain a bowing feature in the Raman spectral response (Ye *et al.*, 2007). By cross-referencing the change in 1LO peak position to this model, as well as the modification of 2θ peak diffractions of ZnO, the estimated Mg content incorporated is demonstrably increased via annealing, and agrees with EDX analysis.

The cathodoluminescence (CL) spectra of all ZnMgO wires were measured both

in the UV-A range, presented in Figure C.5(a.1), and in the UV-C range, presented in Figure C.5(b.1). While the relative intensity of the band edge of ZnO (≈380 nm) dominates all other peaks across the spectrum, the intensity of the peak is found to decrease with increasing annealing temperature, given the same level of CL excitation current. This is attributed to the increased formation of O_2 defects along the wires, leading to an increased green-band emission (see supporting information Figure S.1). The higher energy UV-C cathodoluminescence response, as presented in Figure C.5(b.1), was normalized to the peak at 156 nm, corresponding to the bandgap of MgO. From the normalized response, the relative intensities of two other peaks can be compared: specifically those between 165-183 nm (linked to the band energy ranges of Mg_2SiO_4 and $MgSiO_3$) (Shankland, 1968; Stashans *et al.*, 2010) and at 230 nm (linked to the band energy of Zn_2SiO_4) (Mishra *et al.*, 1991; Karazhanov *et al.*, 2009). The progressive attenuation of the Zn_2SiO_4 peak intensity, shown in Figure C.5(b.3), and the increase of the Mg_2SiO_4 and $MgSiO_3$ peak intensity, shown in Figure C.5(b.2), illustrate a relative exchange in composition, directly resulting from dissimilar anneal environments. Because molecules of Zn tend toward vapor pressures lower than that of Mg, ZnO nanostructures and Zn_2SiO_4 will more preferably dissociate into Zn^{2+}, O_2, and SiO_4^{4-} at higher anneal temperatures (Lamoreaux *et al.*, 1987). Isolated orthosilicate ions must therefore react to form a forsterite molecules with Mg, or equilibrate into silica if reaction-limited. As previously discussed, Zn deposits were found along the sealed ampoules, which indicate a vaporization and dissociation of Zn^{2+} from the nanowire arrays. As O_2 is a reactive gas, Zn_2SiO_4 is found to have completely converted into Mg_2SiO_4 (Shankland, 1968). This is validated by the fact that the relative CL peaks associated with Mg_2SiO_4 rise considerably under an oxidizing environment, until forming a close shoulder to the MgO band edge (in other words, exhibiting a distinct species, rather than coalescencing with MgO). Annealing

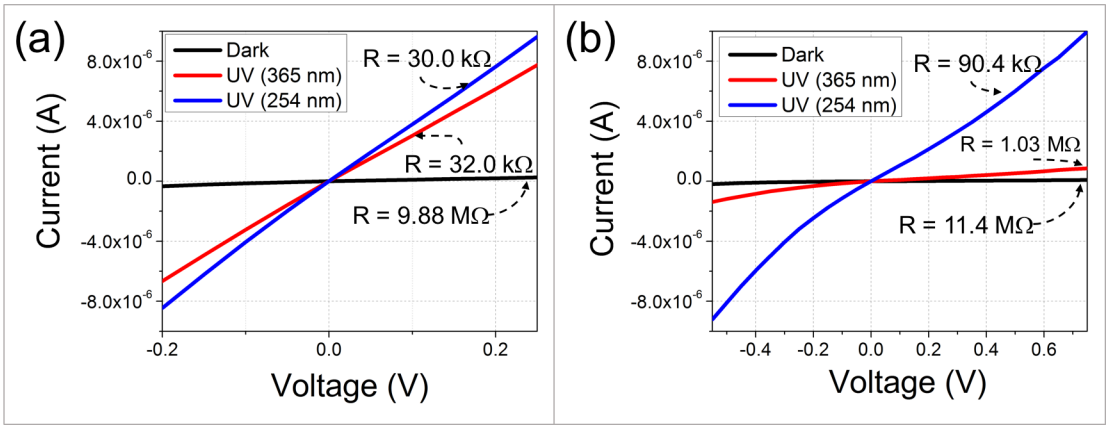

Figure C.6: Current-Voltage measurement of ZnMgO NW photodetector as a function of illumination conditions for nanowires that were (a) initially grown and (b) received thermal treatment at 900 °C in O_2

in Ar reduces the relative peak intensity of the Zn_2SiO_4 peak to approximately 75% of its original level, and in the inert environment, must only react with MgO in a kinetically-limited manner to form half as much (molar ratio) of $MgSiO_3$ (Stashans *et al.*, 2010) (see reactions of both anneal environments in Figure C.1). Mishra et al. have described a modification of the orbital symmetries t_1 and t_2 of SiO_4^{4-} ions, which have been influenced by the oxidizing reactions mechanics, contributing to a range of orthosilicate ion peak position shifts found in Figure C.5(b.1). These results are illustrated in Figure C.1, and summarize the complex reaction kinetics of Zn^{2+} dissociation in conjunction with silicate formation as a function of the annealing environment.

Current-Voltage measurements were conducted vertically across the nanowire arrays for the as-synthesized case, shown in Figure C.6(a), and for samples annealed at 900 °C in O_2, shown in Figure C.6(b). Measurements were conducted in the dark and in the presence of UV-A (365 nm) and UV-C (254 nm) monochromatic illumination. The photoconductive properties of ZnO nanowires have long been attributed to the size effect of nanostructures, in correspondence with the adsorption/desorption of O_2 molecules along the nanowire surface leading to surface band bending and reducing

channel resistivity (Soci *et al.*, 2007; Yu *et al.*, 2012a; Xie *et al.*, 2014). The control case exhibited a negligible difference in conductance regardless of UV illumination wavelength, which suggests that band-to-band transition along the ZnO band edge largely contributes to its photoconductive behavior. However, in the annealed case, UV-A photoconduction is suppressed due to the increased formation of Zn vacancies, as evidenced by the attenuation of the peak ZnO band-edge luminescence, from in Figure C.5(a.1). Specifically, the conductance was found to increase by almost 2 orders of magnitude (126 times) when illuminated with a UV-C source, as compared to a lower energy UV-A source, in which the annealed nanowire array only exhibited an increase of conduction by a factor of 11.

$$R_\lambda = \frac{\Delta I}{PA} \tag{C.1}$$

$$G = \left(\frac{\Delta I}{e}\right) / \left(\frac{P}{h\nu}\right) \tag{C.2}$$

The spectral responsivity (R_λ) and photoconductive gain (G) are key figures of merit that distinguish photodetector systems. These figures are defined by the relationships expressed in eq. (C.1) and (C.2), where ΔI represents the difference between the photocurrent and dark current, P is the irradiation power, A is the area impinged by photons on the top surface of the nanostructures, $h\nu$ is the illumination energy, and e is the elementary electronic charge (Yu *et al.*, 2012a). The results of both performance characteristics are summarized in Table C.2 for treated and untreated cases, compared between UV-A and UV-C illumination. In agreement with the observed changes in photoconduction, the most notable differences in R_λ and G occur for UV-A illumination (λ=365 nm), in which at least a single order of magnitude difference is estimated between the as-grown ($R_{\lambda|\lambda=365} = 1.70\times10^{-5}$ (A/W), $G_{|\lambda=365} = 5.79\times10^{-5}$)

Photodetection Metric	As-Synthesized	Annealed
$R_{\lambda\|\lambda=365}$ (A/W)	1.70×10^{-5}	1.78×10^{-4}
$R_{\lambda\|\lambda=254}$ (A/W)	2.20×10^{-4}	2.15×10^{-4}
$G_{\|\lambda=365}$	5.79×10^{-5}	9.85×10^{-4}
$G_{\|\lambda=254}$	9.47×10^{-4}	1.05×10^{-3}
$NEP_{\|\lambda=365}$ ($WHz^{-0.5}$)	1.02×10^{-8}	1.56×10^{-9}
$NEP_{\|\lambda=254}$ ($WHz^{-0.5}$)	7.91×10^{-10}	1.46×10^{-9}
$D^*_{\|\lambda=365}$ ($cmHz^{0.5}W^{-1}$)	3.10×10^{9}	2.03×10^{10}
$D^*_{\|\lambda=254}$ ($cmHz^{0.5}W^{-1}$)	4.00×10^{10}	2.17×10^{10}

Table C.2: Comparison of photodetection performance and noise metrics between as-grown and thermally treated ZnMgO nanowires as a function of ultraviolet illumination energy

and annealed cases ($R_{\lambda|\lambda=365} = 1.78\times10^{-4}$ (A/W), $G_{|\lambda=365} = 9.85\times10^{-4}$), illustrating a suppression of UV-A photoconduction in the nanowire ensemble. Likewise, these figures do not change appreciably with UV-C illumination.

$$NEP = (1/R_\lambda)(2qI_d + 4kT/R_v)^{1/2} \tag{C.3}$$

$$D^* = (Af)^{1/2}/NEP \tag{C.4}$$

To further investigate detection performance disparities, detector noise characteristics were calculated in order to distinguish the sensitivity of ZnMgO nanowires before and after thermal anneal. Noise equivalent power (NEP) and detectivity (D^*) were evaluated according to eq. (C.3) and (C.4), where k is Boltzmann's constant, T is the absolute ambient temperature, I_d is the dark current for a specified operating voltages, R_v is the device differential resistance, and f is the amplifier bandwidth (taken as 1 kHz in this analysis) (Sze and Ng, 2006). Along with detector perfor-

mance characteristics, detector noise metrics are also summarized in Table C.2, and demonstrate a reduction of NEP for UV-A illumination (due to decreased spectral sensitivity), whereas a slight increase in NEP is observed for UV-C illumination. As highly sensitive detectors tend to exhibit low NEP and high D^*, the sensitivity of ZnMgO detectors increases in conjunction with suppressed photoconductive gain at λ=365 nm. Because annealing was found to reduce Zn content from the nanowire system, electrons from ZnO become less effective at band-to-band transitions, which diminishes the effect of surface band-bending from oxygen desporption (Feng, 2012). On the substrate surface, the formation of Mg_2SiO_4 results in stochiometricly heterogeneous MgO films, thereby increasing thermal noise. Annealing in oxygen was shown to increase the incidence of O_2 related green-band defects (see supporting information Figure S.1), which contribute directly to thermal agitation of charge carriers (Hsu *et al.*, 2004; Djurišić *et al.*, 2007; Lee *et al.*, 2015). However, this NEP increase is negligible in comparison to the modification of spectral sensitivity under UV-A illumination, which suggests a minor design tradeoff between noise and tunability.

C.5 Conclusion

In conclusion, high-quality ZnMgO nanowires have been synthesized utilizing a novel growth mechanism that incorporates Mg dissociated from Mg_3N_2, in tandem with the carbothermal reduction of ZnO. Modification of the size characteristics, crystal lattice properties, and spectral response from annealing were found to be internally consistent with measured Mg content. In particular, EDX, Raman, and CL revealed a spectral evolution for each treatment group of nanowire arrays, giving rise to increased Mg^{2+} incorporation, along with the dissociation of Zn^{2+}. Statistical inference (ANOVA paired with Tukey's Range Test) was undertaken to discern a reduction of nanowire dimensions, and was cross-referenced to a modification of the

ZnO lattice parameters, as well as the formation of Zn vacancies.

Suppressed photoconductivity under UV-A illumination with retained photoconductivitiy under high energy UV-C illumination was observed for samples post-thermal treatment. An order of magnitude difference for both spectral responsivity and photoconductive gain between the annealed and control cases confirms the tunable filtering of high energy ultraviolet spectral responsivity. Increased thermal noise from the high temperature O_2 anneal process was associated with the increase of oxygen-related defects contributing to thermal agitation, which may present a design tradeoff in integrating ZnMgO as solar blind detectors. Thus, these results indicate that synthesized ZnMgO nanowires demonstrate promising selective UV-C detection capabilities, in which controlled post-synthesis thermal treatment may effectively tune for selective, high-pass, solar-blind ultraviolet detection.